Electronic Properties of Graphene Systems with Sublattice-Asymmetry

Aktor, Thomas

Publication date:
2018

Document Version
Publisher's PDF, also known as Version of record

Electronic Properties of Graphene Systems with Sublattice-Asymmetry

Thomas Aktor
PhD Thesis August 2018

DTU Nanotech
Department of Micro- and Nanotechnology

TECHNICAL UNIVERSITY OF DENMARK

PHD THESIS

Electronic Properties of Graphene Systems with Sublattice-Asymmetry

Author:
Thomas AKTOR

Supervisor:
Prof. Antti-Pekka JAUHO

A thesis submitted in fulfillment of the requirements for the degree of Ph.D.

at the

Center for Nanostructured Graphene (CNG)
DTU Nanotech

August 4, 2018

Preface

This work is submitted for the candidacy for a Ph.D degree at the Technical University of Denmark(DTU). The work has been carried out at DTU Nanotechin the period from May 2015 to August 2018. The project has been founded by the Center for Nanostructured Graphene (CNG), which in turn is sposered by the Danish Research Foundation, Project DNRF103, together with DTU Nanotech. The project has been supervised by Prof. Antti-Pekka JAUHO. Unless otherwise state all simulations done during this ph.d. has been written and implemented by me in C or python.

I would to thank Antti for all the support during the process of this ph.d. I would also like to thank Stephen R. Power who has been a defacto unofficial cosupervisor, and of amazing help analysing and interpreting results throughout this process. I would also like to thank both the groups of Prof. Antti-Pekka JAUHOand Prof. Mads Brandbyge for being great colleagues. Both at work and outside of it I have fully enjoyed working side by side with them. Extra special thanks goes to Søren Schou Gregersen for helping with the creation of the NDtables storage method, Johannes Handberg Juul Martiny for his help in correcting the text of this thesis and Mattias Lau Nøhr Palsgaard for his company when writing the thesis itself. With these 3 the thesis would not have completed.

Finally great thanks goes to my familly, especially my wife Anna Louise Aktor for her amazing support and my daughter Clara Isabella Aktor for making it all worth it.

Thank you all,
Thomas Aktor

Abstract

Electronic Properties of Graphene Systems with Sublattice-Asymmetry

by Thomas AKTOR

The interest in 2 dimensional materials has exploded in the last decade. Purposeful engineering of these materials has been a major field of research in this period, as specific properties from each material are wanted in different combinations.

As a consequence of the fact that graphene has a collection of some of the most exotic properties, which together with the amazing ability of carbon to chemically bond to in many different ways, has resulted in graphene being one of the most studied of these materials.

In this thesis we deal with engineering of the electronic properties of graphene, where we have special interest in the formation of band gaps, which are essential for the use of graphene as field effect transistors, and the valleytronic applications of graphene.

Valleytronics is a field similar to electronics where the valley, or pseudospin, degree of freedom is the carrier of information instead the electric charge.

Both gap opening and valley specific behaviour is seen when breaking the inversion symmetry of the graphene unit cell. By introducing sublattice dependent potentials in graphene based devices we investigate the interactions between geometry and different potential distributions.

Using a tight binding description, we investigate boundaries between domains where the sublattice potentials are swapped in both graphene sheets and in graphene nanoribbons and see the formation of interface states that are potentially valley polarised. These states appear for energies where the bulk of the material has no states. This effects are stable under disorder and appear even in the case of low concentrations of dopants with sublattice distributions similar to what is observed in experiments. We also show the importance of interactions with edge geometry when considering these sublattice-asymmetric potentials.

We consider scattering of electronic waves off circular localised sublattice-asymmetric potentials using the Dirac approximation and show strong valley dependence when pure mass dots are considered. The valley dependence is highly energy dependent and could be tuned using a back gate. We also use an atomistic tight binding model to confirm these results. This is done in a dual probe setup with one probe far to the left of the mass dot simulating an incoming plane wave and the second probe placed behind the dot to pick up the scattered current. This atomistic calculation takes advantage of the Green's functions patching methods.

As the Green's functions patching methods are etremely useful for calculations we also make an effort to make method accesible for materials other than graphene, by describing and testing an alternate implementation of the method, which takes advantage of the effciency of fast Fourier transforms. This will be useful for research that consider devices with large separations and theoretical multi probe investigations.

Resumé (Danish)

I et forsøg på at forstætte med at forbedre den næste generation af elektroniske komponenter, er forskning inden 2dimensionelle materialer eksploderet indenfor det sidste årti. Ved specifikt at ændre på materialerne på nano-skala forskellige materialers kan ændres designes eller kombineres.

Det faktum at det har mange eksotiske egenskaber sammen med evnen til kemisk at binde sig til andre materialer utroligt fleskibelt, har gjort grafen, et sekskantet gitter bestående af kulstof atomer, til et af de mest undersøgte af de 2dimensionelle materialer.

I denne afhandling undersøger vi grafens elektroniske egenskaber med specielt fokus på åbening af båndgab, som er nødvendige hvis grafen skal overtage rollen som transitor, samt de valleytroniske andvendelsmuligheder som grafen har.

Valltronics er måde at bruge den særlige valley frihedsgrad til at transportere information på lige fod med hvad spintronics bruge spin og elektronik bruger elektrisk ladning til.

Ved at bryde inversionssymmetrien i enhedscellen for grafen, kan vi introducere både båndgab og valleytroniske egenskaber. Vi introducer del-gitter specifikke potentialer og undersøger sammenhængen mellem materialegeometri og forskellige potentialefordelinger.

Ved at bruge en tight binding beskrivelse undersøger vi hvordan grænser ved skift i det dominerende del-gitter fører til potentielt valleypolariserede tilstande der løber langs med grænsefladen, både i flager af grafen såvel som i nanoskopiske grafenbånd. Disse grænsetilstande opstår for energier hvor resten af materialet har et båndgab og bliver derved elekstrisk isolerede. Vi viser at både båndgab og grænse tilstande opstår selv hvis der stor grad af uorden i systemet og selv hvis potentialerne bare er gennemsnitlige effekter af spredt doping, doping profiler der til forveksling ligner dem der er set i eksperimenter. Samtidig viser vi også at kant geometrien i nanoskopiske grafenbånd har en enorm indflydelse på de elekstriske egenskaber.

Ved at bruge Dirac approksimationen, kigger vi også spredning af indkommende planbølger der rammer cirkulære lokaliserede områder med del-gitter potentialer og viser at strømmen i de individuelle valleyer opdeles baseret på systemenergien, og specielt når potentialerne er rene Dirac masser. Dermed kan de valleytroniske egenskaber styres eksternt ved hjælp påførte elekstriske felter. Vi bruger ligeledes en tight binding model til at bekræfte resultaterne fra Dirac modellen. Det gøres ved bruge to prober, en langt til venstre for cirklen for at simulere den indkommende planbølge, og den anden lige til højre for cirklen for at detektere den spredte strøm. Dette gøres ved hjælp af en metode kaldet Green's function patching.

Siden af Green's funcion patching kan bruges til sådan beregninger hvor dele af system er pladseret langt fra hinanden i et ellers perfekt ensartet materiale præsenterer vi også implementerings metoder der kan benyttes til andre materialer en grafen til lignende beregninger i håbet om det vil kunne benyttes i fremtidig forskning, der også kigger på flerprobe systemer eller interaktion mellem lokaliserede defekter.

List of Contributions

Papers:

Paper I (attached):
Electronic transport in graphene nanoribbons with sublattice-asymmetric doping,
Authors: Thomas Aktor, Antti-Pekka Jauho, and Stephen R. Power
Physical Review 93, 035446 (2016)

Paper II (not attached):
Valley splitting due to local pseudospin asymmetry in graphene,
Authors: Thomas Aktor, Antti-Pekka Jauho, and Stephen R. Power
In preperation

Below is a list of conference contributions:

- **Graphene nanoribbons with sublattice-asymmetric doping**, Carbonhagen 2015
  T. Aktor, A.-P. Jauho, and S. R. Power
- **Graphene nanoribbons with sublattice-asymmetric doping**, Graphene 2016
  T. Aktor, A.-P. Jauho, and S. R. Power
- **Disorder-induced localised gating in graphene**, Graphene 2017
  T. Aktor, A.-P. Jauho, and S. R. Power
- **Disorder-induced localised gating in graphene**, Carbonhagen 2017
  T. Aktor, A.-P. Jauho, and S. R. Power

Nomenclature

Abbriveations:

DOS	Density of states
LDOS	Local density of states
STM	Scanning tunneling microscopy
CVD	Chemical vapor deposition
VCA	Virtual crystal approximation
CPA	Coherent potential approximation
LCAO	Linear Combinations of Atomic Orbitals
FFT	Fast Fourier transform
GNR	Graphene nanoribbon
AGNR	Armchair graphene nanoribbon
ZGNR	Zigzag graphene nanoribbon
APRES	Angle resolved photo emission spectroscopy
n-D	n-Dimensional
1NN	First nearest neighbour
DFT	Density functional theory

Notation and constants:

e	Elementary charge	1.602×10^{-19}C
h	Planck's constant	6.63×10^{-34}Js
$\hbar = h/2\pi$	Planck's reduced constant	1.05×10^{-34}Js
a_{cc}	Interatomic carbon distance	1.42Å
$\mathbf{M}$	Matrix or vector	
$\mathbf{M}_{ij}$	The ij elements of $\mathbf{M}$	
$\hat{c}$	Second quantisation operator	

Contents

List of Figures

"So perhaps the best thing to do is to stop writing Introductions and get on with the book."

A.A. Milne

1 Introduction

Any reasonable text should set reasonable expectations with the reader. In order to clear up what should be expected from this thesis, and get the reader into the right frame of mind, we start out with introducing the subject of graphene and its already rich history. We will also explain how this thesis tries to advance the knowledge of graphene and similar materials.

1.1 The exciting 2 dimensional world of graphene

The confirmation that graphene exists, not only awarded the Nobel prize [1] (see figure 1.1), but opened up a world filled with materials that was one dimension short of the regular physics we knew. Among the exciting properties of graphene is extraordinary mechanical, thermal, optical and electronical properties [2–4]. The promise of a material stiffer than diamond, with extraordinary high electronic velocities that is also broadband absorber but at the same time virtually see-through, opens up not only for potential upgrades of current technologies, but also potential technological innovation. Graphene also embraces the quantum world it is a part of by having exotic properties such as Klein tunneling and balistic transport. These discoveries kickstarted the entire research field of 2 dimensional materials, which apart from graphene now includes a whole host of diverse and exciting materials. These materials range from semi-metals such as graphene to semiconductors such as MoS_2 and insulators as hBN as well as many other.
The general technique of mechanical exfoliation that was used originally to separate the graphene layers within graphite, has since supplemented with growth techniques that can directly synthesise the 2 dimensional materials such as chemical vapor deposition (CVD), that allow for large scale industrial fabrication. Recently moves have been to standardise both fabrication and calculations to both identify [5] and synthesise almost custom made materials. Furthermore these 2 dimensional materials can now be combined in layered structures to create a whole new set of materials, the so called the van der Waals heterostructures [6, 7].

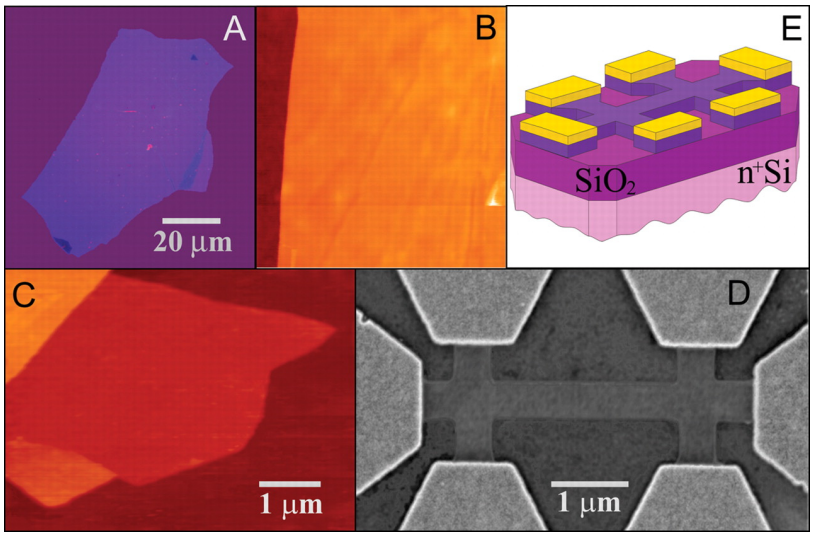

FIGURE 1.1: Graphene films. (A) Photograph of a relatively large multilayer graphene flake. (B) Atomic force microscope (AFM) image of 2 μm by 2 μm area of this flake near its edge. (C) AFM image of single-layer graphene. (D) Scanning electron microscope image of one experimental device. (E) Schematic view of the device in (D). Figure from [1]

1.2 Electronics and the nanoscale

The story of electronics is a story of exponential growth. In 1965 Gordon E. Moore made a prediction that the number of transistors in dense integrated circuits would double approximately every year [8]. This held true for around 50 years by halving the size of the individual transistors every two years, but of course this progress is impossible to continue forever, and the current size of commercial transitors is already $< 14nm$ (Intel's current standard size). Entering the nano regime causes quantum effects to become more domninant, and thus quantum calculations is needed when designing the next generation of electronics.

Whilst graphene is the oldest of the 2 dimensional materials the great flexibility of carbon also allows it to remain one of the most malleable as well as on of the easiest to produce, and as such remains an active research topic. Furthermore it has quite unique electronics including linear electronic bands, which makes the electrons behave in manyways as massless relativistic particles, including phenomenon like suppressed backscattering, the so called Klein tunneling [9], and high electronic velocities. The malleablity of graphene has opened up for specific engineering of electronic properties, specifically the band gap in graphene has been the subject of modification. The main goal has been the use of graphene field effect transitors in next generation electronics, for which the size band gap is essential.

In order for graphene based devices to be viable we need to be able to reliably mass produce them, and hence they need to be stable under small pertubation, changes or impurities. Random disorder inevitably happens due to small errors in production, changes in lab conditions or similar. Many modifications that require atomic precison, such as nanoribbon structures or antidot lattices, break down exactly due to random disorder. However, methods that are induced due to some average effect of disordered processes such as doping [10–18] tend to be robust under small changes and pertubations.

1.3 Valleytronics

The 2 dimensional materials introduces viable alternatives to regular electronics using different quantum properties as the bit indication. The manipulation of the these quantum numbers usually bears the name *property*-tronics, two which are relevant in the context of graphene, namely spintronic which uses the spin as the important quantum property and **valleytronics** [19] which uses the distinct local extrema of the electronic bands called *valleys*.

The road to valleytronics in graphene is a long and winding one. The properties that makes graphene a desirable candidate for valleytronics are the low scattering between the inequivalent valleys the K and K' and correspondingly long valley lifetime. At the same time the valleys are generate in energy, and hence difficult to address individually.

A number of device setups have been proposed which are predicted to filter or split electrons according to their valley index.

First we have atomic-scale engineering, which has the downside of being hard to realise experimentally and difficult to scale up, and hence not suited for device application. These proposal include atomically-precise constrictions, interfaces and defects [20–24].

Many of the early graphene based valleytronic proposals involved bilayer graphene with an electric field acting differently on the two layers [25–27], which induces a Dirac *mass term*. In mono layer graphene we can also introduce a Dirac mass by introducing sublattice-asymmetric potentials. Sublattice-asymmetric potentials leads to chrial edge states [28], and domain walls where subalttice potentials are swapped lead to valley polarised boundary states [29]. This due to the opposite sign of the Berry phase in the two valleys, which also leads equal contribution with opposite sign to the Chern number from each valley [28].

This opposite chirality for the two valleys in the presence of a Dirac mass is predicted to cause electrons from different valleys to be deflected in opposite directions in an in-plane electric field, and to essentially act as a momentum-space Lorentz force [30–32], and is the focus point of sublattice-asymmetric approaches, which also includes placing graphene on top of hexagonal boron nitride (hBN) [33].

Another approach is the interaction with a pseudomagnetic field. Pseudomagnetic fields can be induced by non-uniform strains [34–36] and act with opposite sign on the K and K' valleys in order to preserve time-reversal symmetry. Systems have induced strain using many different approches such as suspending the graphene sheet [36], bending ribbons [37], or nanobubbles [34, 35]. However, experimental realisation of these systems may be hampered by the relatively small regions of parameter-space that give significant valley effects. Furthermore a recent study show a connection between pseudomagnetic fields and non-uniform mass term distributions [38].

1.4 Thesis content and layout

This goal of this ph.d. project has been twofold. The first was to look at sublattice specific engineering of graphene by implementing several different large scale models efficiently. The second was to try and extend the methods used beyond graphene, to enable large scale calculations of some of the other interesting 2D materials and also extend the types of systems that is possible to look at. To present this work the thesis is structured in the following way;

In **chapter 2** we give a detailed overview of the many methods and models used during ph.d. project. This includes, the tight binding model, the virtual crystal model, the coherent potential approximation, Green's functions and their connection to physical properties, different boundary conditions, and recursive and pathcing methods used to calculate the Green's functions.

In **chapter 3** we give a short introduction to the electronics of graphene and graphene nanoribbons. Including theoretical treatment in the tight binding model and the Dirac approximation.

In **chapter 4** we discuss why and how sublattice engineering works, and present some work made in a project together with ph.d. student Thomas Lane which looks at interface states between sublattice domains in graphene.

In **chapter 5** we discuss the work presented in paper I concerning asymmetric doping in graphene nanoribbons. We show that the exact electronic properties are very dependent on the edge geometry and that band gaps can form in the presence of asymmetric disordered potential. We also discuss interface states between prefered sublattice domains and the generation of mid gap states along the domain boundaries.

In **chapter 6** we discuss the work presented in paper II concerning mass dots in graphene. We show the electronic behaviour of such dots and demonstrate a strong angular valley splitting of the current. We solve the problem both using an analytical Dirac model as well as an atomistic tight binding model, using the Green's function patching method.

In **chapter 7** we discuss the use of discrete Fourier transforms, when calculating pristine Green's functions between sites in beloing to different unit cells efficiently, in order to extend the use of patching methods to other materials than graphene.

We end the main text by **concluding** on the main results and summarising the key points of the discussions from the different chapters.

In the **appendix** we discuss the computational implementation. This includes many of the considerations regarding memory, speed and storage.

"Where misunderstanding dwells, misuse will not be far behind. No theory in the history of science has been more misused and abused by cranks and charlatans—and misunderstood by people struggling in good faith with difficult ideas—than quantum mechanics."

Sean Carroll

2 Electronic methods and models

There exist many methods to deal with quantum mechanical problems. Here we distinguish between methods and models. The overarching models will usually come down to the form of the Hamiltonian, or equivalently the Green's function. The methods are the overarching tools that will appear multiple times in different contexts, and will focus how to calculate the physical parameters in a given system with a given model Hamiltonian or Green'sfunction. We will discuss how to modify the general models to take into account disorder, doping and other modification.

2.1 Tight binding

The tight binding model is an LCAO method (Linear Combinations of Atomic Orbitals), as it uses localised atomic orbitals as a basis set to describe the electronic properties. The general Hamiltonian can be written as

$$\mathbf{H}_{TB} = \sum_i \epsilon_i \hat{n}_i + \sum_{<ij>} \gamma_{ij} \hat{c}_i^\dagger \hat{c}_j \tag{2.1}$$

where $\hat{n}_i = \hat{c}_i^\dagger \hat{c}_i$ are the number operators, $\hat{c}_i^\dagger (\hat{c}_i)$ are the standard second quantization creation (annihilation) operators, $< ij >$ indicates all pairs of orbitals where $i \neq j$ and γ_{ij} is the hopping integral. This simple model works surprisingly well for graphene as a material (see Ref. [39]), even when only considering the π-orbitals of each atom. There is a set of these standardized models for graphene that we will consider, namely the 1NN and the 3NN models. Both models only consider the π-orbitals and only the hopping terms between atoms up to the third/first nearest neighbours respectively. The simplicity of the model allows us to treat a large number of atoms as the Hamiltonian only scales with number of the orbitals considered. In general the size of the Hamiltonian is essential when considering the two main computational limitations, speed and memory. This is further discussed in appendix A. Furthermore because of the local nature of the model the Hamiltonian becomes very sparse and can for many structures be tridiagonalized, meaning that it can be divided into blocks that only couple to the two neighbouring blocks, giving

the Hamiltonian a structure like the following

$$\mathbf{H}_{\text{system}} = \begin{bmatrix} \ddots & \ddots & \ddots & \vdots & \iddots \\ \ddots & \mathbf{H}_i & \mathbf{V}_{i+1,i} & 0 & \cdots \\ \ddots & \mathbf{V}_{i,i+1} & \mathbf{H}_{i+1} & \mathbf{V}_{i+2,i+1} & \ddots \\ \cdots & 0 & \mathbf{V}_{i+1,i+2} & \ddots & \ddots \\ \iddots & \vdots & \ddots & \ddots & \ddots, \end{bmatrix} \tag{2.2}$$

a structure which becomes very useful because of the way the Dyson equation (2.6) handles this type of system. For a more thourough treatment of the subject, one can use standard solid state textbooks such as Ref. [40].

2.2 Green's functions

Green's functions can be adapted from the original use in solutions of partial differential equations to solutions of the time dependent Schrödinger equation, and is a standard topic in many manybody textbooks such as Ref. [41]. We introduce the retarded Green's function as the solution to the equation

$$\mathbf{H}\mathbf{G}(t) + \mathrm{i}\frac{\partial}{\partial t}\mathbf{G}(t) = \mathrm{i}\delta(t)\mathbb{1}. \tag{2.3}$$

The retarded Green's function can be thought of as the propagator turned on at $t = 0$, useful if a pertubation is made then. A corresponding Green's function called the advanced propagates until $t = 0$, and has a similar equation

$$\mathbf{H}\mathbf{G}_A(t) + \mathrm{i}\frac{\partial}{\partial t}\mathbf{G}_A(t) = -\mathrm{i}\delta(t)\mathbb{1}. \tag{2.4}$$

In this work the Green's function will refer to the *retarded* Green's function unless otherwise stated explicitly. By broadening the Dirac-delta function by a positive infinetesimal $\eta \to 0_+$, we can get a convergent Fourier tranform. In energy space the equation then becomes

$$\lim_{\eta \to 0_+} [(E + \mathrm{i}\eta)\mathbb{1} - \mathbf{H}]\mathbf{G}(E) = \mathbb{1}. \tag{2.5}$$

The usfulness of the Green's functions are due to their close connection to several physical quantities such as the spectral operator. In some of the following sections we will look at how to calculate some important physical quantities using the Green's function, but first we will discuss its convenience when dealing with tridiagonal systems. Furthermore from now we will supress the explicit dependence on energy of the Green's function and introduce $z = E + \mathrm{i}\eta$ with the limit of $\eta \to 0_+$ being implied.

2.2.1 The Dyson equation and self-energy

The Dyson equation allows us to calculate the Green's function of separable systems. Imagine a system described by a Hamiltonian $\mathbf{H}_0$, which undergoes some pertubation $\mathbf{V}$, so that the total Hamiltonian can be written as a sum $\mathbf{H} = \mathbf{H}_0 + \mathbf{V}$. Let $\mathbf{g} = [z\mathbb{1} - \mathbf{H}_0]^{-1}$ be the Green's function that corresponds to $\mathbf{H}_0$. We will call this

type of Green's function the *uncoupled* Green's function. Now the equation for the Green's function become

$$\begin{aligned}
[z\mathbb{1} - \mathbf{H}]\mathbf{G} &= \mathbb{1} \\
[z\mathbb{1} - \mathbf{H}_0 - \mathbf{V}]\mathbf{G} &= \mathbb{1} \\
[\mathbf{g}^{-1} - \mathbf{V}]\mathbf{G} &= \mathbb{1} \\
\mathbf{g}^{-1}\mathbf{G} &= \mathbb{1} + \mathbf{V}\mathbf{G} \\
\mathbf{G} &= \mathbf{g} + \mathbf{g}\mathbf{V}\mathbf{G}
\end{aligned} \tag{2.6}$$

where the last equation is commonly refered to as the Dyson equation. In general the Dyson equation can also by used to infer the full Green's function from the uncoupled versions and the coupling to rest of the structure. Imagine two systems described locally by Hamiltonians $\mathbf{H}_{1,2}$ and coupled from 1 to 2 by $\mathbf{V}$. The Hamiltonian can be written as a block structure

$$\mathbf{H} = \begin{bmatrix} \mathbf{H}_1 & \mathbf{V}^\dagger \\ \mathbf{V} & \mathbf{H}_2 \end{bmatrix} \tag{2.7}$$

meaning that

$$\mathbf{H} = \begin{bmatrix} \mathbf{H}_1 & 0 \\ 0 & \mathbf{H}_2 \end{bmatrix} + \begin{bmatrix} 0 & \mathbf{V}^\dagger \\ \mathbf{V} & 0 \end{bmatrix}. \tag{2.8}$$

We now have a similar situation to before where the Hamiltonian can be written as a sum of two parts. Since $\mathbf{H}_0 = \begin{bmatrix} \mathbf{H}_1 & 0 \\ 0 & \mathbf{H}_2 \end{bmatrix}$ is diagonal, the uncoupled Green's function will be $\mathbf{g} = \begin{bmatrix} \mathbf{g}_1 & 0 \\ 0 & \mathbf{g}_2 \end{bmatrix}$, with $\mathbf{g}_{1,2}$ will be the uncoupled Green's function corresponding to $\mathbf{H}_{1,2}$. Writing the Green's function in block form as well and using the Dyson equation yeilds

$$\begin{aligned}
\mathbf{G} &= \mathbf{g} + \mathbf{g}\mathbf{V}\mathbf{G} \\
\begin{bmatrix} \mathbf{G}_{11} & \mathbf{G}_{12} \\ \mathbf{G}_{21} & \mathbf{G}_{22} \end{bmatrix} &= \begin{bmatrix} \mathbf{g}_1 & 0 \\ 0 & \mathbf{g}_2 \end{bmatrix} + \begin{bmatrix} \mathbf{g}_1 & 0 \\ 0 & \mathbf{g}_2 \end{bmatrix} \begin{bmatrix} 0 & \mathbf{V}^\dagger \\ \mathbf{V} & 0 \end{bmatrix} \begin{bmatrix} \mathbf{G}_{11} & \mathbf{G}_{12} \\ \mathbf{G}_{21} & \mathbf{G}_{22} \end{bmatrix} \\
&= \begin{bmatrix} \mathbf{g}_1 & 0 \\ 0 & \mathbf{g}_2 \end{bmatrix} + \begin{bmatrix} 0 & \mathbf{g}_1\mathbf{V}^\dagger \\ \mathbf{g}_2\mathbf{V} & 0 \end{bmatrix} \begin{bmatrix} \mathbf{G}_{11} & \mathbf{G}_{12} \\ \mathbf{G}_{21} & \mathbf{G}_{22} \end{bmatrix} \\
&= \begin{bmatrix} \mathbf{g}_1 + \mathbf{g}_1\mathbf{V}^\dagger\mathbf{G}_{21} & \mathbf{g}_1\mathbf{V}^\dagger\mathbf{G}_{22} \\ \mathbf{g}_2\mathbf{V}\mathbf{G}_{11} & \mathbf{g}_2 + \mathbf{g}_2\mathbf{V}\mathbf{G}_{12} \end{bmatrix}
\end{aligned} \tag{2.9}$$

In particular we can find the diagonal terms using the off diagonal terms

$$\begin{aligned}
\begin{bmatrix} \mathbf{G}_{11} \\ \mathbf{G}_{22} \end{bmatrix} &= \begin{bmatrix} \mathbf{g}_1 + \mathbf{g}_1\mathbf{V}^\dagger\mathbf{g}_2\mathbf{V}\mathbf{G}_{11} \\ \mathbf{g}_2 + \mathbf{g}_2\mathbf{V}\mathbf{g}_1\mathbf{V}^\dagger\mathbf{G}_{22} \end{bmatrix} \\
&= \begin{bmatrix} \left(\mathbf{g}_1^{-1} - \mathbf{V}^\dagger\mathbf{g}_2\mathbf{V}\right)^{-1} \\ \left(\mathbf{g}_2^{-1} - \mathbf{V}\mathbf{g}_1\mathbf{V}^\dagger\right)^{-1} \end{bmatrix} \\
&= \begin{bmatrix} \left(\mathbf{g}_1^{-1} - \Sigma_2\right)^{-1} \\ \left(\mathbf{g}_2^{-1} - \Sigma_1\right)^{-1} \end{bmatrix},
\end{aligned} \tag{2.10}$$

and we see that the equations for the fully coupled Green's functions becomes just the ordinary definition of the uncoupled Green's function with an extra term, Σ, also called the *self-energy* added to the Hamiltonian. This method of thinking about the physics as seperate uncoupled smaller systems coupled together using the Green's functions and self-energies, to calculate the important parts that we need for physical quantities, will be very useful in recursively constructing systems.

2.3 Calculating physical quantities using Green's functions

The main reason to calculate the Green's function for a system is in order to extract the physical properties of said system. In this section we discuss the what parameters we calculate using the Green's functions and how to do so.

2.3.1 Density of states

The connection between the DOS and the Green's function is one of the main reasons why Green's functions are useful. The spectral function, $\mathbf{A}$, is given from the imaginary part of the Green's function as

$$\mathbf{A}(\nu, E) = 2\mathrm{Im}\mathbf{G}(\nu, E). \tag{2.11}$$

The spectral function describes the resolution of quantum states for a given energy E, or conversely the energy resolution for a given quantum number ν. A standard derivation of the relationship between spectral function and the DOS be found in many solid state text books such as Ref. [41], namely that the spectral function is a probability function with norm 2π and thus

$$\mathrm{DOS}(E) = -\frac{1}{\pi}\mathrm{Tr}_\nu \mathrm{Im}\mathbf{G}(\nu, E). \tag{2.12}$$

Furthermore we can find the density of states for a given quantum number just by not taking the trace, which is especially useful for a tight binding model where the local orbital is a quantum number, giving us a local measure of the density of states, or LDOS as the diagonal elements

$$\mathrm{LDOS}(E, \nu) = -\frac{1}{\pi}\mathrm{Im}\mathbf{G}_{\nu,\nu}(E) \tag{2.13}$$

2.3.2 Injected spectral density

A major use of Green's functions is when studying scattering states injected from leads (or probes) into a device. We assume the Hamiltonian has a block structure similar to equation (2.7) with the lead and device Hamiltonians occupying seperate blocks. We introduce the broadening of the spectral function from a lead, $\mathbf{\Gamma}_L$, as

$$\mathbf{\Gamma}_L = -2\mathrm{Im}\mathbf{\Sigma}_L = \mathrm{i}\left(\mathbf{\Sigma}_L - \mathbf{\Sigma}_L^\dagger\right) \tag{2.14}$$

with Σ_L being the self-energy of the lead. States incoming from the lead will occupy part of the spectral function in the device given in Ref. [42], as

$$\mathbf{A}_L = \mathbf{G}_D \mathbf{\Gamma}_L \mathbf{G}_D^\dagger, \tag{2.15}$$

which can be used to track the scattered states, and in the following sections we derive results given in Ref. [42] tracking the current carried by these states.

2.3.3 Bond currents

If we are interested in the local current we can look at the time derivative of the scattered states. Let ψ_m be the projection of the scattered state on site m. The probability flux of this state is given as

$$\dot{P}_m = \frac{\partial |\psi_m|^2}{\partial t}, \tag{2.16}$$

which can be rewritten using the Schrödinger equation to

$$\dot{P}_m = \frac{-\mathrm{i}}{\hbar} \sum_n \mathbf{H}_{mn} \mathrm{Im}(\psi_m \psi_n) \equiv \sum_m \mathbf{J}_{mn} \tag{2.17}$$

where we have introduced the local probability operator between sites m and n, as

$$\mathbf{J}_{mn} = \frac{-\mathrm{i}}{\hbar} \mathbf{H}_{mn} \mathrm{Im}(\psi_m \psi_n). \tag{2.18}$$

Using the injected spectral density we rewrite the current operator as

$$\mathbf{J}_{mn} = \frac{-\mathrm{i}}{\hbar} \mathbf{H}_{mn} \mathrm{Im}\left[(\mathbf{A}_L)_{mn}\right]. \tag{2.19}$$

(2.19) gives us expression we will use to calculate the local currents or *bond currents* injected from the lead.

2.3.4 Transmission and conductance

We can calculate the transmission from one lead (or probe) to another lead which couple to each other only through a device, by using the scattered states forming the spectral density operator. The Hamiltonian can be written in block form as

$$\mathbf{H} = \begin{bmatrix} \mathbf{H}_1 & \mathbf{V}_1^\dagger & 0 \\ \mathbf{V}_1 & \mathbf{H}_D & \mathbf{V}_2^\dagger \\ 0 & \mathbf{V}_2 & \mathbf{H}_2 \end{bmatrix}. \tag{2.20}$$

and the time independent Schrödinger equation becomes

$$\mathbf{H}\psi = \begin{bmatrix} \mathbf{H}_1 & \mathbf{V}_1^\dagger & 0 \\ \mathbf{V}_1 & \mathbf{H}_D & \mathbf{V}_2^\dagger \\ 0 & \mathbf{V}_2 & \mathbf{H}_2 \end{bmatrix} \begin{pmatrix} \psi_1 \\ \psi_D \\ \psi_2 \end{pmatrix} = z \begin{pmatrix} \psi_1 \\ \psi_D \\ \psi_2 \end{pmatrix} \tag{2.21}$$

Now we consider an incoming eigenstate from the left that fulfills $\mathbf{H}_1 \phi_1 = z\phi_1$. We get a total wave which consists of the incoming wave, a reflected wave and a transmitted wave. We can write up the total wave as

$$\begin{pmatrix} \psi_1 - \phi_1 \\ \psi_D \\ \psi_2 \end{pmatrix} \tag{2.22}$$

where $\begin{pmatrix} \psi_1 \\ \psi_D \\ \psi_2 \end{pmatrix}$ fulfils equation (2.21). By dividing the Schrödinger equation into an uncoupled part and a coupling part, we get

$$\begin{bmatrix} z-\mathbf{H}_1 & 0 & 0 \\ 0 & z-\mathbf{H}_D & 0 \\ 0 & 0 & z-\mathbf{H}_2 \end{bmatrix} \begin{pmatrix} \psi_1-\phi_1 \\ \psi_D \\ \psi_2 \end{pmatrix} - \begin{bmatrix} 0 & \mathbf{V}_1^\dagger & 0 \\ \mathbf{V}_1 & 0 & \mathbf{V}_2^\dagger \\ 0 & \mathbf{V}_2 & 0 \end{bmatrix} \begin{pmatrix} \psi_1-\phi_1 \\ \psi_D \\ \psi_2 \end{pmatrix} = 0. \quad (2.23)$$

We can rewrite this equation in terms of the uncoupled Green's functions to get what is known as the Lippman-Schwinger equation (Ref. [43])

$$\begin{pmatrix} \psi_1 \\ \psi_D \\ \psi_2 \end{pmatrix} = \begin{pmatrix} \phi_1 \\ 0 \\ 0 \end{pmatrix} + \begin{bmatrix} \mathbf{g}_1 & 0 & 0 \\ 0 & \mathbf{g}_D & 0 \\ 0 & 0 & \mathbf{g}_2 \end{bmatrix} \begin{bmatrix} 0 & \mathbf{V}_1^\dagger & 0 \\ \mathbf{V}_1 & 0 & \mathbf{V}_2^\dagger \\ 0 & \mathbf{V}_2 & 0 \end{bmatrix} \begin{pmatrix} \psi_1 \\ \psi_D \\ \psi_2 \end{pmatrix} \quad (2.24)$$

We want to track the current carried by states going from lead 1 to 2, so we first look at the flux of particles in lead 2, described the time derivative of the projection operator unto said second lead,

$$\mathbf{P}_2 = \begin{bmatrix} 0 & 0 & 0 \\ 0 & 0 & 0 \\ 0 & 0 & 1 \end{bmatrix} \quad (2.25)$$

which can be found using the Heisenberg equation

$$\dot{\mathbf{P}}_2 = \frac{\mathrm{i}}{\hbar}[\mathbf{H}, \mathbf{P}_2] = \frac{\mathrm{i}}{\hbar} \begin{bmatrix} 0 & 0 & 0 \\ 0 & 0 & \mathbf{V}_2^\dagger \\ 0 & -\mathbf{V}_2 & 0 \end{bmatrix} \quad (2.26)$$

Now we are interested in the probability current of the scattered states originating in lead 1 and ending up in lead 2, carried by some state ψ_m

$$\mathbf{j}_{mm} = \langle \psi_m | \dot{\mathbf{P}}_2 | \psi_m \rangle \quad (2.27)$$

$$= \frac{\mathrm{i}}{\hbar} \langle \psi_{m,D} | \mathbf{V}_2^\dagger | \psi_{m,2} \rangle - \langle \psi_{m,2} | \mathbf{V}_2 | \psi_{m,D} \rangle . \quad (2.28)$$

Using the Lippman-Schwinger equation (2.24), we can find that $|\psi_{m,2}\rangle = \mathbf{g}_2 \mathbf{V}_2 |\psi_{m,D}\rangle$, yielding

$$\mathbf{j}_{mm} = \frac{\mathrm{i}}{\hbar} \langle \psi_{m,D} | \mathbf{V}_2^\dagger \mathbf{g}_2 \mathbf{V}_2 | \psi_{m,D} \rangle - \langle \psi_{m,D} | \mathbf{V}_2^\dagger \mathbf{g}_2^\dagger \mathbf{V}_2 | \psi_{m,D} \rangle \quad (2.29)$$

$$= \frac{1}{\hbar} \langle \psi_{m,D} | \mathbf{\Gamma}_2 | \psi_{m,D} \rangle \quad (2.30)$$

To get the full particle current we just need to sum all the ortogonal, energy-normalized scattering states. Furthermore we know any scattered state originating lead 1 can be written in terms of the injected spectral density, and hence we get the transmission from 1 to 2 to be

$$T_{21} = \sum_m \mathbf{j}_{mm} = \mathrm{Tr}\left(\mathbf{A}_1 \mathbf{\Gamma}_2\right) = \mathrm{Tr}\left(\mathbf{G}_D \mathbf{\Gamma}_1 \mathbf{G}_D^\dagger \Gamma_2\right). \quad (2.31)$$

The transmission can for mesoscopic systems be directly linked to the conductance, G, via the Landauer formula

$$G = \frac{2e^2}{\hbar} T \tag{2.32}$$

however, we will stick to calculating the transmission when characterizing the electronics.

2.4 Boundary conditions

The limitation on the system size caused by the computational limitations discussed in appendix A, causes boundaries to play a large role. In this section we dicuss the standard boundary conditions, how they differ and how they match up to physical systems. In particular we discuss the effect of each boundary condition and how they can cause artefacts in our simulationsm.

2.4.1 Periodicity, finiteness, semi infinite

Finite:
The most simple boundary condition we can imagine is finiteness. Basically the system ends suddenly at the boundaryor egde. For graphene the exact edge has a large effect on the electronics structure, as discussed in chapter 3, and unless the actual physical system we want to look at has edges then we have to extend the system size to minimize the effect of the edges. This method can be useful when considering disordered systems as it is the computationally cheapest boundary condition, and for randomly disordered systems you might want several calculations of the same system with different configurations of disorder to calculate statistical quantities, and furthermore we do not want to introduce artificial order in form of the next type of boundary condition, periodicity.
Periodic:
The second boundary condition that immediately comes to mind is the periodic boundary, in which we require that all physical parameters of the system are repeated regualarly. The wave function which is not directly measureable can at most pick up a phase, which leads to two different kinds of periodic boundaries. The open periodic boundary condition, where the wavefunction picks up a non-zero phase, uses the Bloch theorem, and will thus give rise to an extra periodicity parameter usually denoted by k, per direction with periodic boundary conditions and corresponds to infinite systems. A different approach is the closed periodic boundary where we require the wave function to be periodic as well with no extra phase picked up, and which corresponds to finite systems with edges "glued" together . In this thesis we refer to the open infinite type of periodicity when using the term periodic, unless otherwise stated.
Semi infinite:
The semi infinite boundary condition corresponds to a mix of the finite and open periodic boundary condition, but harder to implement directly in the Hamiltonian. However, we can use the Dyson equation to construct the Green's functions for semi infinite system in certain situation. This is especially useful when generating leads since they usually resemble a semi infinite structure, with one end connecting to a device.
Figure 2.1 shows different examples of physical structures which has these types of

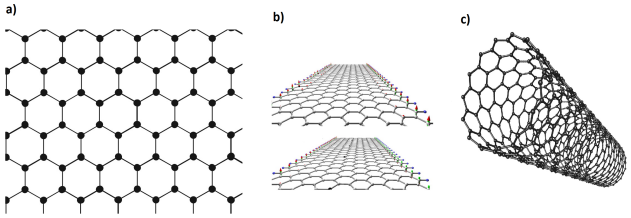

FIGURE 2.1: Carbon structures with different periodicities: a) Graphene sheet[3], Open periodic , b) GNR[13], Finite and c) Carbon nanotube, Closed periodic

boundary conditions. Other boundary conditions exists as well, but we will deal mainly combinations of these 3 to get systems resembling physical systems.

2.5 Left-Right Geometry

Left-Right geometries are an important simple subset of general systems that can be treated recursively. Imagine some finite subset of a system that can be divided into slices (or layers) that only couple to the two neighbouring slices. We call slices of this type *principal layers*, and we will call this subsystem the device, and furthermore we require that the device only couples to the outside through the two end pricipal layers, see the illustration in figure 2.2 for a schematic of the system. An example of this type of system could be a graphene nanoribon connected to two leads, one at each end of the ribbon. The Hamiltonian for full system becomes

$$\mathbf{H} = \begin{bmatrix} \mathbf{H}_L & \mathbf{V}_L^\dagger & 0 \\ \mathbf{V}_L & \mathbf{H}_D & \mathbf{V}_R^\dagger \\ 0 & \mathbf{V}_R & \mathbf{H}_R \end{bmatrix} \tag{2.33}$$

with a tridiagonal device Hamiltonian

$$\mathbf{H}_D = \begin{bmatrix} \mathbf{H}_1 & \mathbf{V}_1^\dagger & 0 & 0 & 0 & \cdots & 0 \\ \mathbf{V}_1 & \mathbf{H}_2 & \mathbf{V}_2^\dagger & 0 & 0 & \cdots & 0 \\ 0 & \mathbf{V}_2 & \mathbf{H}_3 & \mathbf{V}_3^\dagger & 0 & \cdots & 0 \\ \vdots & \ddots & \ddots & \ddots & \ddots & \ddots & \vdots \\ 0 & \ddots & \ddots & \mathbf{V}_{N-3} & \mathbf{H}_{N-2} & \mathbf{V}_{N-2}^\dagger & 0 \\ 0 & 0 & \cdots & 0 & \mathbf{V}_{N-2} & \mathbf{H}_{N-1} & \mathbf{V}_{N-1}^\dagger \\ 0 & 0 & \cdots & 0 & 0 & \mathbf{V}_{N-1} & \mathbf{H}_N \end{bmatrix} \tag{2.34}$$

and with

$$\mathbf{V}_L = \begin{pmatrix} \mathbf{V}_l \\ 0 \\ \vdots \\ 0 \end{pmatrix} \text{ and } \mathbf{V}_R^\dagger = \begin{pmatrix} 0 \\ \vdots \\ 0 \\ \mathbf{V}_r^\dagger \end{pmatrix}. \tag{2.35}$$

In order to calculate the LDOS we need the diagonal elements of the Green's function, and in order to calculate the injected spectral density from a lead, we need to the Green's functions that connect each slice to that lead. We will later discuss an algorithm that lets us calculate the essential Green's functions needed for those two calculations.

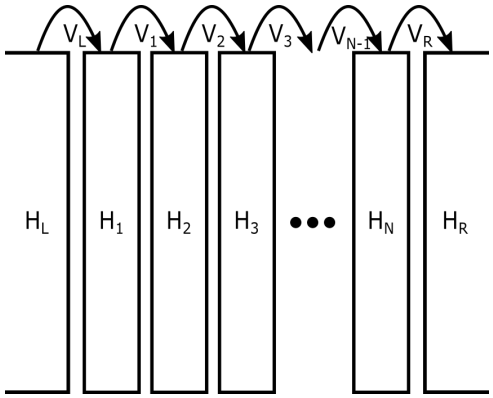

FIGURE 2.2: Schematic of left-right geometry

2.6 Green's functions patching

A very different set of boundary condition can be made if we consider what is known as patching (see Ref. [44]). The goal is to describe interaction with an infinite material by introducing some self-energy without introducing edges or periodicity. The fundamental idea here is limited interaction range and it hedges on a local description of the material. When a system only has local interactions certain parts can be "cut out" and replaced without changing the outside Hamiltonian. It requires us to be able to divide the Hamiltonian of our system into 3 parts: outside, boundary and patch, where the physics we are interested in such as interactions probes or local disorder all can be described by the patch Hamiltonian. The Hamiltonian can then be written in block form as

$$\mathbf{H}_{\text{system}} = \begin{bmatrix} \mathbf{H}_O & \mathbf{V}_{O,B} & 0 \\ \mathbf{V}_{B,O} & \mathbf{H}_B & \mathbf{V}_{B,P} \\ 0 & \mathbf{V}_{P,B} & \mathbf{H}_P \end{bmatrix} \tag{2.36}$$

where $\mathbf{V}_{B,O}$ and $\mathbf{V}_{O,B}$ do not depend on $\mathbf{H}_P$. Thus we can write the system as

$$\mathbf{H}_{\text{system}} = \mathbf{H}_0 + \mathbf{V} = \begin{bmatrix} \mathbf{H}_O & \mathbf{V}_{O,B} & 0 \\ \mathbf{V}_{B,O} & \mathbf{H}_B & 0 \\ 0 & 0 & \mathbf{H}_P \end{bmatrix} + \begin{bmatrix} 0 & 0 & 0 \\ 0 & 0 & \mathbf{V}_{B,P} \\ 0 & \mathbf{V}_{P,B} & 0 \end{bmatrix}. \tag{2.37}$$

Notice the slightly different division of the system into uncoupled parts and coupling than in previous cases. The full system will have the fully coupled Green's functions

$$\begin{bmatrix} \mathbf{G}_{O,O} & \mathbf{G}_{O,B} & \mathbf{G}_{O,P} \\ \mathbf{G}_{O,B} & \mathbf{G}_{B,B} & \mathbf{G}_{B,P} \\ \mathbf{G}_{O,P} & \mathbf{G}_{B,P} & \mathbf{G}_{P,P} \end{bmatrix} \tag{2.38}$$

and uncoupled Green's functions

$$\begin{bmatrix} \mathbf{g}_{O,O} & \mathbf{g}_{O,B} & 0 \\ \mathbf{g}_{B,O} & \mathbf{g}_{B,B} & 0 \\ 0 & 0 & \mathbf{g}_{P,P} \end{bmatrix}. \tag{2.39}$$

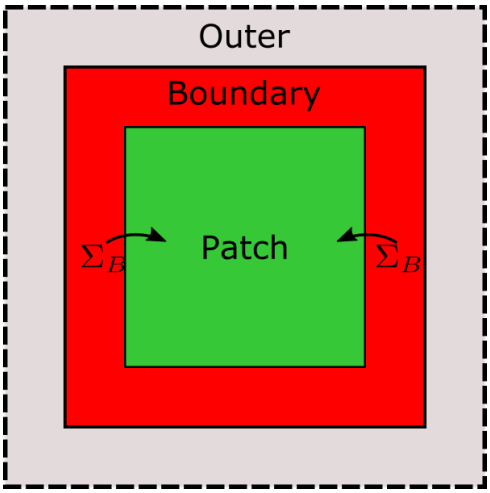

FIGURE 2.3: Schematic of patching setup

We are interested in the physical behaviour of the patch, i.e. the fully coupled Green's function, $\mathbf{G}_{P,P}$. Using the Dyson equation (2.6) we get that

$$\mathbf{G}_{P,P} = \mathbf{g}_{P,P} + \mathbf{g}_{P,P}\mathbf{V}_{P,B}\mathbf{G}_{B,P} \tag{2.40}$$
$$\mathbf{G}_{B,P} = \mathbf{g}_{B,B}\mathbf{V}_{B,P}\mathbf{G}_{P,P} \tag{2.41}$$
$$\mathbf{G}_{P,P} = \mathbf{g}_{P,P} + \mathbf{g}_{P,P}\mathbf{V}_{P,B}\mathbf{g}_{B,B}\mathbf{V}_{B,P}\mathbf{G}_{P,P} \tag{2.42}$$

which allows us to identify the important self-energy term as

$$\mathbf{\Sigma}_B = \mathbf{V}_{P,B}\mathbf{g}_{B,B}\mathbf{V}_{B,P} \tag{2.43}$$

giving us the usual fully coupled Green's function as

$$\mathbf{G}_{P,P} = \left[z\mathbb{1} - \mathbf{H}_P - \mathbf{\Sigma}_B\right]^{-1}. \tag{2.44}$$

Since $\mathbf{g}_{bb}$ is independent only depends on the parts of the Hamiltonian which we require to be unaffected by the patch Hamiltonian, we can use any patch Hamiltonian to solve for $\mathbf{\Sigma}_B$. This is the key to the patching method. Now assume that there exists a patch Hamiltonian, $\mathbf{H}^0_P$ for which we can calculate the fully coupled Green's function of the *entire* system. Using the Dyson equation (2.6) gives us

$$\mathbf{G}^0_{B,B} = \mathbf{g}^0_{B,B} + \mathbf{g}^0_{B,B}\mathbf{V}^0_{B,P}\mathbf{G}^0_{P,B} \tag{2.45}$$
$$\mathbf{G}^0_{B,B} = \mathbf{g}^0_{B,B}\left(\mathbb{1} + \mathbf{V}^0_{B,P}\mathbf{G}^0_{P,B}\right) \tag{2.46}$$
$$\mathbf{g}^0_{B,B} = \mathbf{G}^0_{B,B}\left(\mathbb{1} + \mathbf{V}^0_{B,P}\mathbf{G}^0_{P,B}\right)^{-1}, \tag{2.47}$$

and since the uncoupled system is independent of the patch we have $\mathbf{g}^0_{B,B} = \mathbf{g}_{B,B}$. We can use the fully solvable system to find the solution for patched system, essentially cutting out part of the known system and replacing it with something different. A schematic of the typical patching setup is shown in figure 2.3.

One type of system where the fully coupled Green's function can be calculated are fully periodic, or *pristine*, systems. The patching method enables us to essentially substitute part of a pristine system with some different, enabling us to calculate the effect of local disorder without the introduction of artifacts coming from edges or periodicity. We can also introduce multiple patches containing different disorder in

order to calculate disorder interaction or probes to solve scattering problems. We will discuss techniques to calculate these types of system in the following subsections, starting with how to efficiently calculate pristine Green's functions.

2.6.1 Pristine system Green's functions

Calculating the pristine system Green's functions for any periodic structure presents the single biggest challenge in using the patching method. In this section we discuss graphene specific methods and approaches that can be used for general periodic systems.

The most straightforward method is directly replacing the patch with your pristine system and implementing periodic boundary conditions. This allows a full super cell calculation to be performed, from which the required real-space Green's functions can be obtained by k-averaging. For large systems this can sometimes be unfeasible, especially if multiple patches are included and seperated from each other by large distances.
However, since pristine systems are periodic, all information is obtainable from a single unit cell, instead of a full supercellm though it involves a little more bookkeeping. Let $\mathbf{H}(k)$ be a Hamiltonian for a single unit cell, and let $\mathbf{G}(E,k)$ be the corresponding Green's function. Since the system is periodic the Green's function components between two cells with positions $\mathbf{R}_i$ and $\mathbf{R}_j$, can thus only depend on the difference in position of the two cells $\mathbf{R}_j - \mathbf{R}_i$, and thus in real space the Green's function becomes just the inverse Fourier component given as

$$\mathbf{G}(E, R_j - R_i) = \int \mathrm{d}\mathbf{k}\mathbf{G}(E,\mathbf{k})\mathrm{e}^{\mathbf{i}\mathbf{k}\cdot(R_j - R_i)}. \tag{2.48}$$

If a closed analytical expression is known for $\mathbf{G}(E,k)$, this integration can be made directly, and though it can be computationally hard (depending on the dimensionality of k), the pristine system remains the same, and thus the elements $\mathbf{G}_{m,n}(E,k)$ can be saved and used for several distinct calculations. However several efficient algorithms exist to calculate the Fourier transform from sampled data, called FFTs, so a different approach where the Green's function is sampled in k-space, and used to calculate the Fourier transform is also possible. FFT techniques are implemented and discussed in chapter 7 in order test them.

2.6.2 Multiple patches

A strength of the patching method is that the generalisation to multiple patches is straightforward. The general structure of the Hamiltonian becomes

$$\mathbf{H}_{\text{system}} = \begin{bmatrix} \mathbf{H}_O & \mathbf{V}_{O,B} & 0 & 0 & 0 & \cdots & 0 \\ \mathbf{V}_{B,O} & \mathbf{H}_B & \mathbf{V}_{B,P1} & \mathbf{V}_{B,P2} & \mathbf{V}_{B,P3} & \cdots & \mathbf{V}_{B,PN} \\ 0 & \mathbf{V}_{P1,B} & \mathbf{H}_{P1} & 0 & 0 & \cdots & 0 \\ 0 & \mathbf{V}_{P2,B} & 0 & \mathbf{H}_{P2} & 0 & \ddots & 0 \\ 0 & \mathbf{V}_{P3,B} & 0 & 0 & \mathbf{H}_{P3} & \ddots & 0 \\ 0 & \vdots & 0 & \vdots & \vdots & \ddots & \vdots \\ 0 & \mathbf{V}_{PN,B} & 0 & 0 & 0 & \cdots & \mathbf{H}_{PN} \end{bmatrix}. \tag{2.49}$$

By treating the collection of patches as a single large patch, with coupling

$$\mathbf{V} = \begin{bmatrix} \mathbf{V}_{B,P1} & \mathbf{V}_{B,P2} & \mathbf{V}_{B,P3} & \cdots & \mathbf{V}_{B,PN} \end{bmatrix}$$

the generalisation is complete, even if the patches are not directly coupled to each other. It is worth noting that the boundary now incompases all of the patches, and so the elements of $\mathbf{G}_{BB}$ and $\mathbf{G}_{PB}$ includes Green's functions connecting the boundary of each patch to each other and all other patches as well. This can give rise to rapidily oscillating Fourier integrals when patches are far from each other, something discussed in appendix A. Multiple patches are particularly useful when we consider things separated by large distances, such as a probe and a device, in an otherwise pristine sheet of material.

2.6.3 Patching in left-right geometries

Using the patched method in left-right geometries is a special case where the outer system can be split into two uncoupled parts. The system that we consider are some of the same systems as discussed in section 2.5. Many of these systems can be solved using recursive techniques discussed later in this chapter in order to calculate the uncoupled Green's functions directly, however it can be advantageous to apply the patching idea as well, i.e. the idea that some part of the system is substituted by something else. E.g. in the case of the nanoconstriction with ultra wide leads it is straightforward to describe the system as an infinite sheet with a thin slice cut out and substituted by a narrow ribbon.

In case of periodic semi infinite leads we can even calculate the self energy from the leads using the pristine simple unit cell. In case of the left-right geometry we can rewrite the Hamiltonian as

$$\mathbf{H}_{\text{system}} = \begin{bmatrix} \mathbf{H}_L & \mathbf{V}_{L,BL} & 0 & 0 & 0 \\ \mathbf{V}_{BL,L} & \mathbf{H}_{BL} & \mathbf{V}_{BL,P} & 0 & 0 \\ 0 & \mathbf{V}_{P,BL} & \mathbf{H}_P & \mathbf{V}_{P,BR} & 0 \\ 0 & 0 & \mathbf{V}_{BR,P} & \mathbf{H}_{BR} & \mathbf{V}_{BR,R} \\ 0 & 0 & 0 & \mathbf{V}_{R,BR} & \mathbf{H}_R \end{bmatrix}. \tag{2.50}$$

Similar to before the patching equations becomes

$$\mathbf{G}_{P,P} = \left[z\mathbb{1} - \mathbf{H}_P - \mathbf{\Sigma}_R - \mathbf{\Sigma}_L\right]^{-1} \tag{2.51}$$

with

$$\mathbf{\Sigma}_R = \mathbf{V}_{P,R}\mathbf{g}_{R,R}\mathbf{V}_{R,P} \tag{2.52}$$
$$\mathbf{\Sigma}_L = \mathbf{V}_{P,L}\mathbf{g}_{L,L}\mathbf{V}_{L,P} \tag{2.53}$$

and

$$\mathbf{g}_{R,R} = \mathbf{G}^0_{R,R}\left(\mathbb{1} + \mathbf{V}^0_{R,P}\mathbf{G}^0_{P,R}\right)^{-1} \tag{2.54}$$
$$\mathbf{g}_{L,L} = \mathbf{G}^0_{L,L}\left(\mathbb{1} + \mathbf{V}^0_{L,P}\mathbf{G}^0_{P,L}\right)^{-1}. \tag{2.55}$$

The notable difference between the left-right patching and regular patching is the division of the boundary into a left and right part which can be dealt with individually as long as the Green's functions for the uncoupled left and right are known.

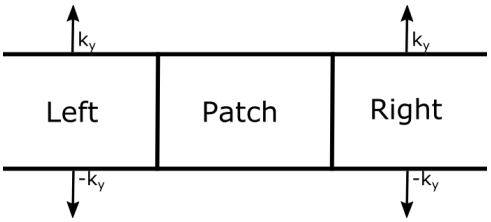

FIGURE 2.4: Schematic of patching setup in left-right geometry

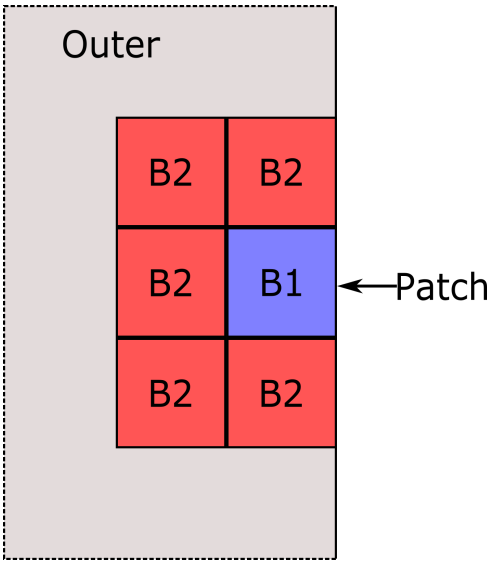

FIGURE 2.5: Schematic of left lead connection to device patch

2.6.4 Self-energy for semi-infinite systems using patching

If we want to calculate the self-energy of semi-infinite leads independently of our device, we can use patching techniques. A situation where this could become useful is if we have periodic semi-infinite leads connected to a finite patch as shown in figure 2.4. Lets assume that the device patch is connected to the lead through a boundary area, B1, which connects to the rest of the lead through a secondary boundary layer B2, as shown in figure 2.5. Our goal will be to find the patching self-energy from B2 onto B1, $\mathbf{\Sigma}_{B2}$, which can then be included in the device patch, and then connect B1 using the patching equations (2.43)+(2.47), which becomes

$$\mathbf{\Sigma}_{B2} = \mathbf{V}_{B1,B2}\mathbf{g}_{B2,B2}\mathbf{V}_{B2,B1} \tag{2.56}$$

$$\mathbf{g}_{B2,B2} = \mathbf{G}^0_{B2,B2}\left(\mathbb{1} + \mathbf{V}^0_{B2,B1}\mathbf{G}^0_{B1,B2}\right)^{-1}. \tag{2.57}$$

The challenge will be to find expressions for these Green's function elements. We will essentially decouple $B1$ from the rest of the semi-infinite structure. Since the lead is semi-infinite we will assume that we can make a unit cell that includes $B1$ and $B2$, which is the final most right cell in the semi-infinite direction, and is repeated infinitely in both the transverse directions (up and down). This allows us introduce periodic boundary condtions in the transverse direction introducing a k_y Fourier parameter. Lets assume that we can find the full Green's function as a function of k_y

just for the right most cell, which we will call $\mathbf{G}_{00}(k_y)$, where

$$\mathbf{G}_{00}(k_y) = \begin{bmatrix} \mathbf{G}_{OO}(k_y) & \mathbf{G}_{OB2}(k_y) & \mathbf{G}_{OB1}(k_y) \\ \mathbf{G}_{B2O}(k_y) & \mathbf{G}_{B2B2}(k_y) & \mathbf{G}_{B2B1}(k_y) \\ \mathbf{G}_{B1O}(k_y) & \mathbf{G}_{B1B2}(k_y) & \mathbf{G}_{B1B1}(k_y) \end{bmatrix} \tag{2.58}$$

we then do the inverse fourier transform to find the real space representation for the internal Green's functions

$$\mathbf{G}_{00}(0) = \frac{1}{2\pi}\int_0^{2\pi} \mathrm{d}k_y \mathbf{G}_{00}(k_y)\mathrm{e}^{\mathrm{i}k_y\cdot 0} \tag{2.59}$$

$$= \begin{bmatrix} (\mathbf{G}_{OO})_{00} & (\mathbf{G}_{OB2})_{00} & (\mathbf{G}_{OB1})_{00} \\ (\mathbf{G}_{B2O})_{00} & \mathbf{G}_{B2B2} & \mathbf{G}_{B2B1} \\ (\mathbf{G}_{B1O})_{00} & \mathbf{G}_{B1B2} & \mathbf{G}_{B1B1} \end{bmatrix} \tag{2.60}$$

yielding us the two Green's function components that we need. One way we can calculate $\mathbf{G}_{00}(k_y)$ is using a recursive method described in section 2.7.2. We will also discuss how to calculate the same thing using patching methods.

2.6.5 Green's functions for semi-infinite systems from pristine unit cells

In order to use the patching method in these left right geometries, with semi-infinite left and right parts, we need some way of calculating the pristine Green's functions for these semi infinite systems. A way of doing this using patching methods exists using only information contained in a single unit cell of the pristine material. The idea is essentially to take a fully periodic system, and cut out a slice wide enough that the left and right parts of the system no longer interacts.

We focus on a left semi-infinite system but a right type system has an equivalent derivation. A semi-infinite system has two main directions. The direction in which it is semi-infinite, which will call x and a fully periodic direction which will call y. Now we consider a fully periodic system with Hamiltonian $\mathbf{H}(k_x, k_y)$ with k_x and k_y being the periodicity numbers in the corresponding directions. Let a_x and a_y be the real space lattice vectors in the x and y directions. We can construct the necessary realspace coupling matrices between cells directly from the Hamiltonian as the inverse Fourier component corresponding to the separation. If the separation between two cells is (ma_x, na_y), the coupling matrix between those becomes

$$\mathbf{V}(ma_x, na_y) = \frac{1}{4\pi^2}\int_0^{2\pi}\mathrm{d}k_x \int_0^{2\pi}\mathrm{d}k_y \mathrm{e}^{\mathrm{i}(mk_x+nk_y)}\mathbf{H}(k_x, k_y). \tag{2.61}$$

If the coupling matrices are not easily extracted and span several unit cells, this methid can be used to get the required coupling matrices. These can also be used to construct principal cells from single unit cells if needed.

We can also find the full Green's function for the pristine system by direct inversion of periodic Hamiltonian

$$\mathbf{G}(k_x, k_y) = \left[z\mathbb{1} - \mathbf{H}(k_x, k_y)\right]^{-1}. \tag{2.62}$$

We will assume that the unit cell is a principal cell (and only couples to the nearest neighbouring cells), otherwise one needs to extend the unit cell to a principal unit cell. Using the patching equation (2.47) we can uncouple a principle layer as shown in figure 2.6. We find the relevant Green's functions by doing an inverse Fourier

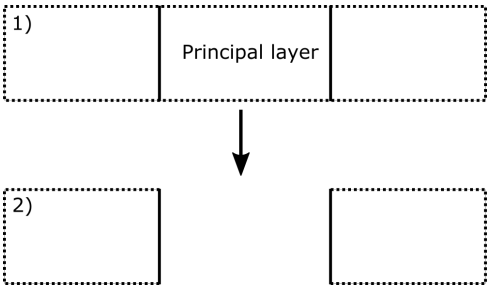

FIGURE 2.6: Uncoupling left and right sides by removing a principal layer

transform over k_x. The equation for the left semi-infinite part reads

$$(\mathbf{g}_{L,L})_{00}(k_y) = (\mathbf{G}_{L,L})^0_{00}(k_y)\left(\mathbb{1} + \mathbf{V}^0_{L,P}(k_y)(\mathbf{G}_{P,L})^0(k_y)\right)^{-1}, \tag{2.63}$$

and since all cell are principal, we have

$$(\mathbf{G}^0_{L,L})_{00}(k_y) = \mathbf{G}(0,k_y) = \frac{1}{2\pi}\int_0^{2\pi} \mathrm{d}k_x \mathbf{G}(k_x,k_y) \tag{2.64}$$

$$\mathbf{V}^0_{L,P}(k_y) = \mathbf{V}(-a_x,k_y) = \frac{1}{2\pi}\int_0^{2\pi} \mathrm{d}k_x \mathbf{H}(k_x,k_y)e^{-\mathrm{i}k_x} \tag{2.65}$$

$$\mathbf{G}^0_{P,L}(k_y) = \mathbf{G}(a_x,k_y) = \frac{1}{2\pi}\int_0^{2\pi} \mathrm{d}k_x \mathbf{G}(k_x,k_y)e^{\mathrm{i}k_x}. \tag{2.66}$$

2.7 Recursive methods

One of the strengths of the Dyson equation lies in the ability to find the Green's function from uncoupled parts. This section discusses methods to extract important parts of the full Green's function recursively from uncoupled subsystem Green's functions. A large range of these methods are discussed in Ref. [45, 46].

2.7.1 Double sweep algorithm

The double sweep algorithms is designed to extract important parts of the Green's function from left-right type geometries. In principle since the device is required to finite, we can, if the computational power is available, directly invert the Hamiltonian in order to calculate the full Green's function. However there exists a method to extract only the parts of the Green's function we need which is computationally cheaper than the full inversion. In essence we use the Dyson equation to first couple the device to the right side Hamiltonian, and later to left side Hamiltonian hence the name "double sweep". Note that a single sweep is actually enough to connect the left and right to each other, but in order for the entire device to be fully connected to both sides a full double sweep is needed. We will denote the Green's functions of the i'th slice, coupled only to the right as $\mathbf{g}^R_i$. We will assume a total N slices, and we will number them from left to right as in figure 2.2. For the right most slice we have

$$\mathbf{g}^R_N = \left(z\mathbb{1} - \mathbf{H}_N - \mathbf{\Sigma}_R\right)^{-1}, \tag{2.67}$$

with

$$\mathbf{\Sigma}_R = \mathbf{V}^\dagger_R \mathbf{G}_R \mathbf{V}_R \tag{2.68}$$

with $\mathbf{G}_R$ being the full Green's function corresponding to $\mathbf{H}_R$. The remaining partially coupled Green's functions can now be found recursively using

$$\mathbf{g}^R_{N-i} = \left(z\mathbb{1} - \mathbf{H}_{N-i} - \mathbf{\Sigma}^R_{N-i+1}\right)^{-1}, \tag{2.69}$$

with

$$\mathbf{\Sigma}^R_{N-i+1} = \mathbf{V}^\dagger_{N-i}\mathbf{g}^R_{N-i+1}\mathbf{V}_{N-i}. \tag{2.70}$$

For the left most slice we can include the self-energy from the left to fully to get the fully coupled Green's function,

$$\mathbf{G}_{1,1} = \left(z\mathbb{1} - \mathbf{H}_1 - \mathbf{\Sigma}^R_2 - \mathbf{\Sigma}_L\right)^{-1}, \tag{2.71}$$

with

$$\mathbf{\Sigma}_L = \mathbf{V}_L\mathbf{G}_L\mathbf{V}^\dagger_L \tag{2.72}$$

In order to get the fully connected Green's function parts that we need from each slice, we simply apply the Dyson equation (2.6) again, and get the recursive relations

$$\mathbf{G}_{i,1} = \mathbf{g}^R_i\mathbf{V}_i\mathbf{G}_{i-1,1} \tag{2.73}$$

$$\mathbf{G}_{i,i} = \mathbf{g}^R_i + \mathbf{g}^R_i\mathbf{V}_i\mathbf{G}_{i-1,i-1}\mathbf{V}^\dagger_i\mathbf{g}^R_i \tag{2.74}$$

whichs allows us to calculate both the injected spectral density and the LDOS for each slice. This algortihm does present us with the problem of calculating the full Green's function of the left and right systems, or at least the the part that needs to be included to calculate the self-energies.

2.7.2 The Rubio-Sancho Method

If the the left and right systems are each made up of a semi infinite stacks identical principal layers, we only need the Green's function of the outer most layers, the so called surface Green's functions. An iterative scheme exists, first published in Ref. [47]. This method was originally designed to efficiently calculate the surface Green's function of solids consisting of stacked layers. This means that the Hamiltonian can be written as

$$\mathbf{H} = \begin{bmatrix} \mathbf{h}_s & \mathbf{V}^\dagger & 0 & 0 & 0 & \cdots \\ \mathbf{V} & \mathbf{h} & \mathbf{V}^\dagger & 0 & 0 & \cdots \\ 0 & \mathbf{V} & \mathbf{h} & \mathbf{V}^\dagger & 0 & \cdots \\ \vdots & \ddots & \ddots & \ddots & \ddots & \ddots \end{bmatrix} \tag{2.75}$$

where we have denoted the Hamiltonian for the surface layer individually even though it is identical to the rest of the layers simply because it will help us in describing the algorithm. We can write up the Green's function equation (2.5) as

$$\begin{bmatrix} z\mathbb{1} - \mathbf{h}_s & \mathbf{V}^\dagger & 0 & 0 & 0 & \cdots \\ \mathbf{V} & z\mathbb{1} - \mathbf{h} & \mathbf{V}^\dagger & 0 & 0 & \cdots \\ 0 & \mathbf{V} & z\mathbb{1} - \mathbf{h} & \mathbf{V}^\dagger & 0 & \cdots \\ \vdots & \ddots & \ddots & \ddots & \ddots & \ddots \end{bmatrix} \begin{bmatrix} \mathbf{G}_{00} & \mathbf{G}_{01} & \mathbf{G}_{02} & \cdots \\ \mathbf{G}_{10} & \mathbf{G}_{11} & \mathbf{G}_{12} & \cdots \\ \mathbf{G}_{20} & \mathbf{G}_{21} & \mathbf{G}_{22} & \cdots \\ \vdots & \vdots & \vdots & \ddots \end{bmatrix} = \mathbb{1}. \tag{2.76}$$

We are only interested in calculating the surface Green's function, $\mathbf{G}_{00}$, so we look at part of the part of the block product that involvese the first column of the Green's

function

$$\begin{bmatrix} z\mathbb{1}-\mathbf{h}_s & \mathbf{V}^\dagger & 0 & 0 & 0 & \cdots \\ \mathbf{V} & z\mathbb{1}-\mathbf{h} & \mathbf{V}^\dagger & 0 & 0 & \cdots \\ 0 & \mathbf{V} & z\mathbb{1}-\mathbf{h} & \mathbf{V}^\dagger & 0 & \cdots \\ \vdots & \ddots & \ddots & \ddots & \ddots & \ddots \end{bmatrix} \begin{bmatrix} \mathbf{G}_{00} \\ \mathbf{G}_{10} \\ \mathbf{G}_{20} \\ \vdots \end{bmatrix} = \begin{bmatrix} \mathbb{1} \\ 0 \\ 0 \\ \vdots \end{bmatrix}. \tag{2.77}$$

This is a infinite set of linear equations which we can reduce by using the every second equation to eliminate 1 variable, (the rows involving $\mathbf{G}_{2n+1,0}$), giving us a new infinite set of equations. Doing this j times we can rewrite the remaing equations as

$$\begin{bmatrix} z\mathbb{1}-\varepsilon_{sj} & -\alpha_j & 0 & 0 & 0 & \cdots \\ -\beta_j & z\mathbb{1}-\varepsilon_j & -\alpha_j & 0 & 0 & \cdots \\ 0 & -\beta_j & z\mathbb{1}-\varepsilon_j & -\alpha_j & 0 & \cdots \\ \vdots & \ddots & \ddots & \ddots & \ddots & \ddots \end{bmatrix} \begin{bmatrix} \mathbf{G}_{00} \\ \mathbf{G}_{2^j0} \\ \mathbf{G}_{2\cdot 2^j0} \\ \vdots \end{bmatrix} = \begin{bmatrix} \mathbb{1} \\ 0 \\ 0 \\ \vdots \end{bmatrix}. \tag{2.78}$$

The equations for the first two rows gives us

$$\mathbb{1} = (z\mathbb{1}-\varepsilon_{sj})\mathbf{G}_{00} - \alpha_j\mathbf{G}_{2^j0} \tag{2.79}$$
$$0 = -\beta_j\mathbf{G}_{00} + (z\mathbb{1}-\varepsilon_s)\mathbf{G}_{2^j0} - \alpha_j\mathbf{G}_{2\cdot 2^j0} \tag{2.80}$$

eliminating $\mathbf{G}_{2^j0}$ gives us

$$\mathbb{1} = (z\mathbb{1}-\varepsilon_{sj})\mathbf{G}_{00} - \alpha_j(z\mathbb{1}-\varepsilon_s)^{-1}\left(\beta_j\mathbf{G}_{00} + \alpha_j\mathbf{G}_{2\cdot 2^j0}\right) \tag{2.81}$$
$$\mathbb{1} = (z\mathbb{1}-\varepsilon_{sj} - \alpha_j(z\mathbb{1}-\varepsilon_s)^{-1}\beta_j)\mathbf{G}_{00} - \alpha_j(z\mathbb{1}-\varepsilon_s)^{-1}\alpha_j\mathbf{G}_{2\cdot 2^j0} \tag{2.82}$$
$$\mathbb{1} = (z\mathbb{1}-\varepsilon_{s(j+1)})\mathbf{G}_{00} - \alpha_{j+1}\mathbf{G}_{2\cdot 2^j0} \tag{2.83}$$

allowing us to identify α_{j+1} and $\varepsilon_{s(j+1)}$, and it is straightforward to show using slightly more equations that

$$\alpha_{j+1} = \alpha_j g_{bj}\alpha_j \tag{2.84}$$
$$\beta_{j+1} = \beta_j g_{bj}\beta_j \tag{2.85}$$
$$\varepsilon_{j+1} = \varepsilon_j + \alpha_j g_{bj}\beta_j + \beta_j g_{bj}\alpha_j \tag{2.86}$$
$$\varepsilon_{s(j+1)} = \varepsilon_{sj} + \alpha_j g_{bj}\beta_j, \tag{2.87}$$

with $g_{bj} = (\mathbb{1}-\varepsilon_j)^{-1}$. The effective couplings α_j and β_j will tend towards zero as j increases since the layers they couple will grow further apart. Because of this the equation corrsponding to the first row of the leftmost matrix will fulfil

$$\mathbb{1} = (z\mathbb{1}-\varepsilon_{sj})\mathbf{G}_{00} - \alpha_j\mathbf{G}_{2^j0} \to (z\mathbb{1}-\varepsilon_{sj})\mathbf{G}_{00} \tag{2.88}$$

and thus

$$(z\mathbb{1}-\varepsilon_{sj})^{-1} \to \mathbf{G}_{00}. \tag{2.89}$$

Similarly we can get the bulk Green's function, as $g_{bj} \to \mathbf{G}_{\text{Bulk}}$, where $\mathbf{G}_{\text{Bulk}} = \mathbf{G}_{nn}$ for $n \to \infty$. Since we know

$$\alpha_0 = \mathbf{V}^\dagger \tag{2.90}$$
$$\beta_0 = \mathbf{V} \tag{2.91}$$
$$\varepsilon_0 = \mathbf{h} \tag{2.92}$$
$$\varepsilon_{s0} = \mathbf{h}_s, \tag{2.93}$$

we can recursively find the surface Green's function, that we need for the left-right type geometries.

2.7.3 Adaptive recursive algorithm

It is useful to be able to efficiently divide a finite system into principle layers or slices, if possible. Several methods of tridiagonlisation exists, but this method allows for easy constraints. We will refer to these slices as "cells" since they no longer resemble neither layers nor slices. Given a list of sites L_{sites} and a Hamiltonian, we will construct these cells. This algorithm is also presented in Ref. [44].
We need a starting point, a list of starting sites to include in the first cell, which we call L_0. We remove these sites from the total list giving us a list of remaining sites L_0^R. The recursive algorithm is as follows for the i'th step.

1. Select any site, m, in L_{i-1}^R where $\mathbf{H}_{mn} \neq 0$ for any site, n, in L_{i-1}
2. Put those sites in L_i
3. Put the rest of the sites to L_i^R

and just repeat until no sites remain. This creates a nice tridiagonal Hamiltonian, since any site with coupling to a site in the cell is either in the previous cell or in the next. We can add extra constraints that can be useful. For the patched method we have two extra constraints. We want the sites that couple to the boundary to be in the same cell, and we want all the sites that couple to leads or probes to be in a single cell, preferably the first cell, so as to use the left-right double sweep algorithm, to then calculate the necessary Green's functions. We accomplish this by putting any site that couple to leads or probes in L_0 and nothing else, generating a list of sites that couple to the boundary, L_B, and by extending the algorithms i'th step to be

1. Select any site, m, in L_{i-1}^R where $\mathbf{H}_{mn} \neq 0$ for any site, n, in L_{i-1}
2. Put those sites in L_i
3. If any sites from the L_B is selected add the entire list to L_i.
4. Put the rest of the sites to L_i^R.

This modified algorithm accomplishes the extra constraints we have imposed on our cell division.

2.8 Effective crystal models

Finally we want to discuss two effective crystal models. These effective crystal models are a simple way to treat local potential impurities in a system in an effective

system that itself is periodic. This also lets us find the differences between local interactions that are specific to a certain configuration of disorder and larger scale effectts that are common average effects of many different configurations. In more technical terms we let sites of type i, have an extra en potential of V_i, with a concentration of c_i. The models presented here deal with these types of disorder by replacing the individual local crystal properties with an effective Hamiltonian or Green's function, that can simulate the full system. Each model makes specific approximations, and by comparing the differences between models we can determine the importance of the effects that one model includes and an other excludes.

2.8.1 VCA - Virtual crystal approximation

The simplest way to model potential impurities is by only taking the average effect into account. In this thesis we will in general allow the average be type specific. Essentially we define $\tilde{V}_i = c_i V_i$, which will then be used in the effective Hamiltonian. As an example, graphene will have two site types, one for each sublattice, and we can describe the system within this rough approximation by just 2 variables. Of course the nature of this approximation does not take local effects into account, and where used we will discuss the validity of this approximation.

2.8.2 CPA - Coherent potential approximation

The coherent potential approximation was originally developed to simulate substitutional disorder in alloys in 1967 in Ref. [48]. The approximation allows us to self consistently calculate an effective Green's function which differs from the pristine Green's function, only by some self-energy $\mathbf{\Sigma}_{\text{CPA}}$. The idea is that we can calculate the disorder configuration averaged Green's function in this mean field approach, by doing the single site scattering approximation, i.e. by requiring that the average scattering for each site is 0, as opposed to the total scattering of the full system averaging to 0. Under this approximation the self-energy was shown in Ref. [49] to fulfil the self consistent equation

$$(\mathbf{\Sigma}_{\text{CPA}})_i = \frac{\tilde{V}_i}{\mathbb{1} - (\sum_i V_i(\mathbb{1})_{ii} - \mathbf{\Sigma}_{\text{CPA}})\mathbf{G}_{\text{eff}}} \tag{2.94}$$

where $\mathbf{G}_{\text{eff}}$ is the effective medium Green's function. The Green's function has to found from this self-energy in some fashion, e.g. by exploiting a left-right geomtry system connecting two semi-infinite systems together using the Dyson equation. The Green's function of the semi-infinite system is found by using the effective Hamiltonian

$$\mathbf{H}_{\text{eff}} = \mathbf{H}_0 + \mathbf{\Sigma}_{\text{CPA}}. \tag{2.95}$$

Since the method is self consistent, a good guess for the first self-energy can speed up the convergence process. We used the VCA self energy $\tilde{V}_i$ as the first guess. The approximation used here has already been mentioned, and as further point we want to stress that this can be used straightforwardly to calculate the spectral function allowing us to calculate the DOS, but that the injected spectral density needs extra treament called vertex corrections. As we do not use the approximation for anything but DOS calculations, we have omited this extra treament.

3 The electronic structure of Graphene materials

Since graphene structures plays a leading role in this thesis, we will introduce different standard graphene structures and their electronics, that will be need to understand the rest of the thesis. Many of these results have been published and collected in review articles such as [2].

3.1 Crystal structure

Graphene is a 2 dimensional crystal made up entirely of carbon atoms. Carbon has four valence electrons, 1 in an s-orbital and 3 in the p-orbitals. In graphene two of the p-orbitals hybridises with the s-orbital, making a type of carbon known as sp-2 hybridised carbon. These hybridised orbitals are used to form the σ-bonds in the plane, with the remaining p_z orbital forming the π-bonds, with the orbitals perpendicular to the plane. This of course means that each carbon atom will have exactly 3 neighbours in plane creating a regular hexagonal structure. This lattice is also called a honeycomb lattice because of the familiar shape. Because the electrons in the σ-bonds are used to strongly bind the atoms in-plane the energy of these will be much lower than the electrons occupying the p_z orbitals. Hence the p_z orbitals will be resposible for the states near the Fermi energy. These states will be the main relevant states to consider when looking at electronic transport.
Because of the hexagonal structure the minimal unit cell contains two atoms, both carbon atoms, giving diamond shaped unit cell with two periodicity vectors, $\mathbf{a}_{1,2}$, see figure 3.1. The periodicty vectors can be described as

$$\mathbf{a}_1 = \frac{a_{cc}}{2}\begin{pmatrix} 3 \\ \sqrt{3} \end{pmatrix} \quad \text{and} \quad \mathbf{a}_2 = \frac{a_{cc}}{2}\begin{pmatrix} 3 \\ -\sqrt{3} \end{pmatrix}, \tag{3.1}$$

with a_{cc} being the inter atomic distance between 2 nearest neighbouring carbon atoms, which is around 1.42Å (see eg. Ref. [2]). The reciprocal lattice vectors $\mathbf{b}_{1,2}$,

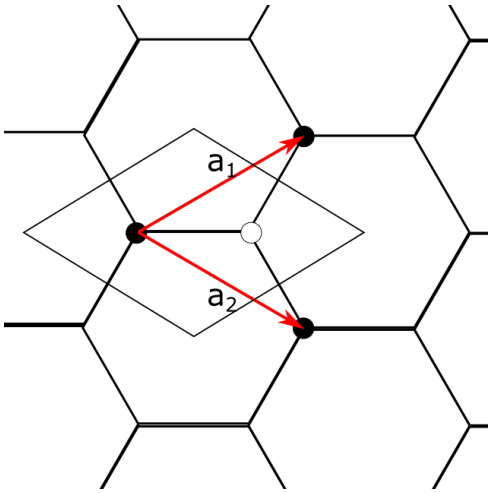

FIGURE 3.1: Lattice structure of graphene

with $\mathbf{b}_{1,2} \cdot \mathbf{a}_{1,2} = 2\pi$ will then be

$$\mathbf{b}_1 = \frac{2\pi}{3a_{cc}} \begin{pmatrix} 1 \\ \sqrt{3} \end{pmatrix} \quad \text{and} \quad \mathbf{b}_2 = \frac{2\pi}{3a_{cc}} \begin{pmatrix} 1 \\ -\sqrt{3} \end{pmatrix}, \tag{3.2}$$

This gives rise to two triangular sublattices, one for each atom in the unit cell. The sublattices are of course equivalent since the atoms are identical, but the main focus of this thesis is the manipulation of this symmetry.

3.2 Electronic structure

If we include only the bands created by the p_z orbitals. The nearest neighbour tight binding Hamiltonian becomes,

$$\mathbf{H}_{TB}(k_1, k_2) = \begin{bmatrix} 0 & -tf(k_1, k_2) \\ -tf^*(k_1, k_2) & 0 \end{bmatrix} \tag{3.3}$$

with $k_{1,2} = \mathbf{k} \cdot \mathbf{a}_{1,2}$ and

$$f(k_1, k_2) = 1 + e^{ik_1} + e^{ik_2}, \tag{3.4}$$

and where $t \approx 2.8$ eV, is there nearest neighbour hopping (see Ref. [2]). We can solve the time independent Schrödinger equation to find the band structure. The eigenvalue equation becomes

$$0 = \det(E\mathbb{1} - \mathbf{H}_{TB}(k_1, k_2)) \tag{3.5}$$

$$= E^2 - t^2|f(k_1, k_2)|^2 \Leftrightarrow \tag{3.6}$$

$$E = \eta t|f(k_1, k_2)|, \tag{3.7}$$

with $\eta = \pm 1$, which we can call the band index (-1 is the valence band and $+1$ is the conduction band). By tranforming $\mathbf{k}$ to the more standard (k_x, k_y) basis, we can get the familiar first brillioun zone bandstructure as seen in figure 3.2. We see that first brillioun zone has exactly 2 points where the valance and conduction bands touch, called the Dirac points. By symmetry we have two sets of 3 equivalent points. These sets are called the K and K' points and they are degenerate as long as the inversion

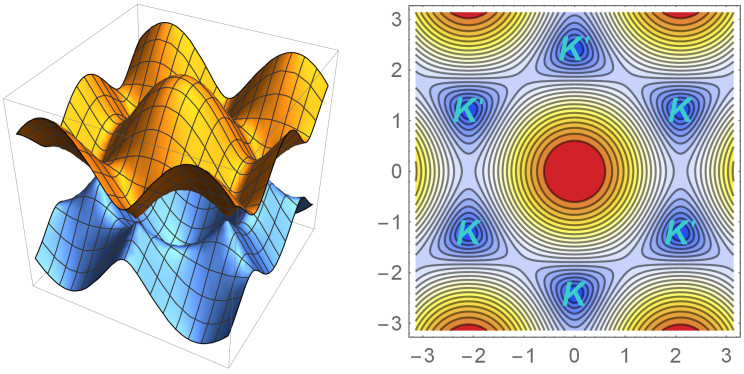

FIGURE 3.2: **Left**: Full tight binding bands. **Right**: Contour plot of the valence (or conduction) band

symmetry of the unit cell is kept, and near these points the Dirac approximation can be used as discussed in section 3.3.

We can also calculate the eigenstates in graphene on the two sublattices to be

$$\psi = \begin{pmatrix} \psi_A \\ \psi_B \end{pmatrix} = \frac{1}{\sqrt{2}} \begin{pmatrix} 1 \\ \eta f(k_1, k_2)/|f(k_1, k_2)| \end{pmatrix} \tag{3.8}$$

inside a single unit cell. The phase change over multiple unit cells can be included using Bloch's theorem as $e^{i\mathbf{r}\cdot\mathbf{k}}$, where $\mathbf{r}$ is the seperation between the unit cells. With a seperation of $\mathbf{r} = m\mathbf{a}_1 + n\mathbf{a}_2$ we get the wave function

$$\begin{pmatrix} \psi_A \\ \psi_B \end{pmatrix}(m, n) = e^{imk_1} e^{ink_2} \frac{1}{\sqrt{2}} \begin{pmatrix} 1 \\ \eta f(k_1, k_2)/|f(k_1, k_2)| \end{pmatrix} \tag{3.9}$$

3.3 Graphene in the Dirac approximation

Another of the most useful descriptions of graphene is the Dirac approximation around the two Dirac points, K and K' which works well for low energies and in the continuum limit, where the individual atoms play a small role compared to collective effects (see e.g. [2]), and where the dispersion becomes approximately linear. If we introduce the valley index $\tau = 1$ ($\tau = -1$) for the K (K') valley, the general Hamiltonian becomes

$$\mathbf{H}_\tau = -i\hbar v_F \boldsymbol{\sigma}_\tau \cdot \boldsymbol{\nabla} + \mathbf{V}(\mathbf{r}) \tag{3.10}$$

with v_F being the Fermi velocity in graphene, and $\boldsymbol{\sigma}_\tau = (\tau\sigma_x, \sigma_y)$ with $\sigma_{x,y}$ being the standard Pauli matrices. The Dirac approximation models the electron as massless or relativistic fermions[1], and it is an ideal way of looking at larger uniform structures such as circular potentials and holes, which havve fully closed analytical solutions. It works especially well if the inversion symmetry of graphene is conserved, keeping the two valleys equivalent. If the inversion symmetry is not kept it is important to notice that the Dirac model explicitly excludes any intervalley scattering. The large advantage of the Dirac model is that the complexity does not increase with feature size, allowing us to treat structure with very large sizes as long as the features are simple enough.

[1] A mass can be introduced through the potential V

3.3.1 Calculating current and electronic density

In general the electronic density, n, is straightforward to find given the wavefunction, as just:

$$n = \psi^\dagger \psi \tag{3.11}$$

Furthermore we can track the flow of probability by using a standard continuity equation

$$\frac{\partial}{\partial t} n + \boldsymbol{\nabla} \cdot \mathbf{j} = 0, \tag{3.12}$$

where $\mathbf{j}$ is the probability density current. By using the Schrödinger equation

$$i\hbar \frac{\partial \psi}{\partial t} = \mathbf{H}_\tau \psi \tag{3.13}$$

we get:

$$\begin{aligned}
\frac{\partial}{\partial t} n &= \frac{\partial \psi^\dagger}{\partial t}\psi + \psi^\dagger \frac{\partial \psi}{\partial t} && (3.14)\\
&= \frac{1}{i\hbar}\left(- \left(\mathbf{H}_\tau \psi\right)^\dagger \psi + \psi^\dagger \mathbf{H}_\tau \psi \right) && (3.15)\\
&= -2 v_F \mathrm{Re}\left[\left(\boldsymbol{\sigma}_\tau \cdot \boldsymbol{\nabla}\psi\right)^\dagger \psi \right] && (3.16)\\
&= -2 v_F \boldsymbol{\nabla} \cdot \mathrm{Re}\left[\psi^\dagger \boldsymbol{\sigma}_\tau \psi \right] && (3.17)\\
&= -2 v_F \boldsymbol{\nabla} \cdot \left[\psi^\dagger \boldsymbol{\sigma}_\tau \psi \right] && (3.18)\\
&= -\boldsymbol{\nabla} \cdot \mathbf{j} && (3.19)
\end{aligned}$$

and thus the probability current becomes

$$\mathbf{j} = 2 v_F \psi^\dagger \boldsymbol{\sigma}_\tau \psi \tag{3.20}$$

3.4 Graphene Green's function

By direct inversion of the Hamiltonian we find

$$\mathbf{G}_{ij}(z, k_1, k_2) = \frac{N_{ij}(z, k_1, k_2)}{z^2 - t^2 |f(k_1, k_2)|^2} \tag{3.21}$$

with

$$N_{ij}(z, k_1, k_2) = \begin{cases} z & \text{for i and j on same sublattice} \\ t f(k_1, k_2) & \text{for i on sublattice a and j on sublattice b} \\ t f^*(k_1, k_2) & \text{for i on sublattice b and j on sublattice a} \end{cases} \tag{3.22}$$

By doing the inverse fourier transform we find to real space Green's function elements for two elements, i and j, in unit cells with positions $\mathbf{r}_i$ and $\mathbf{r}_j$ respectively, to be

$$\mathbf{G}_{ij}(z) = \frac{1}{\Omega_{BZ}} \int \mathrm{d}^2\mathbf{k} \frac{N_{ij}(z, \mathbf{k}) e^{i\mathbf{k}\cdot(\mathbf{r}_j - \mathbf{r}_i)}}{z^2 - t^2 |f(\mathbf{k})|^2} \tag{3.23}$$

where Ω_{BZ} is the volume of the first Brillouin zone. We want to find an analytical approach to try and cut down the number of numerical integrations needed. This

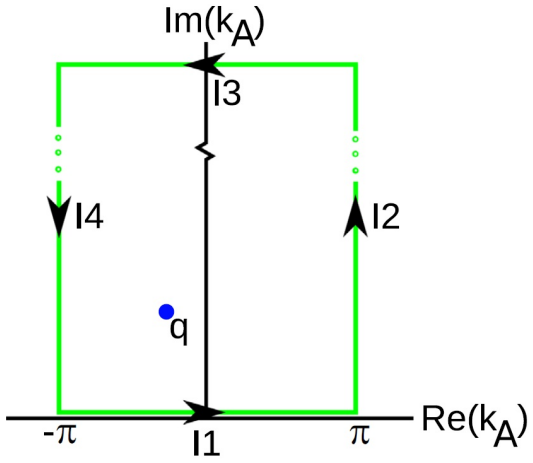

FIGURE 3.3: Integration path. Image taken from Ref. [50]

has been done by Ref. [50], and we do something similar in the 1NN TB model. By transforming to a $\mathbf{k}$ basis consisting of reciprocals of the armchair and zigzag lattice vectors, $\mathbf{b}_{ac}$ and $\mathbf{b}_{zz}$, given as

$$\mathbf{b}_{ac} = \mathbf{b}_1 + \mathbf{b}_2 \quad \text{and} \quad \mathbf{b}_{zz} = \mathbf{b}_1 - \mathbf{b}_2 \tag{3.24}$$

we get

$$\mathbf{G}_{ij}(z) = \frac{1}{2\pi^2}\int_{-\pi}^{\pi} \mathrm{d}k_{ac} \int_{-\frac{\pi}{2}}^{\frac{\pi}{2}} \mathrm{d}k_{zz} N_{ij}(z, k_{ac}, k_{zz}) \frac{\mathrm{e}^{\mathrm{i}k_{ac}(m+n)+\mathrm{i}k_{zz}(m-n)}}{z^2 - t^2[1 + 4\cos^2(k_{zz}) + 4\cos(k_{zz})\cos(k_{ac})]}, \tag{3.25}$$

where $\mathbf{r}_j - \mathbf{r}_i) = m\mathbf{a}_1 + n\mathbf{b}_2$ and $m, n \in \mathcal{Z}$. The advantage of this basis is that we can solve one of the two integrals using complex contour integration techniques. Either of the two can be choosen to be integrated, leaving the remaining to be solved using numerical techniques. We will focus on the solution of the armchair integral here, but the zigzag integral is solved in a similar manner. We extend the variable k_{ac} to the complex plane where the integrant is an analytic function except for removable singularities. This allows us to use the residue theorem when evaluating contour integrals in the complex plane. The integral we want to evaluate is a rectangular contour consisting of 4 lines

$$C_1 : -\pi \to \pi \tag{3.26}$$
$$C_2 : \pi \to \pi + \mathrm{i}L \tag{3.27}$$
$$C_3 : \pi + \mathrm{i}L \to -\pi + \mathrm{i}L \tag{3.28}$$
$$C_4 : -\pi + \mathrm{i}L \to -\pi \tag{3.29}$$

where we let $L \to \infty$, which has corresponding integrals I_1, I_2, I_3, I_4, see figure 3.3. The integral of the contour is the sum of the integral of the four contours $I_C = I_1 + I_2 + I_3 + I_4$. Since the Green's function is periodic as a funtion of k_{ac} with a period of 2π, $I_2 = -I_4$. Furthermore $I_3 \to 0$ as $L \to \infty$, leaving $I_C = I_1$. We can find the pole, q, of the Green's function inside the contour, condsidering it as a function k_{ac}, as

$$q = \pm\cos^{-1}\left(\frac{\frac{z^2}{t^2} - 1 - 4\cos^2(k_{zz})}{4\cos(k_{zz})}\right), \tag{3.30}$$

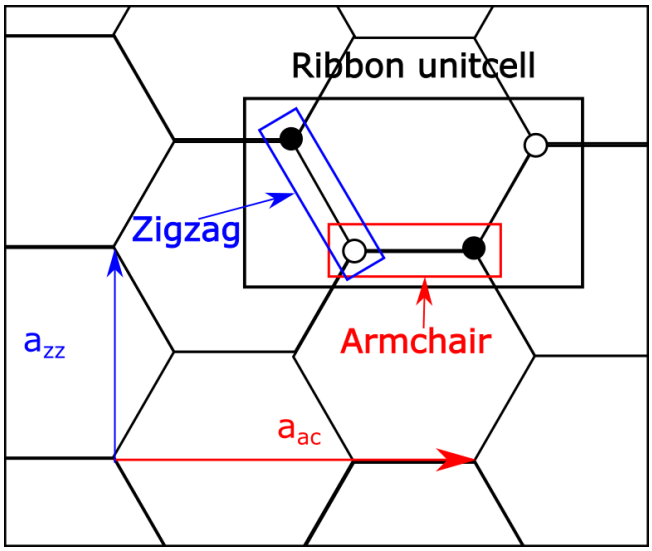

FIGURE 3.4: Armchair and zigzag unit vector and the ribbon unit cell

where $\mathrm{Im}(q) > 0$. Using the residue theorem we find

$$\mathbf{G}_{ij}(z) = \frac{i}{4\pi t^2} \int_{-\frac{\pi}{2}}^{\frac{\pi}{2}} \mathrm{d}k_{zz} \frac{N_{ij}(z, q, k_{zz}) e^{iq(m+n)+ik_{zz}(m-n)}}{\cos(k_{zz}) \sin(q)}. \tag{3.31}$$

This result will play a main role in getting faster and more accurate results for the pristine graphene Green's function, since we have reduced the amount of Fourier transforms needed.

3.5 Graphene nanoribbons

By "cutting" graphene along some direction we get structures known as graphene nanoribbons or GNRs. In principle any multiplum lattice vectors can be used, however we will focus on the armchair and zigzag edged ribbons, also called AGNRs and ZGNRs respectively. We use the reciprocal vectors defined equations 3.24, and find the corresponding real space lattice vectors

$$\mathbf{a}_{ac} = \mathbf{a}_1 + \mathbf{a}_2 \quad \text{and} \quad \mathbf{a}_{zz} = \mathbf{a}_1 - \mathbf{a}_2. \tag{3.32}$$

The AGNRs and ZGNRs can be constructed using the ribbon unit cell shown in figure 3.4. We will in general have a "width" direction and a "length" direction. For the AGNRs the width direction along the $\mathbf{a}_{zz}$ direction and the length along parallel with $\mathbf{a}_{ac}$, whereas the converse is true for the ZGNRs. We will denote a ribbon by the number of standard unit cells across the width of the ribbon, where the ribbon unit cell actually consists of 2 standard unit cells. E.g. 100 of the ribbon unit cells connected along $\mathbf{a}_{zz}$ direction into what we can call the unit chain for the 200-AGNR. In order for it be denoted as a nanoribbon we will then reqire this unit chain to be repeated a large number of times, i.e. the device has to be much longer than it is wide. The ribbon unit cell can be used to get even widths, where odd widths need "extra" "half" ribbon unit cells where the individual types are indicated in the figure.

We notice that the atoms of the ribbon unit cell furthest apart in the armchair direction, sit on opposite sublattices. As a consequence ZGNRs will be sublattice

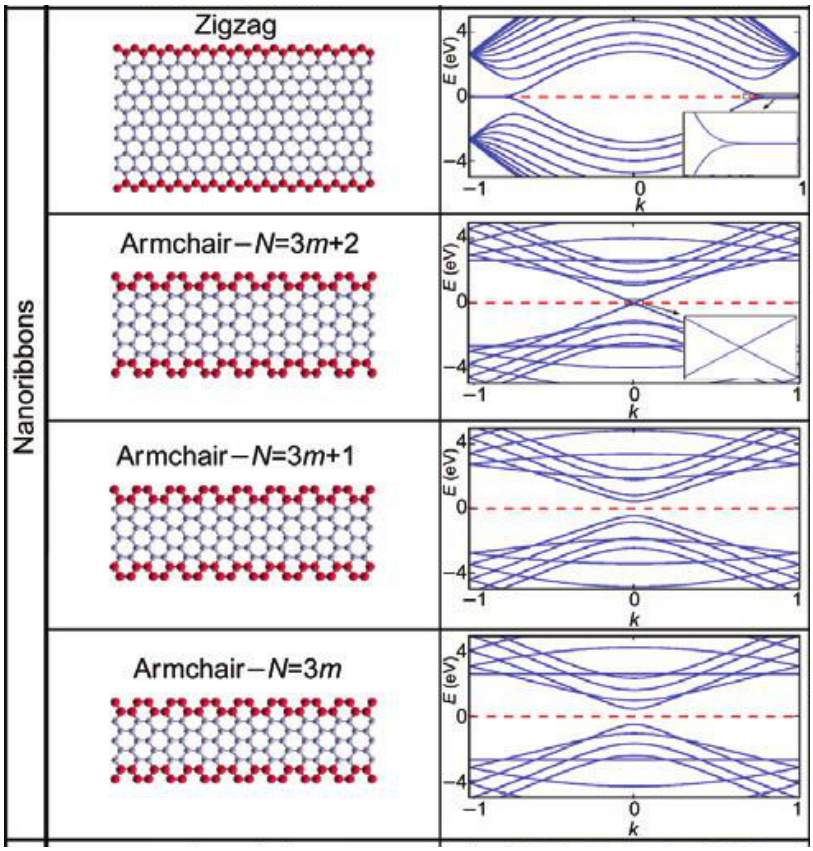

FIGURE 3.5: Electronic bands of nanoribbons from [51]

asymmetric, with one edge consisting exclusively of atoms on a single sublattice and the atoms on the other edge the opposite sublattice.

We can calculate the electronic bands for the nanoribbons by constricting transverse part of the wave function. We can rewrite the wave function in terms of k_{ac} and k_{zz}, as

$$\begin{pmatrix}\psi_A\\ \psi_B\end{pmatrix}(m,n) = \mathrm{e}^{\mathrm{i}(m+n)k_{ac}}\mathrm{e}^{\mathrm{i}(m-n)k_{zz}}\frac{1}{\sqrt{2}}\begin{pmatrix}1\\ \eta f(k_{ac},k_{zz})/|f(k_{ac},k_{zz})|\end{pmatrix}. \tag{3.33}$$

Adding the solutions with k_{zz} and $-k_{zz}$, we get a sine wave in the zigzag direction

$$\psi_{ac}(m,n) = \sin\left(k_{zz}\frac{n-m}{2}\right)\mathrm{e}^{\mathrm{i}(m+n)k_{ac}/2}\frac{1}{\sqrt{2}}\begin{pmatrix}1\\ \eta f(k_{ac},k_{zz})/|f(k_{ac},k_{zz})|\end{pmatrix}. \tag{3.34}$$

For the armchair ribbon we need the wave function to be 0 on both edges, giving the condition that $k_{zz}\frac{n-m}{2} = j\pi$, where $j = 1,2,3,...$, and $n-m-1 = W_{ac}$ is the width of the armchair ribbon. A similar condition can be made for the zigzag edged ribbons. The band structure of the nanoribbons are plotted in figure 3.5 from Ref. [51].

It is worth noting that in the standard $1NN$ tight binding model every third armchair is metallic, but the others are semi conducting, whereas all of the zigzag edged ribbons are metallic.

4 Sublattice engineering

While graphene has remarkable electronic properties such as high Fermi velocity and linear dispersion, it lacks some of the properties that are required for traditional electronics. The high symmetry of the unit cell causes the valance and conduction band to meet in a zero dimensional surface containing a finite number of points. THi makes graphene what is called a semi-metal or zero bandgap semiconductor as there is no denisty of states at the fermi energy. Traditional electronics are built on silicon based semiconductors because of the ability to turn transistors on and off. We usually talk about an on-off ratio, where the size of the band gap will correlate to this on-off ratio. Hence an entire research field, called band gap engineering, opened up in order to make graphene suitable for electronics. The goal is to give graphene a stable band gap large enough to be used for electronics, and still keep as many of the remarkable electronic properties of graphene as possible. In this chapter we go over the simple model we use for perturbing the sublattice symmetry, as well as some results produced in cooperation with ph.d. student Thomas Lane from the National Graphene Institute at the University of Manchester in the U.K.

4.1 Simple Model

A straightforward way to introduce a band gap in graphene is to break the sublattice- or inversion symmetry of the unit cell. By introducing a different potential on the sublattice, we find that the Hamiltonian becomes

$$\mathbf{H}_{TB}(k_1,k_2) = \begin{bmatrix} V_A & -tf(k_1,k_2) \\ -tf^*(k_1,k_2) & V_B \end{bmatrix}, \tag{4.1}$$

and the corresponding electronic bands

$$\begin{aligned} 0 &= \det(E\mathbb{1} - \mathbf{H}_{TB}(k_1,k_2)) && (4.2)\\ &= (E-V_A)(E-V_B) - t^2|f(k_1,k_2)|^2 && (4.3)\\ E &= \frac{1}{2}(V_A+V_B) \pm \frac{1}{2}\sqrt{(V_A-V_B)^2 + 4t^2|f(k_1,k_2)|^2} && (4.4) \end{aligned}$$

By introducing the average shift $V_0 = \frac{1}{2}(V_A + V_B)$ and the mass term $\Delta = \frac{1}{2}(V_A - V_B)$, we can rewrite the dispersion as

$$E(k_1, k_2) = V_0 \pm \sqrt{\Delta^2 + t^2|f(k_1, k_2)|^2} \tag{4.5}$$

and we see that we open up a band gap of the size $2|\Delta|$. The general type of sublattice manipulation we do will be introducing a mass term (and possibly an average shift), in ways that simulate experimental possibilities.

4.1.1 Topology of the model

Breaking a symmetry can give rise to topological states and topological electronic gaps. However breaking the inversion symmetry of the unit cell in graphene gives rise to what is known as a trivial or Semenoff insulator [52]. Introducing a standard Dirac mass introduces similar Berry phases for each valley but with opposite signs, giving a total chern number of zero [28]. However at interfaces where the mass term changes we can have midgap interface states that are valley polarised called Jackiw-Rebbi modes [53, 54].

4.2 Experiments and other theoretical work

Several different approaches to modify the sublattices differently has been experimentally shown to exist. In Refs. [14, 16, 55, 56] it has been shown that large spontaneous domains where substitutional nitrogen dopants occupy mainly a single sublattice in CVD graphene. These type of impurities will on average provide potentials similar to the simple model introduced above, however the random nature of the dopant position will introduce an element of disorder that has to be taken into account, and will give rise to an extra pertubation on top of the simple model. Theoretical studies has been done on why these asymmetric distributions appear and suggest possible mechanisms such as preferential position relative to edges [57], or impurity interactions [58, 59]. Furthermore theoretical studies have predicted that such impurity distributions give rise both a transport gap as well as an electronic band gap and an electron-hole asymmetric conductivity (see Refs. [18, 60–63]). Other strategies include placing the graphene on top of hexagonal boron nitride [33, 64], which has a similar structure and a similar lattice constant to graphene, but with two different atoms in the unit cell. This gives rise to an added potential with a mass term, and the slight mismatch of the lattices gives rise to a Moiré pattern, which means that the mass term will vary over the graphene sheet. This has been used in litterature as a route towards achieving a valley Hall effect in graphene.

4.3 Interfaces

We will discuss the interfaces or domain walls in this type of Dirac mass gapped graphene where domain refer to regions where with simalar mass term but where the sign of the mass term changes. The domains we will discuss here will swap the sublattice potentials changing the sign of the Dirac mass term, $\Delta \to -\Delta$. There exists three general types of uniform interfaces in graphene, namely zigzag, armchair and chiral types that mixes armchair and zigzag types. Of these types of domain walls the zigzag and armchair has been investigated in graphene in 2008 in Ref. [29], using the Dirac model and the 1NN tight binding model. The two different interface

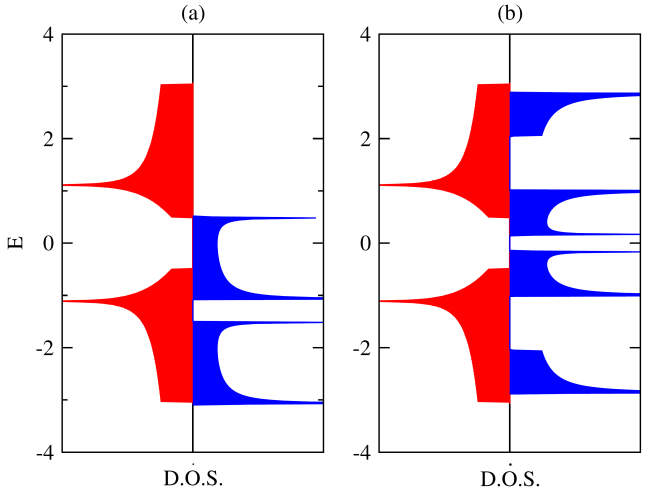

FIGURE 4.1: Density of states (D.O.S. in arbitrary units, blue or dark gray) versus energy E (in units of t) for (a) a zigzag domain wall and (b) an armchair wall when $\Delta = 0.5t$. Also shown is the D.O.S. for bulk bands (red or light gray). Figure taken from [29]

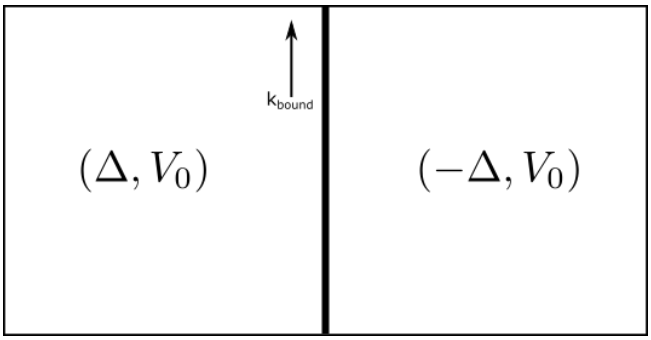

FIGURE 4.2: Interface setup schematic

types have very different boundary states. This is primarily a result of the build-in asymmetry that causes all atomic sites in zigzag boundary to have the same on site potential. In figure 4.1 we see the formation of midgap bands bridging the gap in the zigzag boundary case, but with a small gap in the armchair boundary.

4.4 Spectral function near interfaces

In our project we also look at these boundaries in the 1NN tight binding model. The setup is as follows, two semi-infinite leads with the asymptotic behavior of each domain meeting in a transitional region with periodicity in the transverse direction as shown in the schematic in figure 4.2. We apply a sublattice dependent potential where the mass term smoothely changes sign over the boundary. We extract the spectral function as a function of energy and wavenumber along the boundary for atoms close to the boundary to simulate ARPES (Angle Resolved Photo Emssion Spectroscopy) type experiments, the results of which are shown in figure 4.3.

For the zigzag boundary we see the formation of single velocity bands split between the two valleys, similar to the predictions made by the Dirac description [29], meaning that the current carried by these linear bands along the interface will be valley polarised. For the armchair interface configuration the valleys are degenerate

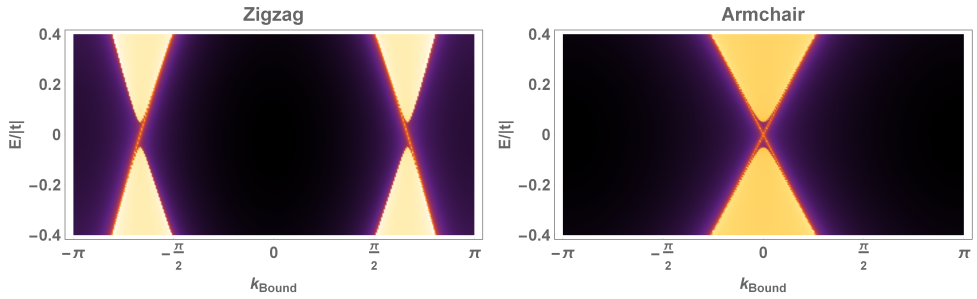

FIGURE 4.3: Logarithm of spectral function for a zigzag domain wall (right) and an armchair domain wall (left), both with $\Delta = 0.05|t|$ and $V_0 = 0$

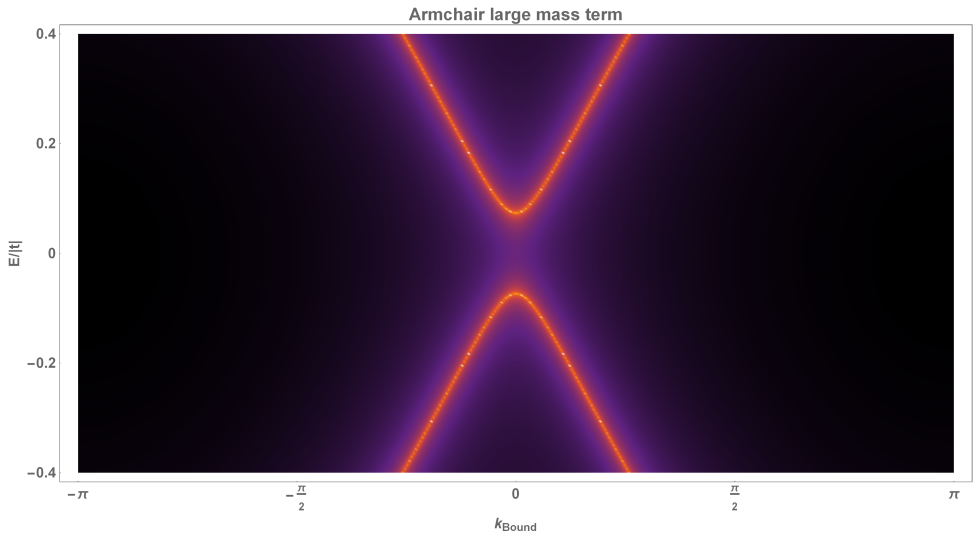

FIGURE 4.4: Logarithm of spectral function for a armchair domain wall with $\Delta = 0.5|t|$ and $V_0 = 0$, with step function potential

in the transverse k, so we cannot directly identify the valley behaviour, however we still see the formation of the linear bands. The non-linear bands in the background are the bulk states described by the fully periodic Hamiltonian described in the previous section 4.1, projected from 2D onto the periodic direction. This feature allows us easily distinguish the 1D-like states, from the 2D-like bulk states. We notice that 1d bands for the armchair does not have a noticable gap. In general this gap shrinks as the potential is smoothened over the interface from the large gap seen in figure 4.1, and of course the smaller mass term used also shrinks the gap but in the case of a sudden interface the gap will still have a noticable size. This gap closening is very relevant in the cases where the gap is induced by *disorder* e.g. by an asymmetric doping distribution as seen in Ref. [14], where a natural smoothening of the interface will occur. In figure 4.4 we rediscover the gap for the 1-D bands by increasing the mass term to the same as in figure 4.1.

It is worth noting that the projections of K and K' points onto the periodic directions are different in the case of an armchair boundary compared to that of a zigzag. In the zigzag case the valleys are projected onto different places in k-space keeping the different valleys separated, whereas in the armchair case they are projected on top of each other. Hence the opening of a gap in teh armchair case could possibly be explained as avoided crossing of the two linear bands.

5 Asymmetrically doped nanoribbons

Asymmetric doping in nanoribbons is an interesting subject to study. First, the finite size of the ribbon lets us calculate the average effect of doping without having to introduce periodicity, and still have resonable computational time. We can treat doping as the random events that they are. Second, we can also calculate the interaction between sublattice-asymmetry caused by the random doping and the symmetries of graphene edges. Apart from the obvious implication for doping of nanoribbons, extended edge-like defects appear in several places in the form of grain boundaries when growing graphene via CVD. It is well known that the electronic structure and transport in nanoribbons are highly dependent on the edge geometry as seen in section 3.5, and similarly it has also been shown in Refs. [11, 13, 65–76] that the impurity distribution has a profound influence.

The asymmetric doping is further motivated by experiments that show spontaneous sublattice-asymmetric nitrogen distributions [10, 14, 55, 56], and theoretical work that show the appearance of stable transport- and band gaps [18, 60–63] as discussed in the section 4.2.

In this chapter, which is based on the work published in Paper I, we consider both of the high symmetry ribbons, the armchair egded (AGNR) and the zigzag edged (ZGNR). The AGNRs behaves mostly bulk-like, with reliable band- and transport gaps, whereas the in-built sublattice-asymmetry of the ZGNRs causes them to behave in a different manner. The electronic band gap gives way to pronounced edge states, along a single one of the ZGNR edges, and the transport is only suppressed, as opposed to completely quenched, in the expected gapped region. We investigate using a randomized disorder configuration average, where several independent random distributions are chosen and the resulting DOS and transmission are averaged. For local properties such as the LDOS, we choose a random single configuration. We also use two effective models, namely the VCA and CPA models discussed in sections 2.8.1 and 2.8.2 respectively, and compare to the DOS obtained using the numerical averages of the tight binding model, and we show that the CPA captures the behaviour of the averaged DOS. Finally we also look at sublattice domain interfaces in nanoribbons and their interaction with edges, and show that robust edge states similar appear to the bulk cases, even in the presence of disorder, which should be detectable by experimental techniques such as scanning tunneling microscopy.

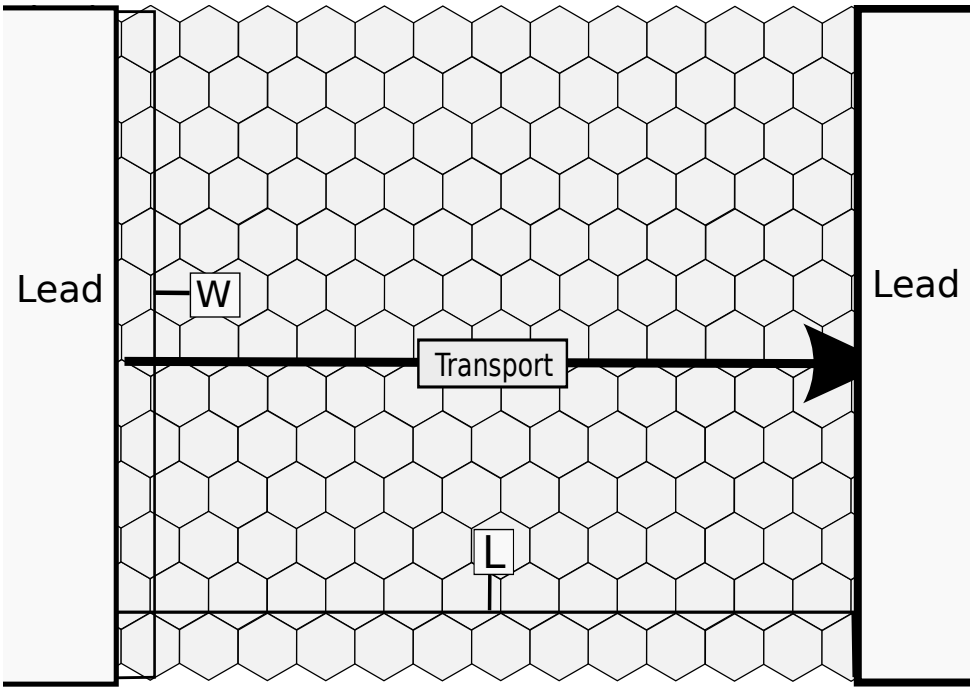

FIGURE 5.1: Schematic of the ribbon setup, showing a zigzag ribbon of width W and length L.

5.1 Modelling nitrogen dopants

In order to model substitutional nitrogen dopant we use the 1NN tight binding model discussed in sec 3.2. We use a simple dopant model where the nitrogen atom substition at site i, is represented by an on-site potential shift $V_i = -|t|$. More accurate parametrisations of nitrogen can be found in e.g. Refs. [15, 18, 77], but the qualitative behaviour is reasonably independent on this exact parametrisation so we use a more generic model, so we can identify the source of the physical features. As discussed in sec 4.1 the average potential gives rise to a band gap and a potential shift, $2|\Delta|$ and V_0 respectively, where $V_0 = \frac{1}{2}(V_A + V_B)$ and the mass term $\Delta = \frac{1}{2}(V_A - V_B)$, and $V_{A,B}$ are the average potentials on the a and b sites.

All electronic and transport quantities are calculated using Green's functions techniques as described in section 2.3, and we construct a device region Green's functions recursively, with the double sweep algorithm described in section 2.7.1, with the priciple layers being the minimal nanoribbon slices. We have also included semi infinite pristine graphene nanoribbon leads, the self-energy for which is constructed using the efficient decimation algorithm from section 2.7.2. A schematic is shown in figure 5.1

Finally we use the two effective models, the VCA and CPA, to describe an effective medium to analyse the averaged DOS. The VCA substitutes the finite disordered nanoribbon with an perfectly periodic infinitely long nanoribbon of the same width, where the on-site potentials are exactly the average expected shift $\tilde{V}_{A,B} = -c_{A,B}|t|$, where $c_{A,B}$ is the concentration of dopants on site A/B. Hence this model only takes the effect of the average potential into account. The CPA replaces the potential used in the VCA with an energy dependent self-energy, which can be found selfconsistently using the single site scattering approximation, as $(\mathbf{\Sigma}_{\text{CPA}})_i = \frac{\tilde{V}_i}{\mathbb{1} - (V_i - (\mathbf{\Sigma}_{\text{CPA}})_i)\mathbf{G}_{\text{eff}}}$, with $i = A, B$. Since we use the single site scattering approximation, the CPA neglects any higher-order cluster effects such as localisation.

5.2 Averaged Transmission and DOS

We start out by focusing on the difference between symmetric- (completely random) and asymmetric (confined to a single sublattice) distributions, using a 101-AGNR and 100-ZGNR. The pristine 101-AGNR has a width $\sim$ 12 nm, and is metallic (since 101 is divisible by 3), and similarly the 100-ZGNR is also metallic but with width $\sim$ 21 nm. First we focus on the transmission plotted in figure 5.2 (A,B), in a comparison between the pristine system (shaded grey background), the symmetric distribution (blue dashed line) and the asymmetric distribution (red line). The transmission is calculated using the averages of 100 different randomly generated configurations of disorder with nanoribbons consisting of 40 unit chains of length ($\sim$ 17 nm for AGNR and $\sim$ 10 for ZNGR), whereas the DOS is calculated using the central 800 unit chains of a system with a total length of 1000 unit chains. In both cases with impurity concentrations of $c_A = c_B = 0.05$ for the symmteric and $c_A = 0.1$, $c_B = 0.0$ for the asymmetric case, which results in the same total amount of dopants.

For AGNRs the asymmetric disorder opens up a transport gap with sharp edges on the hole side of the energy spectrum, whereas the symmetric distribution only suppresses the transmission slightly for the same energies mostly keeping the T= 1 plateau reported in Ref. [68]. Also a corresponding electronic band gap opens in the average DOS for asymmetric case, which is consistent with the results presented for asymmetric disorder in bulk graphene sheets in [18]. We notice that the VCA captures most of the qualitative behaviour of the DOS for electron energies, but it slightly over estitemates the size of the bandgap and has poor agreement on the hole side. These differences mostly disappear when using the CPA instead, which has excelent agreement on both sides. This discrepancies between the two models suggest that the electron site sees very little scattering and the effect there is dominated by the average potential introduced with the dopants. For the hole energies the converse is true. The failure of the VCA and the corresponding success of the CPA suggest that scattering plays a more significant role, which is also supported by the fact that the transmission on the hole side is quenched compared to the electronic side, and has the transmission plateaus smoothened out. Furthermore this is in agreement with the similar results reported for graphene sheets [18], where reduced mobility on the hole side is associated with a pseudospin polarisation giving a higher occupation of the undoped (doped) sublattice on the electron (hole) side. We have confirmed this in the AGNR case by looking at the sublattice specific average DOS. By examining different concentrations, we also checked the scaling of the bandgap that is reported to be $E_G \sim c_A^{0.75}$ in graphene sheets [18], and find a similar scaling.

Looking at the other type of nanoribbons, the ZGNR, many of the features discussed for the AGNR change. We first notice the transmission gap is now more a general suppresion of the transmission with no well defined left edge, and more importantly it is no longer accompanied by a corresponding electronic band gap, where we see a large amount of DOS inside the region where we would expect the gap. Since the VCA always introduces a gap, it cannot capture the full behaviour of the DOS, however it still captures the low energy behaviour at the electron side, including the sharp peak at $E = 0$, fairly well. This peak is associated with states localised on the edge atoms of a ZGNR. It is doubly-degenerate in pristine ribbons, as the states on each ribbon edge, although belonging to opposite sublattices, are equivalent. Adding a uniform mass term breaks this degeneracy and the peak splits into two which reside at the bandgap edges, at energies corresponding to the onsites of each sublattice, as shown by the VCA curve. Again it is the hole side that presents

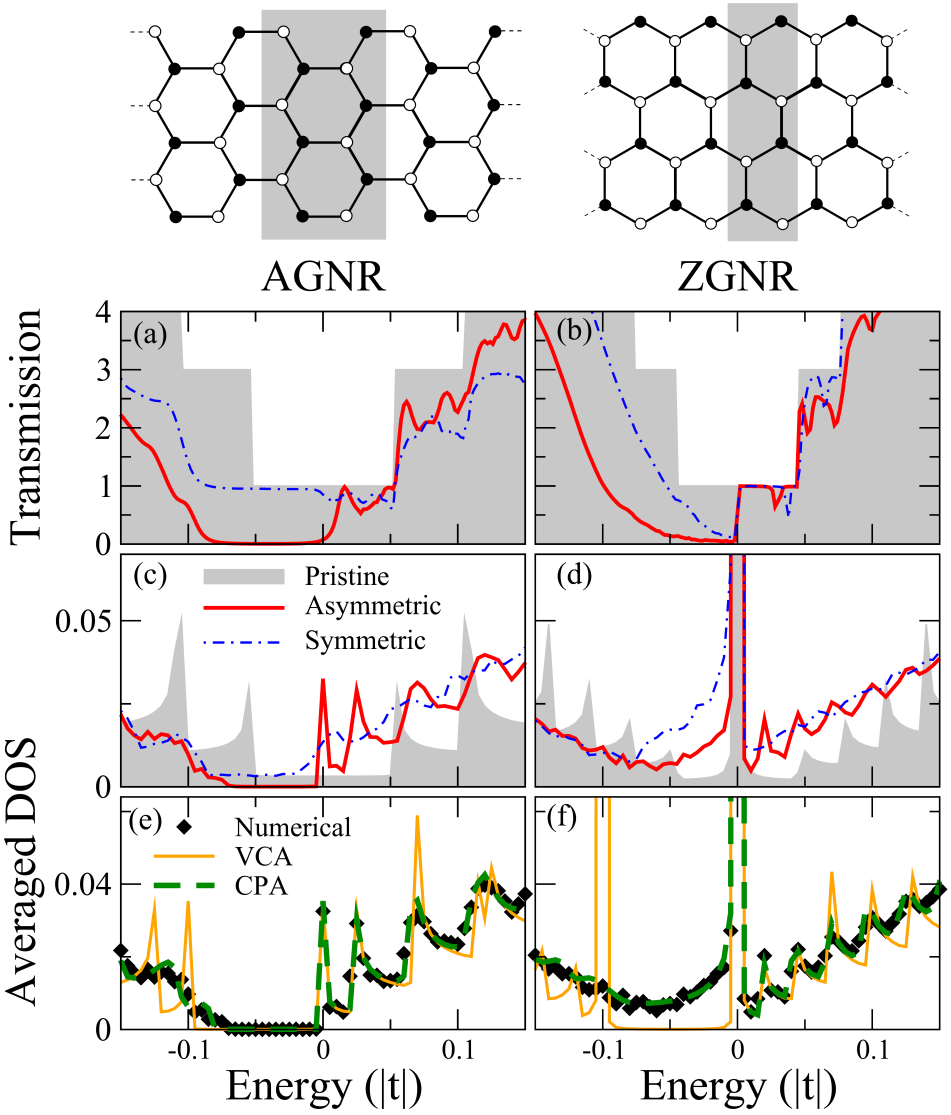

FIGURE 5.2: (Top) Schematics of a 6-AGNR and 4-ZGNR, with the unit cells shown by the shaded areas and the A (B) sublattice sites by hollow (filled) symbols. The index counts the dimer lines or zigzag chains across the ribbon. Remaining panels show results for a 101-AGNR (left) and a 100-ZGNR (right). a), b) show the (averaged) transmission through pristine systems (grey shading) and also systems with 40 unit cells of sublattice-asymmetric (solid red lines) and sublattice symmetric disorder (blue dashed-dotted line). c), d) show the numerically averaged DOS of longer systems with corresponding disorder profiles. e), f) show the numerically averaged DOS for the fully asymmetric case (black symbols) compared to VCA (orange) and CPA (green, dashed) model calculations. The concentration of N atoms for all disordered cases is 5%. (Figure from Paper I).

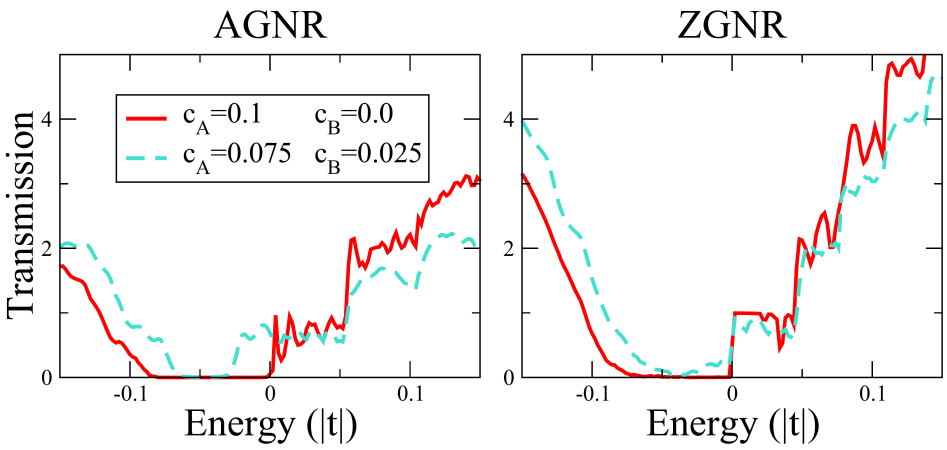

FIGURE 5.3: Transmissions for 101-AGNR (left) and 100-ZGNR systems with 80 unit cells of asymmetric disorder. Results are shown for both fully (red, solid) and partially (turquoise, dashed) asymmetric distributions of impurities. (Figure from Paper I)

difficulties for the VCA, but again CPA restores all effects seen in the tight binding calculations. This suggests that the DOS appearing in place of the expected gap is due to scattering effects dominating over the effect of the average potential.

In order to verify the robustness of the transmission shapes, and especially the gap opening under less asymmetric distributions, we compare the $c_A = 0.1$, $c_B = 0.0$, distribution to a $c_A = 0.075$, $c_B = 0.025$ distribution. This comparison is shown in figure 5.3. We clearly see that the general shape is conserved in both the AGNR and ZGNR case, and both case we get a middle ground between between the symmetric and asymmetric case. Most interestingly the AGNR gap shrinks in width instead of in depth, preserving the clear band gap feature, with the gap slightly smaller and with center preserved moving the right gap edge away from $E = 0$. This gives promise for experimental implementation as samples with asymmetry higher than 90% have been reported in Ref. [14].

5.3 Local DOS

In an effort to further analyse the differences between the ZGNR and the AGNR, we explore the LDOS in the middle of the expected gap energy regime for a single disorder configuration. In figure 5.4 we show these LDOS maps. For the AGNR we see that the LDOS quickly decays away from the leads, uniformly across the ribbon. For the ZGNR we similarly see that the LDOS decays away from the leads, but unlike the AGNR case the LDOS is not uniform across ribbon. We see large clusters of LDOS along the bottom edge, for which the outer most atoms belong to the doped sublattice. This suggests an interplay between the doping of a particular sublattice and the proximity of a zigzag edge of the same sublattice. Since the accuracy of the CPA in terms of the averaged DOS suggest that this can be explained in term of single scattering events, we examine single individual dopant near a zigzag edge.

We chose to use a short 50-ZGNR ribbon to locally study the effect of a single N dopant near the zigzag edge. In Figure 5.5 (a) we show some possible inequivalent positions near said edge with color coded circles. The red and green are on the same sublattice as the edge atom, whereas the blue is on the other sublattice. In Figures 5.5 (b) and 5.5 (c) we see the effect on tranmission and average DOS for

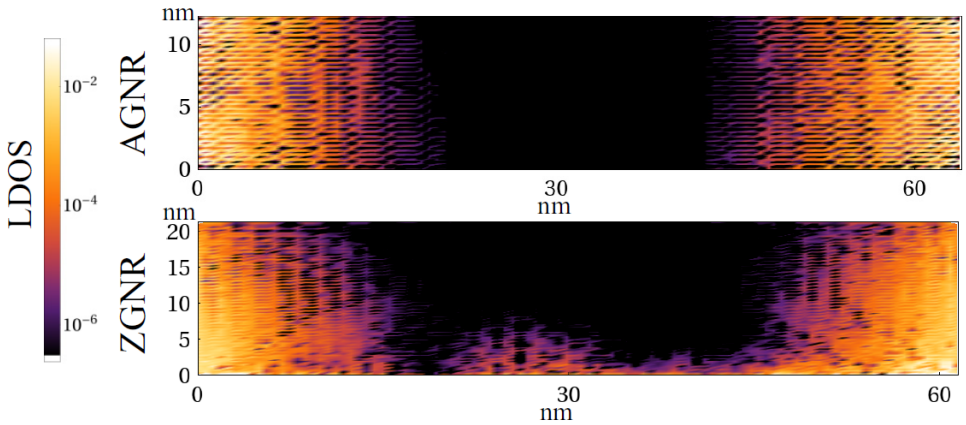

FIGURE 5.4: LDOS maps of a disordered 101-AGNR (top) and 100-ZGNR (bottom) at $E = -0.04|t|$. The impurities are entirely on the A sublattice, corresponding to the bottom edge of the ZGNR, where a non-vanishing DOS is evident. (Figure from Paper I)

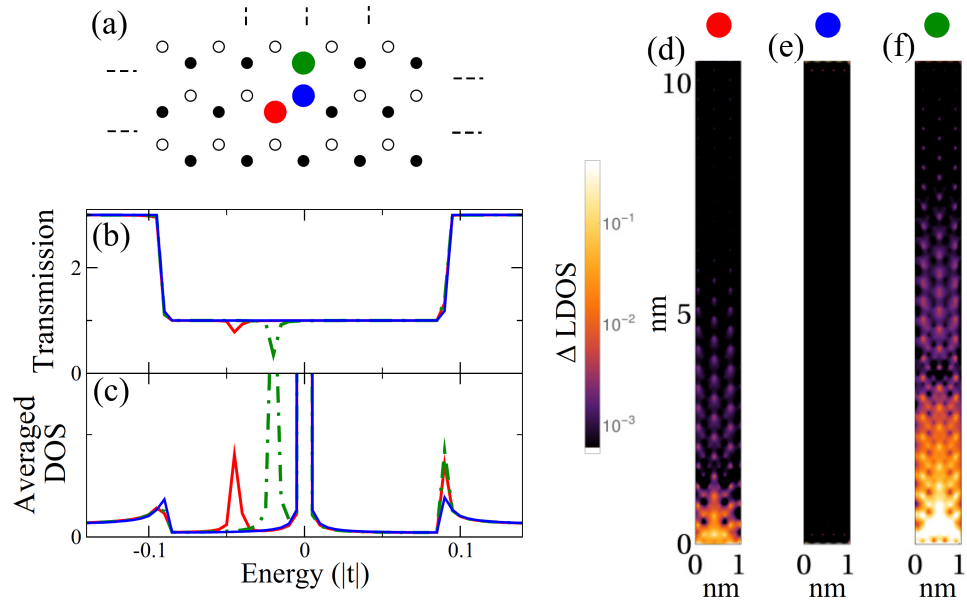

FIGURE 5.5: The transmission (b) and averaged DOS (c) for a 50-ZGNR with a single N impurity located at each of the sites shown by the symbol of the same colour in a). d)-f) map the change in LDOS near the three possible impurity locations, taken at $E = -0.05|t|$ (d) and $E = -0.02|t|$ (e and f). (Figure from Paper I)

the energies near the expected gap. The red and green sites gives dips in the tranmission with corresponding peaks in the averaged DOS. These features, associated with anti-resonances formed by the impurity, have been studied previously in GNRs [65, 74]. Symmetry-breaking edges result in a strong position dependence of the anti-resonance energies. Interestingly, these anti-resonance energies for impurities near the ZGNR edge are within the expected band gap for sites that shares sublattice with the edge atoms, whereas the impurities on the opposite sublattice (similarly to site in ANGRs) have their corresponding features for energies far away from this window. In figures 5.5 (d-f) we plot the change in LDOS caused by impurities near the site mapped. For the two cases where the peaks are within the expectedly gapped region (red and green sites), we have shown the LDOS change for an energy with the DOS peak, whereas in the blue case that has no peak in this region, we have chosen to use the same energy as the green case. In figures 5.5 (d & f) we see large visible triangular resonances in the LDOS near the impurities, corresponding to a single sublattice pattern. In figure 5.5 (e) we see no such resonance pattern for the off sublattice impurity, with barely any visible change in density compared to the pristine case. Consequently electrons in this energy range are scattered by impurities located on the same sublattice as the edge, and not by those on the opposite sublattice. Returning to the asymmetrically disordered ZGNRs, we can now understand the average DOS appearing in figure 5.2 (d) for the ZGNRs as the average of many of single impurity peaks, from impurities close to bottom edge placed on the same sublattice as the edge atoms. As shown in figure 5.4 the DOS vanishes away from this edge, where the net effect from the average potential dominates of the effect of impurity scattering and opens a gap. We confirm this be examining the CPA self-energy on the A sublattice, which in the AGNRs take a real value slightly lower than $\tilde{V}_A$ quite uniformly across the ribbon. For the ZGNRs this true across most of the ribbon except close to the edge associated with the doped sublattice. Here the self-energy becomes complex and the real part varies drastically away from $\tilde{V}_A$. Hence the VCA becomes unable to explain the behaviour near to this edge, as it the effective self-energy deviates far from the effective mass term that the VCA introduces. Increasing the device length will lead to a transport gap as we enter the localization regime. However, this gap is unrelated to the effective mass term or a DOS gap, and is similar to the behaviour observed for ZGNRs with symmetric doping.

The breakdown of the band gap near zigzag edges in asymmetrically doped graphene, may have interesting consequences for other devices than ZGNRs. Grain boundaries with zigzag sections might experience leakage near the boundaries. These grain boundaries break the lattice symmetries in a similar manner [78].

5.4 Sublattice domain interfaces

Another quite relevant interface is the sublattice domain interfaces, where asymmetric distribution changes prefered sublattice. We discussed interfaces of this type in chapter 4 in the case of uniform mass distributions in graphene sheets, where the topological domain wall causes interface states to appear. These types interfaces for asymmetric doping have been shown in experiments [14] as independent of the grain boundaries, and in figure 5.6 we consider an AGNR with a sublattice interface running parallel to the edges in the center of the ribbon so that only the A (B) sublattice is doped in the bottom (top) part of the device. Near this boundary the effective mass term changes sign smoothly resulting in an interface states similar to what we

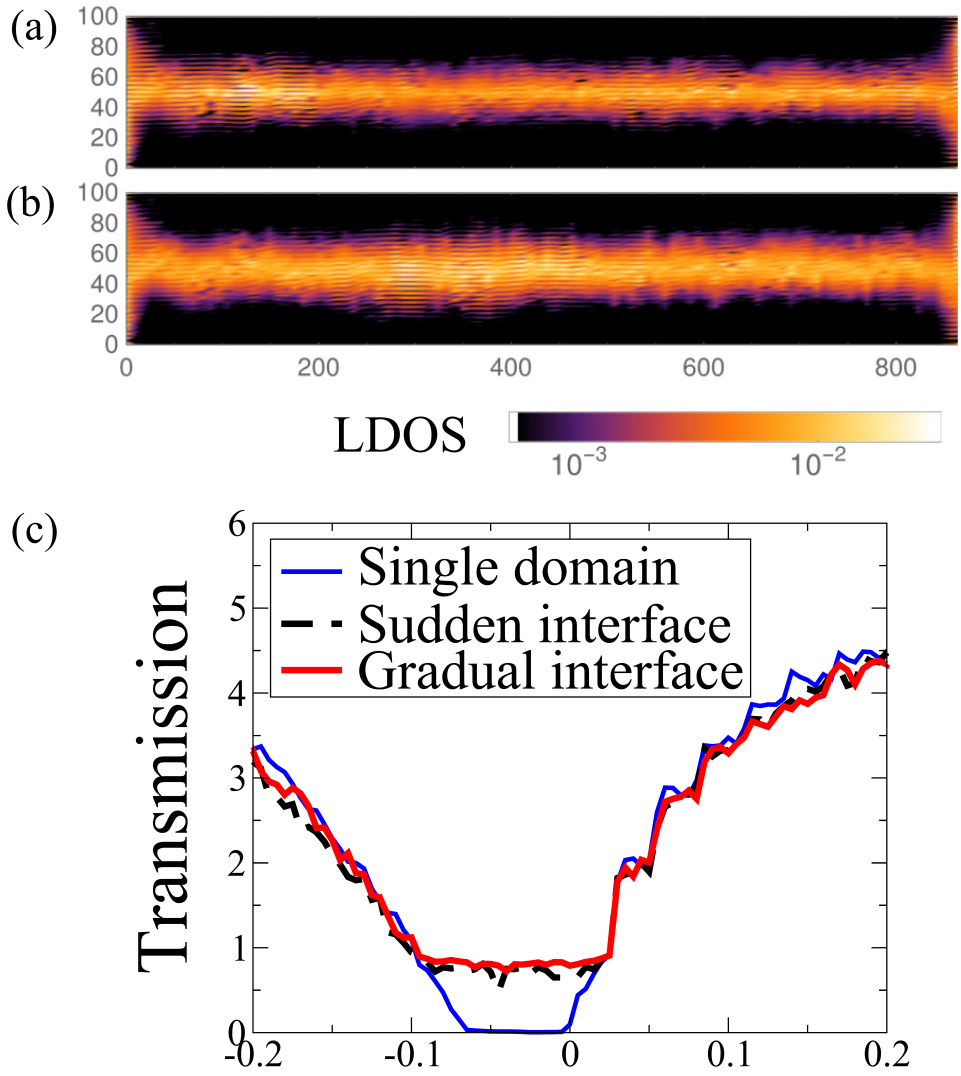

FIGURE 5.6: LDOS maps of asymmetrically doped 200-AGNRs with a) sudden or b) gradual sublattice interfaces running along the centre of the ribbon, taken at $E = -0.04|t|$. c) shows the transmissions for these systems compared to one with a single domain. (Figure from Paper I)

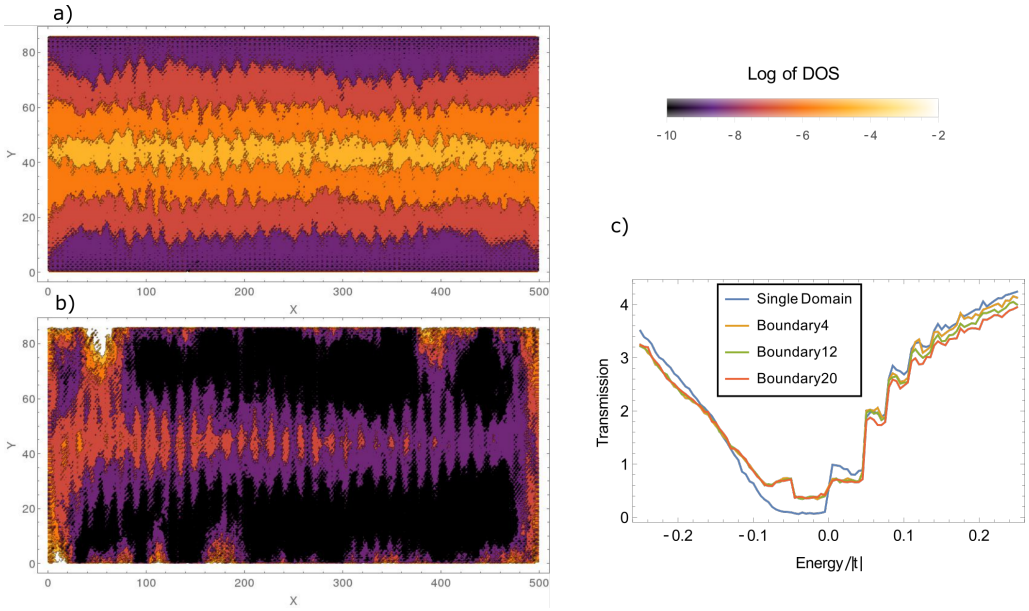

FIGURE 5.7: LDOS maps of asymmetrically doped ZGNRs with a) sublattice not aligned with edges b) sublattice aligned with edges and interfaces running along the centre of the ribbon, taken at $E = -0.04|t|$. c) shows the transmissions for the systems with aligned sublattice compared to one with a single domain.

see in the graphene sheets with Dirac mass interfaces [29]. We confirm this in figure 5.6 (a & b) which has a sudden and graudal change in the dopant concentration respectively. We vary the concentrations linearly over a boundary 4 atoms for the sudden interface and a boundary of 20 atoms for the gradual one. In both cases we see the appearance of a large finite DOS running along the boundary and decaying quickly away from it. Furthermore, this region acts as a 1 dimensional conducting channel, which can be seen by comparing the transmissions in figure 5.6 (c), where we see a finite transmission in the gapped energy range. This corresponds to the mid gap bands seen for the graphene sheet interface.

Similar results can be found for ZGNRs, however one key difference is the existence of two distinct cases. One where each sublattice region agrees with the sublattice on the corresponding edge, and one where they both disagree. In correspondance with the discussion in the previous section, the first case will have increased DOS near the zigzag edges, and the second has no edge states as seen figure 5.7.

5.5 Average doping effects

Electron doping by nitrogen impurities shifts the Fermi energy, E_F, relative to any gap. Accessing the gap region experimentally will involve the application of a gate voltage. While accurate electron-counting can be performed within DFT calculations [18] for single impurities or small disordered regions, this is not feasible for the system sizes considered here or in experiment. Nonetheless, the charge density fluctuation can be approximated from $\delta n \sim \frac{E_D(c_A+c_B)\rho_C}{2}$, where $E_D \approx 0.4$ is the average doping efficiency of nitrogen in GNRs [77] and ρ_C is the density of lattice sites in graphene. For $c_A = 0.1$, we find $\delta n \sim 7.6 \times 10^{13}\,\mathrm{cm}^{-2}$, just inside the range of the most advanced gating methods. [79] $c_A = 0.02$ gives a more realistic

$\delta n \sim 1.5 \times 10^{13}\,\mathrm{cm}^{-2}$, while yielding $E_G \sim 50-200\,\mathrm{meV}$. Gaps from lower concentrations, whilst too small for applications, still allow experimental verification of our results. It is also possible to shift E_F nearer the gap by codoping with a symmetrically distributed p-dopant, at the cost of reducing transmission outside the band gap, due to increased scattering.

5.6 Summary and conclusions

These results demonstrates the importance of edge geometry in doped GNRs. The electronic behaviour predicted for bulk graphene sheets with sublattice-asymmetric doping distribution is highly impacted by the presence of zigzag edges, where the gap-opening behaviour stemming from the effect of the induced effective average potential mass is overshadowed by bound impurity states appearing at the edges, where the doped sublattice corresponds to the edge atoms. These states give rise to a finite DOS and, although quite suppresed, finite electronic transport along the edges.

This dependence on the edge geomtery is relevant beyond GNR devices. Since the majority of samples that has an asymmetric dopant distribution is grown using CVD techniques they often experience edge-like defects in the form of grain boundaries, which can have zigzag-edge-like symmetries. Hence we expect leakage similar to the that of the zigzag edged ribbons, and thus it may prove challenging to detect the band gaps predicted in extended asymmetrically doped graphne sheets.

Finally we have shown the formation of one dimensional metallic channels similar to the topological interface states predicted for Dirac mass interfaces, along the boundaries between domains with different prefered sublattice. We predict that since these interfaces appear in experiments, such metallic channels should be observable using STM measurements. Furthermore these channels have potential as waveguides as they are, away from defects and/or edges, surrounded by gapped material preventing leakage.

An aspect that we didn't consider here, is the potential connections to valleytronics. It could be interesting to check wether the valley polarisation of the interface states are kept even under disorder. Potentially these 1 dimensional states can be used as valley filters, as current for each valley travels in opposite direction, essentially working as valley diode.

In the next chapter we will consider the effect of localised Dirac masses and we show there that the valley behaviour in those types of systems can be kept even in the presence of a high degree of disorder.

6 Circular dots with asymmetric potentials

The previous chapters have dealt with the gap opening properties of sublattice-symmetric potentials and the introduction of *mass* terms, as well as the interfaces between domains and the interaction with edges. In this chapter we consider one more of the exciting possible applications of such systems, namely within the field of valleytronics.

Valleytronics[19] is an emerging field in which the relative occupation of inequivalent local extrema, or *valleys*, in the band dispersion of a material can be exploited to encode, transport and process information in a similar manner to the *spin* degree of freedom for spintronics, or *electronic* current in regular electronics. Many of the two-dimensional materials, and graphene in particular, are particularly promising in this regard due to the presence of two inequivalent valleys formed at the Dirac points, K and K' [2].

A key obstacle to realizing two-dimensional valleytronics is the absense of external controls, analogous to magnetic fields and ferromagnetic contacts in spintronics or electric fields within regular electronics, with which to manipulate and detect valley-polarized currents. In most systems electrons from each valley either behave identically and contribute equally, so that resolving valley-related behaviour from electronic measurements is not possible or intervalley scattering is so high that the information is lost before it can be detected.

For device applications, an all-electronic control of valley properties is highly desireable. The high crystal qualities achievable in graphene, reducing deleterious inter-valley scattering events, have motivated recent work aiming to introduce valley-dependence into graphene-based devices.

A number of device setups have been proposed which are predicted to filter or split electrons according to their valley index, and one can divide these previous approaches into different categories.

First we have atomic-scale engineering, which has the downside of being hard to realise experimentally and difficult to scale up, and hence not suited for device application. These proposal include atomically-precise constrictions, interfacesand defects [20–24].

The second category is nano-scale engineering where more recent efforts have tended to follow one of two main paths: either interaction with a pseudomagnetic field or with sublattice-asymmetric potentials. Furthermore a recent study show a

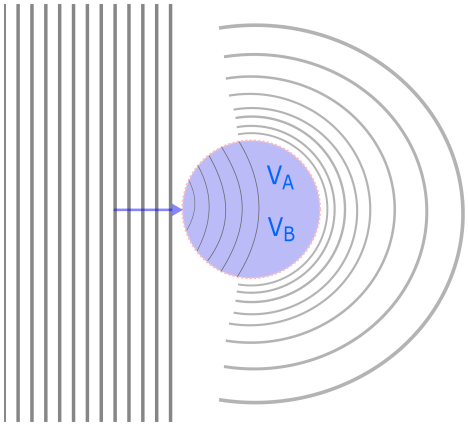

FIGURE 6.1: Schematic of mass dot setup. A plane wave comes in from the left and scatters of the mass dot.

connection between pseudomagnetic fields and non-uniform mass term distributions [38].

Pseudomagnetic fields can be induced by non-uniform strains [34–36] and act with opposite sign on the K and K′ valleys in order to preserve time-reversal symmetry. Systems have induced strain using many different approches such as suspending the graphene sheet [36], bending ribbons [37], or nanobubbles [34, 35]. However, experimental realisation of these systems may be hampered by the relatively small regions of parameter-space that give significant valley effects.

As discussed in chapter 4 sublattice-asymmetric potentials give rise to a valley-dependent chern number and valley-contrasting Hall transport [28]. This is predicted to cause electrons from different valleys to be deflected in opposite directions in an in-plane electric field, and to essentially act as a momentum-space Lorentz force [30–32]. The valley Hall behaviour, predicted in the presence of a mass term, has been suggested as the mechanism behind large non-local resistance measurements in commensurately stacked graphene/hexagonal boron nitride (hBN) systems [33].

However, although semi-classical arguments support a bulk valley current interpretation of the experimental results, to date quantum transport simulations do not.

In this chapter we study circular localised areas of graphene, or dots, with a sublattice-asymmetric potential. As discussed earlier this gives rise to gap of the size $2|\Delta|$, with $\Delta = \frac{V_A - V_B}{2}$ being the so-called mass term. We will refer to these types of dots as *mass dots*, because of this introduction of a mass term. We start by analytically solving the scattering problem for a circular mass dot in the Dirac approximation, a schematic of which is shown figure 6.1, and find a strong valley dependence in the scattered wavefunction at low energies, leading to an angular splitting of valley specific current. This is confirmed by full 1NN tight-binding transport calculations using the patched Green's function approach discussed in section 2.6, where we find that the behaviour is robust against the sharpness of the dot edge and whether or not mass term distribution is uniform or disordered.

6.1 The Dirac model

We first model the system using the Dirac model described in section 3.3, using a generalisation of the method used in Ref. [80], in which a circular dot with uniform potential is investigated, where features similar to those of optical Mie-scattering appears. We include a circular sublattice dependent potential as

$$\mathbf{V} = \begin{bmatrix} V_A\theta(R-\sqrt{x^2+y^2}) & 0 \\ 0 & V_B\theta(R-\sqrt{x^2+y^2}) \end{bmatrix}, \tag{6.1}$$

and hence the Hamiltonian becomes

$$\mathbf{H} = \hbar v_F \begin{bmatrix} \tilde{V}_A\theta(R-\sqrt{x^2+y^2}) & -i\tau\partial_x - \partial_y \\ -i\tau\partial_x + \partial_y & \tilde{V}_B\theta(R-\sqrt{x^2+y^2}) \end{bmatrix} \tag{6.2}$$

with $\tilde{V}_{A,B} = \frac{V_{A,B}}{\hbar v_F}$, and $\tau = \pm 1$ is the valley index. The goal will be to solve the Dirac equation

$$H_\tau \begin{pmatrix} \psi_1^\tau \\ \psi_2^\tau \end{pmatrix} = E \begin{pmatrix} \psi_1^\tau \\ \psi_2^\tau \end{pmatrix} \tag{6.3}$$

which is invariant under the transformation

$$V_A \leftrightarrow V_B, \psi_1^\tau \leftrightarrow \psi_2^{\overline{\tau}}, \psi_2^\tau \leftrightarrow -\psi_1^{\overline{\tau}}$$

and thus we focus on solving it for the K valley, as the equivalent K' results can be calculated by applying this transformation. Since the Hamiltonian has circular symmetry we transform to polar coordinates (r, ϕ). We use the following ansatz for the wave function

$$\psi_m(r,\phi) = e^{im\phi} \begin{pmatrix} a(r) \\ e^{i\phi} i b(r) \end{pmatrix}. \tag{6.4}$$

Inserting this ansatz into equation (6.3), we get the equations

$$\left(\frac{E}{\hbar v_F} - \tilde{V}_A\theta(R-r)\right) a(r) = \left(\partial_r + \frac{m+1}{r}\right) b(r) \tag{6.5}$$

$$\left(\frac{E}{\hbar v_F} - \tilde{V}_B\theta(R-r)\right) b(r) = \left(-\partial_r + \frac{m}{r}\right) a(r). \tag{6.6}$$

We solve for either $a(r)$ or $b(r)$ by combining these two equations. We will go through the calculation only for $a(r)$, as the one for $b(r)$ is similar. If we assume $r \neq R$ we get

$$\left(\frac{E}{\hbar v_F} - \tilde{V}_A\theta(R-r)\right) r a(r) \tag{6.7}$$

$$= \left[\frac{E}{\hbar v_F} - \tilde{V}_B\theta(R-r)\right]^{-1} (r\partial_r + m + 1)\left(-\partial_r + \frac{m}{r}\right) a(r) \tag{6.8}$$

$$= \left[\frac{E}{\hbar v_F} - \tilde{V}_B\theta(R-r)\right]^{-1} \left(-r\partial_r^2 - \partial_r + \frac{m^2}{r}\right) a(r) \tag{6.9}$$

By introducing $\tilde{k}(E,r) = \frac{1}{\hbar v_F}\sqrt{(E - V_A\theta(R-r))(E - V_B\theta(R-r))}$ and $x = \tilde{k}r$, we end up with equation

$$\left(x^2\partial_x^2 + x\partial_x + x^2 - m^2\right) a(x) = 0 \tag{6.10}$$

which is the standard Bessel equation. Solving for $b(r)$ instead we up with a similar equation but with $a \to b$ and $m \to m+1$. We will differentiate between $\tilde{k}(E,r)$ for $R > r$ and $R < r$, by defining

$$k(E) = \frac{1}{\hbar v_F}|E| \tag{6.11}$$

$$q(E) = \frac{1}{\hbar v_F}\sqrt{(E-V_A)(E-V_B)}. \tag{6.12}$$

The full solution to the Bessel equations can be expressed in different ways, but the full result is a linear combination of Bessel functions of the first J_m and second kind Y_m. We choose a basis of Bessel functions of the first kind $J_m(kr)$ and Hankel functions of the first kind $H_m(kr) = J_m(kr) + iY_m(kr)$, which is an equivalent basis. The basis is usefull as standing waves in cylindrical symmetries usually can be expressed as a linear combination of $J_m(kr)$, and the Hankel functions are useful when expanding outgoing waves due to their asymptotic behaviour

$$H_m(x) \to \sqrt{\frac{2}{\pi x}} i e^{ix}(-1)^{m+1} \quad \text{for} \quad x \to \infty. \tag{6.13}$$

The full state for a single m becomes

$$\psi_m(\tilde{k}r,\phi) = \frac{1}{\sqrt{N}} e^{im\phi} \begin{pmatrix} \alpha_1 J_m(\tilde{k}r) + \beta_1 H_m(\tilde{k}r) \\ ie^{i\phi}\left[\alpha_2 J_{m+1}(\tilde{k}r) + \beta_2 H_{m+1}(\tilde{k}r)\right] \end{pmatrix} \tag{6.14}$$

Further restricions on the constants α_i and β_i, can be infered from equations (6.5) and (6.6), also N is a normalization constant.
In the following we set $\hbar = v_F = 1$ for simplicity.
Ouside the dot, for $r > R$ we find the following by inserting our eigenstates in (6.5)

$$Ea(r) = \left(\partial_r + \frac{m+1}{r}\right) b(r) \tag{6.15}$$

$$E\left(\alpha_1 J_m(kr) + \beta_1 H_m(kr)\right) = k\left(\alpha_2 J_m(kr) + \beta_2 H_m(kr)\right) \tag{6.16}$$

$$E\left(\alpha_1 J_m(kr) + \beta_1 H_m(kr)\right) = |E|\left(\alpha_2 J_m(kr) + \beta_2 H_m(kr)\right) \tag{6.17}$$

$$\alpha_1 = \frac{E}{|E|}\alpha_2 \text{ and } \beta_1 = \frac{E}{|E|}\beta_2. \tag{6.18}$$

We can introduce the band index $\eta = \frac{E}{|E|}$ and find that

$$\alpha_1 = \eta\alpha_2 \text{ and } \beta_1 = \eta\beta_2. \tag{6.19}$$

We can find similar conditions inside the dot. First we notice that the outgoing waves, the Hankel functions, diverges as $r \to 0$, and hence we can conclude that $\beta_1 = \beta_2 = 0$. After that we can write the restrictions on the α constants, as

$$(E - V_A)a(r) = \left(\partial_r + \frac{m+1}{r}\right) b(r) \tag{6.20}$$

$$(E - V_A)\alpha_1 J_m(qr) = q\alpha_2 J_m(qr) \tag{6.21}$$

$$(E - V_A)\alpha_1 = q\alpha_2 \tag{6.22}$$

and

$$(E - V_B)b(r) = \left(-\partial_r + \frac{m}{r}\right) a(r) \tag{6.23}$$

$$(E - V_B)\alpha_2 J_{m+1}(qr) = q\alpha_1 J_{m+1}(qr) \tag{6.24}$$

$$(E - V_B)\alpha_2 = q\alpha_1. \tag{6.25}$$

By requiring normalisation, $|\alpha_1|^2 + |\alpha_2|^2 = 1$, and combining the previous equations we find that

$$|\alpha_1|^2 = \frac{|E - V_B|}{|E - V_A| + |E - V_B|} \tag{6.26}$$

$$|\alpha_2|^2 = \frac{|E - V_A|}{|E - V_A| + |E - V_B|}. \tag{6.27}$$

The phase difference between the α constants which is related to the dispersion and is similar to the band choice outside will be denoted as $\eta' = \frac{\alpha_2}{\alpha_1}\frac{|\alpha_1|}{|\alpha_2|}$. We find that

$$\eta' = \begin{cases} 1 & \text{for } V_A, V_B < E \\ -1 & \text{for } V_A, V_B > E \\ -i & \text{for } V_B > E > V_A \\ i & \text{for } V_B < E < V_A \end{cases} \tag{6.28}$$

6.2 Solving the scattering problem

Now that we know the solutions inside and outside the dot, we can solve the scattering problem where we have an incoming plane wave

$$\psi_{\text{inc}} = \frac{1}{\sqrt{2}} \begin{pmatrix} e^{ikx} \\ \eta e^{ikx}. \end{pmatrix} \tag{6.29}$$

We expand the plane wave in terms of Bessel functions to show that this is a valid eigenstate of the Hamiltonian as

$$\psi_{\text{inc}} = \frac{1}{\sqrt{2}} \sum_{m=-\infty}^{\infty} i^m e^{im\phi} \begin{pmatrix} J_m(kr) \\ \eta i e^{i\phi} J_{m+1}(kr) \end{pmatrix}. \tag{6.30}$$

The wave reflected of the dot can be expanded purely in terms of outgoing waves, i.e. the Hankel functions, and given the conditions on the constants we can write the full reflected wave as

$$\psi_{\text{ref}} = \frac{1}{\sqrt{2}} \sum_{m=-\infty}^{\infty} i^m e^{im\phi} c_m^r \begin{pmatrix} H_m(kr) \\ \eta i e^{i\phi} H_{m+1}(kr) \end{pmatrix}, \tag{6.31}$$

and finally we write the transmitted wave as

$$\psi_{\text{trans}} = \frac{1}{\sqrt{2}} \sum_{m=-\infty}^{\infty} i^m e^{im\phi} c_m^t \begin{pmatrix} C_1 J_m(qr) \\ \eta' i e^{i\phi} C_2 J_{m+1}(qr) \end{pmatrix}, \tag{6.32}$$

with

$$C_1 = \sqrt{2}\sqrt{\frac{|E - V_B|}{|E - V_A| + |E - V_B|}} \tag{6.33}$$

$$C_2 = \sqrt{2}\sqrt{\frac{|E - V_A|}{|E - V_A| + |E - V_B|}}. \tag{6.34}$$

Since the Dirac equiation is a first order differential equation, we have to require the wave function to be continuous (differentiable) at the boundary, $r = R$, and we use this to calculate the coefficients c_m^r and c_m^t. Since the wave function has to be continuous for every angle the matching can be done seperately for each mode, and the equations become

$$\begin{bmatrix} H_m(kR) & -C_1 J_m(qR) \\ \eta H_{m+1}(kR) & -\eta' C_2 J_{m+1}(qR) \end{bmatrix} \begin{pmatrix} c_m^r \\ c_m^t \end{pmatrix} = \begin{pmatrix} -J_m(kR) \\ -J_{m+1}(kR) \end{pmatrix} \tag{6.35}$$

resulting in the scattering coefficients

$$c_m^r = \frac{-C_1 J_m(kR) J_{m+1}(qR) + \eta\eta' C_2 J_m(qR) J_{m+1}(kR)}{C_1 H_m(kR) J_{m+1}(qR) - \eta\eta' C_2 H_{m+1}(kR) J_m(qR)} \tag{6.36}$$

$$c_m^t = \frac{J_{m+1}(kR) H_m(kR) - J_m(kR) H_{m+1}(kR)}{C_1 H_m(kR) J_{m+1}(qR) - \eta\eta' C_2 H_{m+1}(kR) J_m(qR)}. \tag{6.37}$$

Using the symmetries of the Bessel and Hankel functions and the symmetries of the Dirac equtaion we find that

$$c_m^r \underset{K \leftrightarrow K'}{=} c_{-m-1}^r \tag{6.38}$$

$$c_m^t \underset{K \leftrightarrow K'}{=} c_{-m-1}^t. \tag{6.39}$$

where $\underset{K \leftrightarrow K'}{=}$ indicates "equal under exchange of the valleys". With these coefficients found, we have all the information we need to find the scattering characteristics of the asymmetric dot system.

We already note some key differences to the gated dot investigated in Ref. [80]. By breaking the sublattice symmetry explicitly get asymmetry between the valleys as seen in equations (6.38) and (6.39). We also notice the posibility of the internal wavenumber being imaginary. This allows for the medium to be dispersive, and prevent internal bound states from forming for energies within the gap of the dot. As seen later this will give rise to vastly different scattering phenomenon compared to the gated dot.

6.3 Physical properties and symmetries

As discussed in section 3.3 we can calculate the both the electronic density of the scattering states and the probality current as

$$n = \psi^\dagger \psi \tag{6.40}$$

$$\mathbf{j} = 2 v_F \psi^\dagger \sigma_\tau \psi. \tag{6.41}$$

Due to the circular structure of the dot and the direction of the incoming wave, we find using the symmetries of the wave function under valley swap that

$$n(r,\phi) \underset{K\leftrightarrow K'}{=} n(r,-\phi) \tag{6.42}$$

$$j_r(r,\phi) \underset{K\leftrightarrow K'}{=} j_r(r,-\phi) \tag{6.43}$$

$$j_\phi(r,\phi) \underset{K\leftrightarrow K'}{=} -j_\phi(r,-\phi), \tag{6.44}$$

i.e. the result for the K' valley is the reflection of the results for the K valley for both the current and electronic density. Hence any difference in valley behaviour is due to an asymmetry of the current and/or electronic density when reflecting the results in the x-axis. These symmetries of the system are useful when calculating the physical quantities, as we can extract full results from one valley halving the computational burden. We also introduce some quanties that will be help when characterising the system. First is the valley current defined as

$$\mathbf{j}_{\text{val}}(r,\phi) = \mathbf{j}_K(r,\phi) - \mathbf{j}_{K'}(r,\phi) \tag{6.45}$$

and the valley polarisation of the current

$$\xi = \frac{|\mathbf{j}_K(r,\phi)| - |\mathbf{j}_{K'}(r,\phi)|}{|\mathbf{j}_K(r,\phi)| + |\mathbf{j}_{K'}(r,\phi)|} \tag{6.46}$$

which will be a number in the range $[-1,1]$, which describes how much weight each of the valleys have. If $\xi = 1$ only current in the K-valley exists, and conversly if $\xi = -1$ only current in the K'-valley exists. Any number in between has mix of the two valleys with $\xi = 0$ corresponds to having an even amount of current in both valleys. We also introduce the scattering efficiency describing the effectiveness of the dot as a scatterer as

$$Q = \frac{\sigma}{2R}, \tag{6.47}$$

where σ is the scattering cross section, given as the reflected current through a concentric circle, normalized to the incoming flux per unit area.

6.4 Far-field approximations

The radial part of the reflected current in the far-field, characterises the scattering of the mass dot. Hence we look at approximating the expressions for the current in this

regime. We start with the current for the K-valley

$$j^r_{\mathrm{ref},K}(r,\phi) = \psi^\dagger_{\mathrm{ref}}\sigma_r\psi_{\mathrm{ref}} \tag{6.48}$$

$$= \psi^\dagger_{\mathrm{ref}}\begin{pmatrix}0 & \mathrm{e}^{-\mathrm{i}\phi}\\ \mathrm{e}^{\mathrm{i}\phi} & 0\end{pmatrix}\psi_{\mathrm{ref}} \tag{6.49}$$

$$= \frac{1}{2}\sum_{m,n=-\infty}^{\infty}\mathrm{e}^{\mathrm{i}(m-n)\phi}\mathrm{i}^{m-n}c^r_m c^{r*}_n \tag{6.50}$$

$$\times \left(H_n(kr)^*, -\mathrm{i}\mathrm{e}^{-\eta\mathrm{i}\phi}H_{n+1}(kr)^*\right)\begin{pmatrix}0 & \mathrm{e}^{-\mathrm{i}\phi}\\ \mathrm{e}^{\mathrm{i}\phi} & 0\end{pmatrix}\begin{pmatrix}H_m(kr)\\ \eta\mathrm{i}\mathrm{e}^{\mathrm{i}\phi}H_{m+1}(kr)\end{pmatrix} \tag{6.51}$$

$$= \frac{1}{2}\sum_{m,n=-\infty}^{\infty}\mathrm{e}^{\mathrm{i}(m-n)\phi}\mathrm{i}^{m-n}c^r_m c^{r*}_n \tag{6.52}$$

$$\times \left(H_n(kr)^*, -\eta\mathrm{i}\mathrm{e}^{-\mathrm{i}\phi}H_{n+1}(kr)^*\right)\begin{pmatrix}\mathrm{i}H_{m+1}(kr)\\ \eta\mathrm{e}^{\mathrm{i}\phi}H_m(kr)\end{pmatrix} \tag{6.53}$$

$$= \frac{1}{2}\sum_{m,n=-\infty}^{\infty}\mathrm{e}^{\mathrm{i}(m-n)\phi}\mathrm{i}^{m-n}c^r_m c^{r*}_n\left(\mathrm{i}H_n(kr)^*H_{m+1}(kr) - \mathrm{i}H_{n+1}(kr)^*H_m(kr)\right) \tag{6.54}$$

Now we take the limit of the Hankel functions for $r\to\infty$: $H_m(kr)\approx\sqrt{\frac{2}{\pi kr}}\mathrm{e}^{\mathrm{i}kr}\mathrm{i}^{-(m+1)}$

$$j^r_{\mathrm{ref},K}(r,\phi) = \frac{2}{\pi kr}\sum_{m,n=-\infty}^{\infty}\mathrm{e}^{\mathrm{i}(m-n)\phi}c^r_m c^{r*}_n \tag{6.55}$$

Using $j^r_{\mathrm{ref},K'}(r,\phi) = j^r_{\mathrm{ref},K}(r,-\phi)$, we get that the valley current can be written as

$$j^r_{\mathrm{ref,val}}(r,\phi) = \frac{2}{\pi kr}\sum_{m,n=-\infty}^{\infty}c^r_m c^{r*}_n(\mathrm{e}^{\mathrm{i}(m-n)\phi} - \mathrm{e}^{-\mathrm{i}(m-n)\phi}) \tag{6.56}$$

$$= \frac{4\mathrm{i}}{\pi kr}\sum_{m,n=-\infty}^{\infty}c^r_m c^{r*}_n\sin\left[(m-n)\phi\right] \tag{6.57}$$

$$= \frac{4\mathrm{i}}{\pi kr}\left(\sum_{m=n} + \sum_{m<n} + \sum_{m>n}\right)c^r_m c^{r*}_n\sin\left[(m-n)\phi\right] \tag{6.58}$$

$$= \frac{-8}{\pi kr}\sum_{m<n}\mathrm{Im}\left(c^r_m c^{r*}_n\right)\sin\left[(m-n)\phi\right] \tag{6.59}$$

similarly we can find the total current

$$j^r_{\mathrm{ref,total}}(r,\phi) = \frac{2}{\pi kr}\sum_{m,n=-\infty}^{\infty}c^r_m c^{r*}_n(\mathrm{e}^{\mathrm{i}(m-n)\phi} + \mathrm{e}^{-\mathrm{i}(m-n)\phi}) \tag{6.60}$$

$$= \frac{4}{\pi kr}\sum_{m,n=-\infty}^{\infty}c^r_m c^{r*}_n\cos\left[(m-n)\phi\right] \tag{6.61}$$

$$= \frac{4}{\pi kr}\sum_{m=-\infty}^{\infty}|c^r_m|^2 + \frac{8}{\pi kr}\sum_{m<n}\mathrm{Re}\left(c^r_m c^{r*}_n\right)\cos\left[(m-n)\phi\right]. \tag{6.62}$$

We can use the far-field approximation to calculate the scattering efficiency. Since we have an incoming plane wave, the incoming current per unit area is just 2 (1 for each valley), and the scattering cross section reduces to just calculating the total reflected

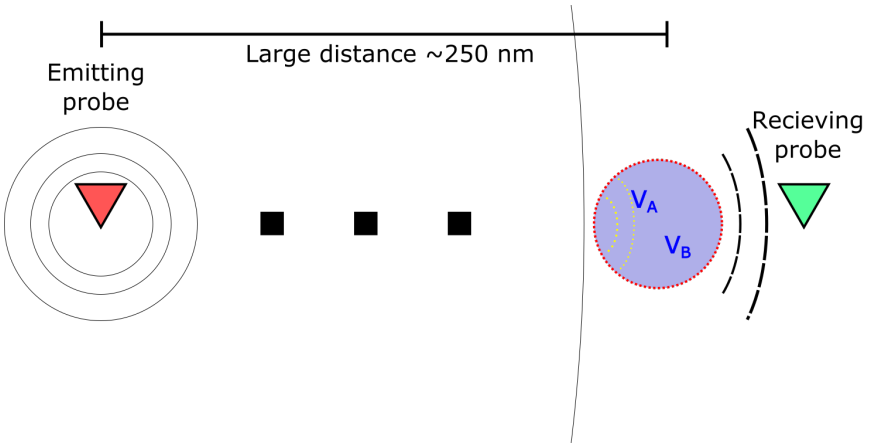

FIGURE 6.2: Schematic of dual probe setup. A circular wave is emitted from the probe far to the left of the dot. This wave becomes approximately plane near the mass dot.

flux through a concentric circle.

$$\sigma = \frac{1}{2} I^r_{\text{ref}} = \frac{1}{2} \int_0^{2\pi} r j^r_{\text{ref,total}}(r,\phi) \mathrm{d}\phi \tag{6.63}$$

$$= \frac{4}{k} \sum_{m=-\infty}^{\infty} |c^r_m|^2 \tag{6.64}$$

resulting in a scattering efficiency of

$$Q = \frac{2}{kR} \sum_{m=-\infty}^{\infty} |c^r_m|^2. \tag{6.65}$$

We can also find the valley polarisation of the reflected current in the far-field approximation as

$$\xi_{FF}(\phi) = \frac{j^r_{\text{ref},K'}(r,\phi)}{j^r_{\text{ref,total}}(r,\phi)} = \frac{\mathrm{i} \sum_{m,n=-\infty}^{\infty} c^r_m c^{r*}_n \sin\left[(m-n)\phi\right]}{\sum_{m,n=-\infty}^{\infty} c^r_m c^{r*}_n \cos\left[(m-n)\phi\right]} \tag{6.66}$$

Finally we introduce a system parameter that characterises the average valley splitting of the scattered current. This is done by finding the average valley splitting of the far-field current for the upper half plane,

$$\xi_{\text{avg}} = \frac{1}{\pi} \int_0^{\pi} \xi_{FF}(\phi) \mathrm{d}\phi \tag{6.67}$$

We will in the results shorten the notation of the far-field reflected current to j^{ffr} to save space.

6.5 Atomistic dual probe spectroscopy simulation

Whilst the Dirac approximation can explain the behaviour of the individual valleys, it explicitly excludes any intervalley interaction. To test the accurracy of this approximation we also model the same mass dot system in a theoretical dual probe setup,

a schematic of which can be seen in figure 6.2. We do a full 1NN tight binding description of graphene with the sublattice dependent on-site energies described by the Hamiltonian,

$$\mathbf{H} = \sum_{<ij>}^{A,B} t\left(\hat{a}_i^\dagger \hat{b}_j + c.c\right) + \sum_i^A V_A(\mathbf{r}_i)\hat{a}_i^\dagger \hat{a}_i + \sum_j^B V_B(\mathbf{r}_j)\hat{b}_j^\dagger \hat{b}_j \tag{6.68}$$

where i and j index the site in the A and B sublattice respectively, with $\hat{a}^{(\dagger)}_i$, $\hat{b}^{(\dagger)}_j$ are the standard annihilation (creation) on the sublattices and $t \ -2.7$eV is the nearest neighbour hopping integral. We include two weakly coupled STM-style probes via their self-energy with corresponding broadening terms $\mathbf{\Gamma}_{1,2}$. Using the patching techniques as described in section 2.6 we connect the 2 probes and the dot, which each have an individual graphene patch. We calculate the required Green's function elements using the analytical expression for a 1NN tight binding pristine graphene sheet, and calculate the Fourier components by numerically integrating equation (3.31).

6.5.1 Physical quantities in the TB model

We can keep track of the injected states by considering the *injected spectral density* from the emitting probe $\mathbf{A}_1(E) = \mathbf{G}(E)\mathbf{\Gamma}_1\mathbf{G}$ from equation (2.15) , and by projecting this spectral density onto the pristine graphene states (equation (3.9)) we can find the local distribution of scattered states in k-space as

$$\rho(k) = \langle \psi_k | \, \mathbf{A}_1 \, | \psi_k \rangle \tag{6.69}$$

from which we can calculate the tight binding valley polarisation as the difference in spectral density weight between the two valleys normalised by the total spectral density,

$$\xi_{TB} = \left(\sum_{k\in K} \rho(k) - \sum_{k\in K'} \rho(k) \right) \Big/ \sum_{k\in K,K'} \rho(k) \tag{6.70}$$

We can also calculate the usual electronic properties described in chapter 2, namely the transmission between the probes $T_{21} = \mathrm{Tr}[\mathbf{A}_1\mathbf{\Gamma}_2]$, which we can compare to the far-field current from the Dirac model, and the density of states $\mathrm{LDOS}(i) = \frac{-1}{\pi}\mathrm{Im}[\mathbf{G}_{ii}]$.

6.6 General scattering properties

We will use units where $\hbar = v_f = 1$ and introduce the mass term $\tilde{\Delta} = \frac{\tilde{V}_A - \tilde{V}_B}{2}$ and the average shift $\tilde{V}_0 = \frac{\tilde{V}_A + \tilde{V}_B}{2}$. We first consider the class of pure mass dots with $\tilde{\Delta} = 1$, $\tilde{V}_0 = 0$. We focus on dots of size $R = 4.5$ first. The general scattering characteristics can be found by analysing the far-field current which is plotted in figure 6.3. Panel a) show the forward scattering behaviour ($\phi = 0$) of the far-field current and panel b) the corresponding scattering efficiency calculated by the Dirac model, and shown as a solid blue line and solid black line respectively. As opposed to potential dots, where sharp-peaked features exists corresponding to bound states within the dot [80], we see that both the far-field current and the scattering efficiency curves are relativly featureless. This is especially true for energy within the "gap", $-|\tilde{\Delta}| < E < |\tilde{\Delta}|$ where the curves are mostly monotonic or flat. This is to be expected for a mass type

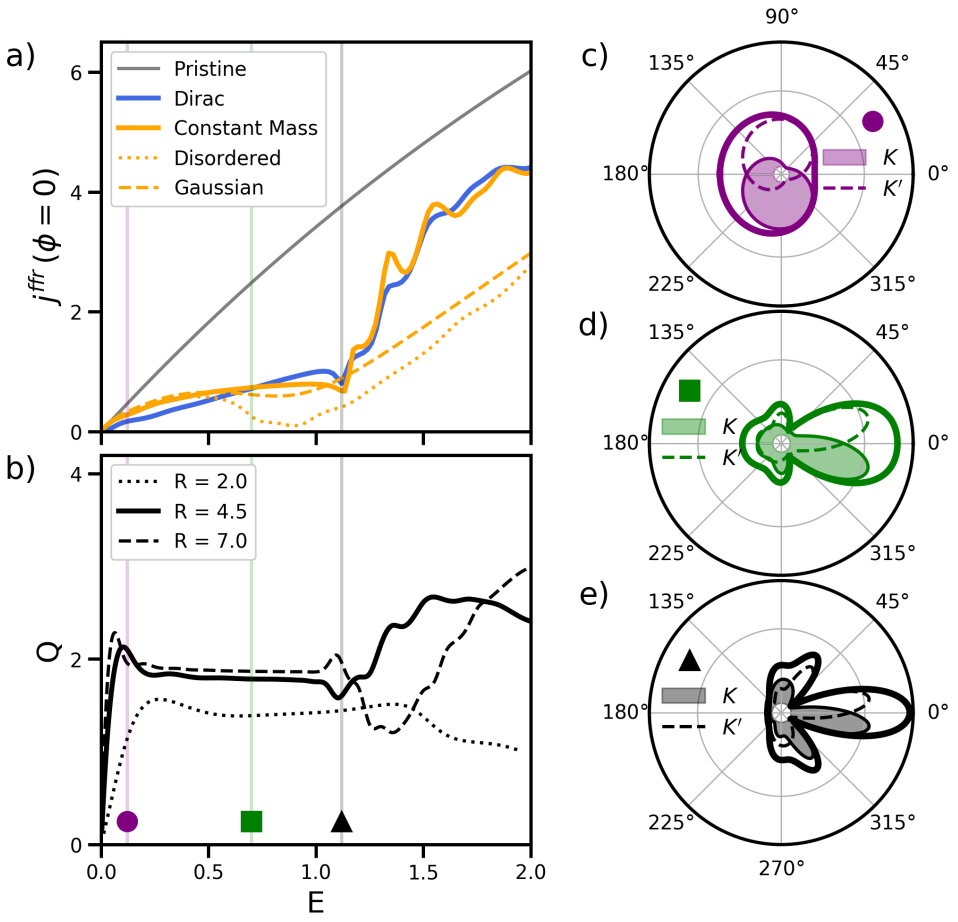

FIGURE 6.3: a) The far-field component of the reflected current along the x-axis ($\phi = 0$) for the constant mass system calculated using the Dirac (solid blue) and atomistically (solid orange). This is compared to calculation of the pristine system (solid grey) and non-uniform mass distributions, gaussian (dashed and dotted orange) also done atomistaclly. b) Scattering efficiency Q for constant mass dots of different radii over the same energy range. c)-e) Total (bold) and individual valley angular scattering profiles, $j^{ffr}(\phi)$ for the the three energies highlighted in a) and b). (Figure from Paper II)

dot as the gap in electronic states moves the internal states to higher energies, leaving no resonance interactions between the inside and the outside. Furthermore mass dots suppress Klein tunneling leaving less forward scattering than in the case of the potential dot [80]. We note that, for energies in the gap, Q is almost constant after reaching a peak, and this constant behaviour is consistent with uniform scattering and a lack of resonant states. This peak follows a regular pattern as function of E and R, with the peak lying around the energy the Fermi wave length corresponds to the dot diameter whereas for lower energies the wavelengths are to long to properly resolve the dot.

6.6.1 Valley specific scattering

The forward scattering alone cannot explain the individual valley behaviour, as the valleys, by symmetry, have to contribute equally for $\phi = 0$, and hence we need to examine the angular profile of the scattered current to analyse the difference of the currents between the K and K' valleys. The three energies marked with coloured symbols and lines in panels a) and b) (E=0.12,0.70,1.12), are the ones we analysed in more detail in the corresponding panels c)-e). We have marked the total far-field current as a bold outline with the K and K' as a shaded and unshaded areas respectively. We see that the current from the individual valleys are indeed exactly antisymmetric in the x-axis and that the individual valley has a primarily preferred direction. This is most clearly seen for the $E = 0.12$ for where the valleys almost exclusively in the transverse direction giving a large spatial splitting of the valley specific currents. As the energy increases the primary lobes moves forward, the angle decreasing with energy and we also see an increasing number of secondary preferred direction. Both of which are consistent with appearance of higher order angular modes $e^{i\phi}H_m(kR)$ present in the reflected current.

6.6.2 Comparing Dirac and tight binding

To check the validity of the Dirac model, we compare the forward far-field current, $j^{ffr}(\phi = 0)$, to the transmission in the tight binding model, T_{21}, from a probe to the far left of the dot, simulating the incoming plane wave, and to a reciving probe close behind the dot, as shown in the schematic. The transmission will in general capture the full wave (both the incident and reflected parts), but just behind the dot we expect the scattered components to dominate. The tight binding results are shown in figure 6.3 in panel a) as orange lines, with different mass term profiles; constant mass (solid line), Gaussian (dashed line) and disordered (dotted line). The disordered distribution was made by chosing sites within the dot region with a 5% probability and applying a potential of $V_{A/B,\text{Dis}} = \frac{\tilde{V}_{A/B}}{0.05}$ to keep the average mass term the same. We see that the constant mass distribution case has excellent agreement with the Dirac calculation, where as both the alternative mass distributions deviates for larger energies. We will discuss these alternative distribution is more detail later.

6.7 Local electronic- and valley behaviour near the dot

We want to further analyse the electronic- and valley flow in these dot systems, and in order to do so with investigate the local electronic- and valley properties near the dot for the same three energies we selected for the angular analysis of j^{ffr}. The results of this investigation are shown in figure 6.4. The left most panels shows the

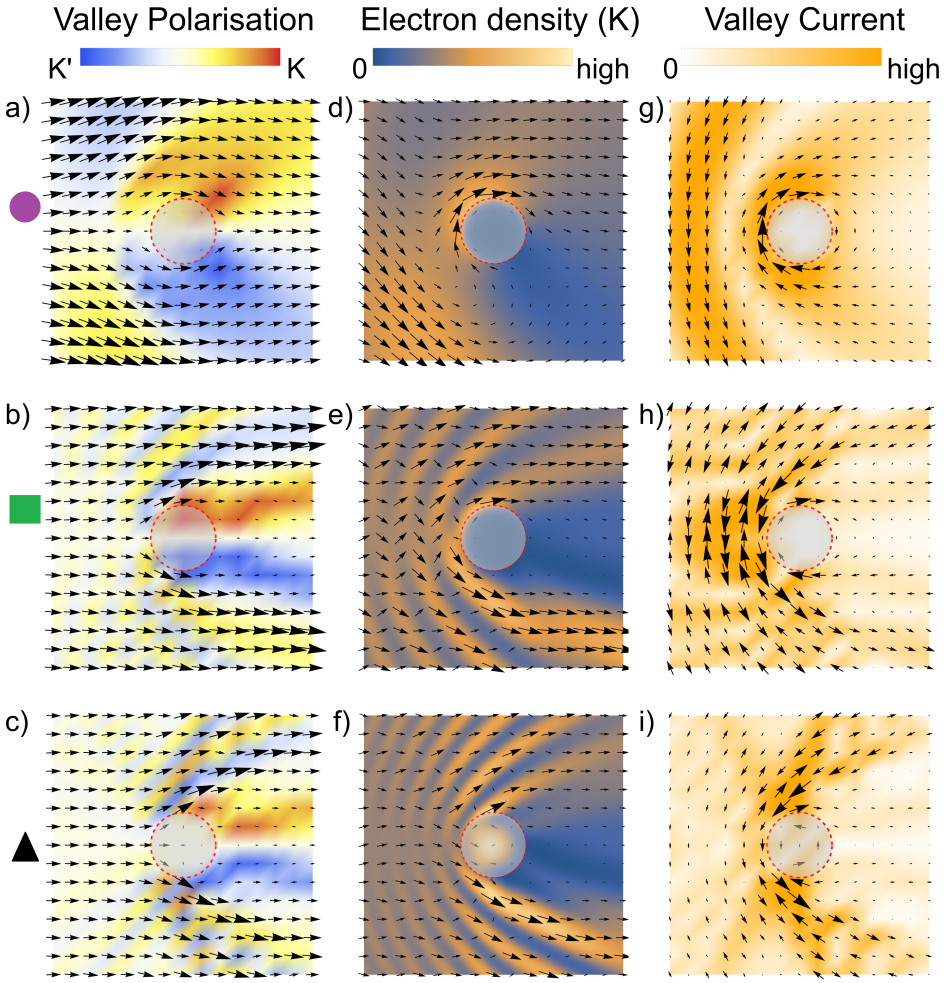

FIGURE 6.4: Local electronic behaviour near the mass dot. The left most column (panels a-c) shows the total current as arrows with the valley polarisation shown as background colour. The second column (panels d-f) show the valley specific current for the K valley as arrows, with the corresponding electronic density of the scattering state as background colour. The final column (panels g-i) show the local valley current as both arrows and background color. The individual rows corresponds to the three energies indicicated in figure 6.3 with panels a,d,g having $E = 0.12$, b,e,h $E = 0.70$ and c,f,i $E = 1.12$. (Figure from Paper II)

local probability current (black arrows) with valley polarisation of that current as a background colour map. The middle panels shows the valley specific current for the K valley (black arrows) with the electronic density of the scattered state as the background colour map. The corresponding currents and density of the K' valley is the mirror image of the K valley in the x-axis. The final column of panels shows the effective valley current flow through the system.

6.7.1 Valley polarisation

First we inspect the valley polarisation of the current as shown in panel a) for the first energy $E = 0.12$. At first glance there seems to be some disagreement between the local behaviour and the far-field reflected behaviour shown in figure 6.3 panel c). Even though there is a large valley splitting in both graphs the individual valleys seem to have opposite preferred directions in the plots. Locally it seems that current above the dot is largely K-polarised, where as the far-field current shows almost exclusively K' current above the dot. To reconcile these two plots, we first note the difference in quantity shown in the two plots. Where the plot in figure 6.3 shows only the reflected current the local plot shows interference between the incoming and reflected waves. Though the reflected wave keeps the same angular profile for all distances the interference with the incoming wave, which is constant in vertical slices, leads to regular interference fringes seen in the local valley polarisation plot. The distance between the fringes are related to the fermi wave length of the electrons, and as we can see in panels b) and c) the increase in energy decreases the distance between the fringes as the wavelength shortens. This effect can also be directly seen from equation (6.11) where the electron wave number is directly propertional with the energy.
While the amplitude of the incoming remains constant the amplitude of the reflected wave tapers of as roughly $1/r$ decreasing the strength of the fringes as the distance from the dot increases, and hence the strength of the valley polarisation which comes from the asymmetry of the reflected wave weakens with distance.

6.7.2 Valley polarised current

By looking at the middle panels in figure 6.4 we see exactly the path that the current in the K valley actually takes. The current is guided by fringes in the valley specific electronic density, and interestingly we see that the chiral nature of the mass dot slightly moves the dark spot from directly behind the dot to slightly off center. The suppressed forward scattering only really appears when the first nodes are pushed enough forward for the valley specific densities that they start to overlap as seen for the second energy $E = 0.70$. We also note that the valley specific current alternates between an upward and downward path which is consistent with the valley polarisation seen in the first column.

In the third and final column shows that the effective valley current manifests as a set of counter propergating channels, with the first channel closest to the dot wrapping around and vanishing on the back side of the dot. The second channel mimics the far-field behaviour the most as it is the strongest of the fringes that has a long distance effect.

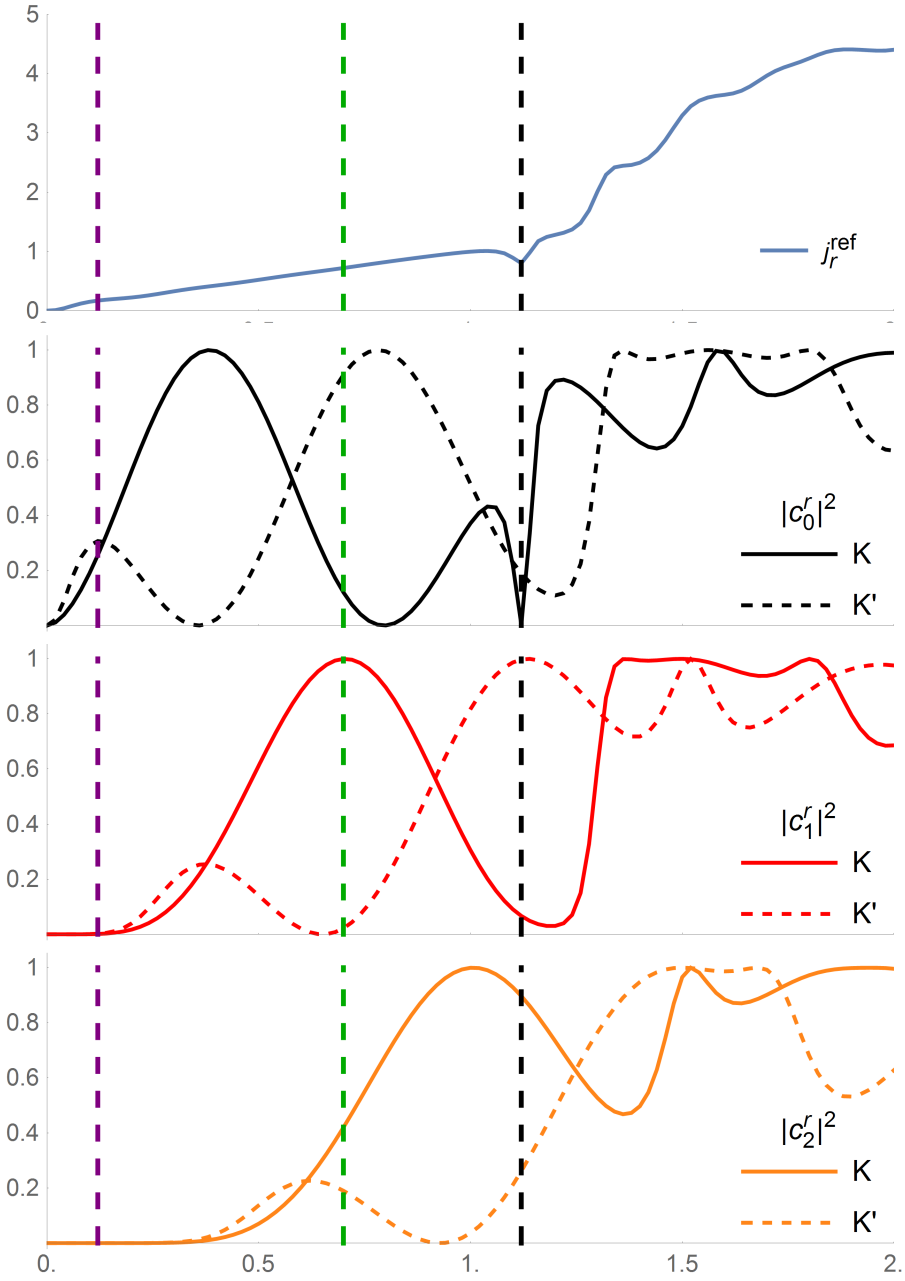

FIGURE 6.5: The amplitude of the reflection modes for the mass dot, with the 3 chosen energies indicated as coloured vertical lines. (Figure from Paper II)

6.8 Interpretation in terms of reflected and internal modes

The first three reflection modes for each valley (and by symmetry the first three negative index modes, $-3, -2, -1$) are shown in figure 6.5, with the chosen energies indicated again as three vertical dashed lines, coloured as in figures 6.3 and 6.4. The onset of the reflection modes are very regular, with the modes just being shifted version of each other, at least for energies inside the gap. For these energies in the range $-|\tilde{\Delta}| < E < |\tilde{\Delta}|$, the internal wave number, q is purely imaginary. In a parallel to the Beer-Lambert law for optics this leads to exponentially fast attenuation away from the boundary leaving no resonant internal states. For larger energies we have the onset of internal bound states as q becomes real, and the coupling between the internal and reflected modes are immedieatly seen in the loss of regularity of the reflection coefficients. Especially the first internal resonant state which peaks at around $E = 1.12$ (black energy) can be clearly seen affecting forward scattering resulting in the first dip in j^{ffr}, and we see a corresponding dip in the zero reflection mode for K. The (anti)symmetry of the of the sublattice potentials and the corresponding valley symmetry gives a corresponding K' dip for $E = -1.12$, and in general all of the modes have a mirror image for the negative energies with the caveat that the modes are valley swapped, as remarked in equations (6.38) and (6.39). We note that fewer modes will usually lead to a larger valley splitting. This can be understood from the far-field valley equation (equation (6.59)), as more modes gives rise to more independent sine functions that tend to cancel each other out.

6.8.1 The role of the potential offset of the dot

We can also introduce a non-zero $\tilde{V}_0$ term. There are two interesting limits not including $\tilde{V}_0 = 0$ already discussed at length, namely $\frac{\tilde{V}_0}{\tilde{\Delta}} >> 1$ (or $\to 0$) and $\tilde{V}_0 = \Delta$. By inspecting equations (6.36) and (6.37) we can check we happens in these limits. For $\frac{\tilde{V}_0}{\tilde{\Delta}} >> 1$ we can set $V_A \approx V_B$, and we immediately see that the equations reduces to

$$c_m^r = \frac{-J_m(kR)J_{m+1}(qR) + \eta\eta' J_m(qR)J_{m+1}(kR)}{H_m(kR)J_{m+1}(qR) - \eta\eta' H_{m+1}(kR)J_m(qR)} \tag{6.71}$$

$$c_m^t = \frac{J_{m+1}(kR)H_m(kR) - J_m(kR)H_{m+1}(kR)}{H_m(kR)J_{m+1}(qR) - \eta\eta' H_{m+1}(kR)J_m(qR)}. \tag{6.72}$$

the same equations as seen for the gated dot [80], which is expected as the mass term becomes negligible.
The other limit is perhaps less intuitive but again inspection of the scattering coefficients in equations (6.36) and (6.37) yields an interesting result. We find the symmetry that $c_m^r = c_{-m}^r$ and $c_m^t = c_{-m}^t$. Using this symmetry we can calculate the valley current in far-field approxmiation from equation (6.57)

$$\frac{4\mathrm{i}}{\pi kr} \sum_{m,n=-\infty}^{\infty} c_m^r c_n^{r*} \sin\left[(m-n)\phi\right]. \tag{6.73}$$

Excluding $m = 0$ and $n = 0$ this leaves four terms with identical coefficients, namely (m, n), $(-m, n)$, $(m, -n)$ and $(-m, -n)$. Since $\sin x = -\sin(-x)$ these terms cancel out each other in pairs. If only $m = 0$ (or $n = 0$) then there are two terms with identical coefficients also canceling out each other, leaving the term with $m = n = 0$, which is identically zero. In total we are left with no valley current, which means we

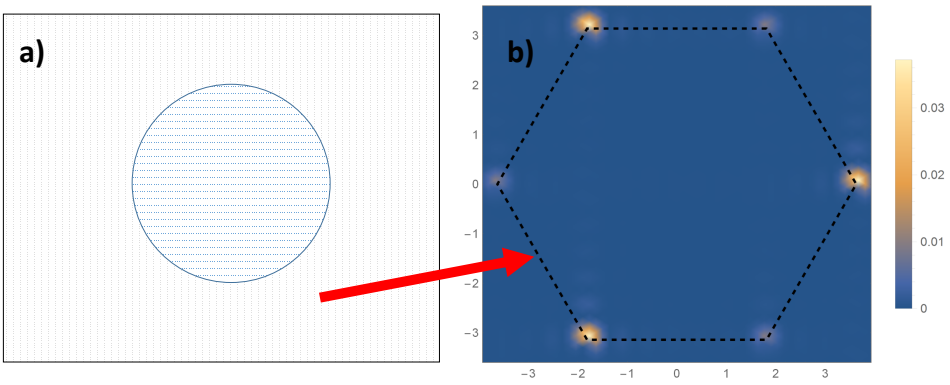

FIGURE 6.6: a) Shows a schematic of a grid used to find the local k-space distribution. b) Shows a single k-projection with valley imbalance.

cannot expect valley splitting by only affecting a single sublattice, such as the case of substitutional doping with only a single doped sublattice, similar to what was considered in chapter 5.
Studying the ξ_{avg} with varying $\tilde{V}_0$ it turns out that this symmetry point is the cross over point where the valleys swap preferential direction, i.e. the preferential direction for each valley in the far-field is opposite for $\tilde{V}_0 < \tilde{\Delta}$ and $\tilde{V}_0 > \tilde{\Delta}$.

6.9 Robustness of the local effects

By using equations (6.69) and (6.70), we can also find the valley polarisation in the tight binding model. This is done by dividing the device region into a 15 by 15 grid and projecting the spectral function of all sites within each grid onto pristine graphene states in k-spaces. The result is a k-space distribution which we can turn into the local valley polarisation of that part of the grid. A schematic is shown in figure 6.6.

By also calculating the bond currents we can get similar local valley polarisation plots as those generated using the Dirac approximation. We show the result of a number of these calculations in figure 6.7 for the energy $E = 0.12$ [1] (the purple energy). The panels a-d show a constant dirac mass distribution, a Gaussian mass distribution, disordered mass distribution with concentration 5% and a disordered mass distribution with concentration 1%, respectively. The disordered mass distributions, as discussed previously, is made by chosing the sites at random with a certain concentration and applying an onsite potential scaled with the concentration to keep the average the same.
For all mass distribution we see a very similar local current and valley distribution as in figure 6.4 panel a). Some of the mass distributions allow leakage through dot, and the specifics of the current very close to the dot will be dependent on the exact mass distribution. This excellent agreement can be understood from figure 6.3 panel

[1] The tight binding energies and distances have a conversion factor to match up with the Dirac. $0.1|t|_{TB} = 1_{\text{Dirac}}$, where a 10nm dot corresponds to $R = 4.5$.

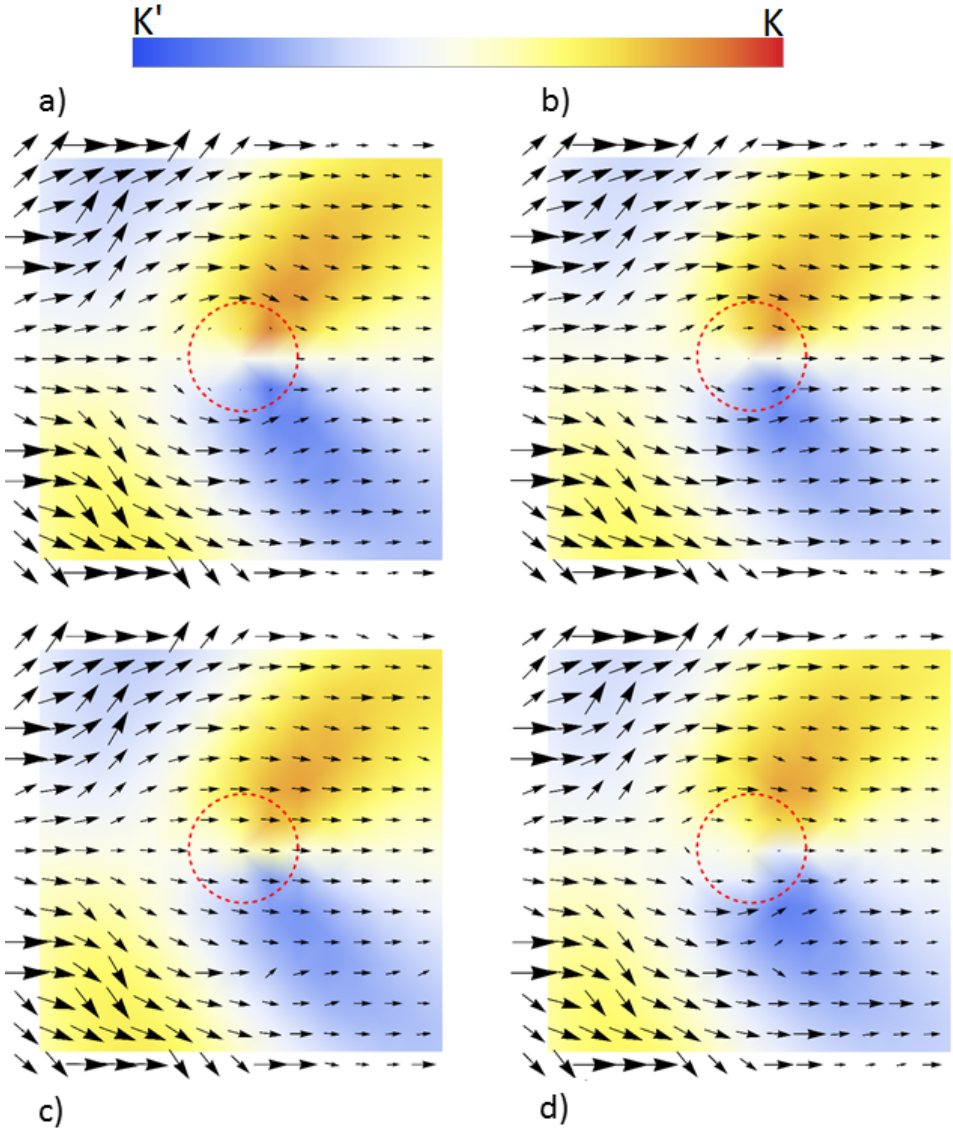

FIGURE 6.7: Local valley polarisation and bond currents using the tight binding model with varying mass distributions for a 10nm dot. The colourmap shows the valley polarisation and the black arrows indicate the bond currents. a) Constant mass distribution. b) Gaussian mass distribution. c) Disordered mass distribution with $C = 5\%$. d) Disordered mass distribution with $C = 1\%$.

a) where for low energies all of the tranmissions agree. Using the same mode of interpretation we can predict that this agreement will start to break down for higher energies, which is indeed the case.

6.10 Summary and conclusions

We have shown that for circular dots in the Dirac model, including a mass term, leads to non-trival valley specific patterns in both current and electronic density. We also show that these valley specific patterns are present in a fully atomistic model which includes intervalley scattering and can survive even in the presence of disorder. Specifically we see a large angular splitting of currents belonging to different valleys allowing the dot to work as an effective valley splitter. By tuning the system energy the strength and direction of the valley current can be altered, allowing for external electronic control, using a back gate, of the valley splitting.

In summation our findings suggest that regions of local sublattice-asymmetry provide a robust platform for engineering valleytronic devices, and while the fabrication of individual mass dots is perhaps a very difficult, we expect systems with fluctuating mass term, induced perhaps in Moire structures like those of in Ref. [33], to give rise to similar qualitative features.

We suggest that further calculations should be made to study how scattering characteristics of the system translate into behaviour of arrays of mass dots. Also the results should be veryfied experimentally, either by explaining an already existing experiment using this new approach, i.e. as an effect of localised mass terms, or by designing a dot type system and injecting a valley polarised current in it, using perhaps the valley filtering states from sublattice interfaces or a similar setup [21]. One could also check the behaviour of the total current experimentally which might not directly verify the valley behaviour but still help validate the model. This can be done with a dual probe setup similar to that used in the tight binding model.

7 Implementation of advanced patching methods

Wanting to expand on the patching method discussed in section 2.6, and used on graphene devices in chapter 6, as well as in Refs. [34, 44, 81], so that they can be applied to other materials than graphene we setup a general method that is material independent, and discuss convergence considerations.

The goal is to be able to generate pristine Green's functions from a single unit cell of a periodic material. We want these Green's functions to be accurate for large unit cell separation, so that they can be used in calculations where modifications are made to the pristine material locally and detected with distant probes, or alternatively calculate interactions between modifications that are spacially separated.

In the previous chapter we calculated the pristine graphene Green's functions by relying on the integration of the closed analytical expression that exists for the 1NN tight binding model, to reduce the number of numerical intergrals from 2 to 1, and then directly recover each individual Fourier component. Here we suggest an alternative method that does not require an effective algortihm to deal with system where such closed form expressions does not exist. It relies on the ability to calculate (or sample) the Green's function inside a single unit cell of the periodic material for many different values in k-space. We can then generate the Green's function matrix elements required for the patching equations (2.43-2.47) using effecient discrete Fourier transformation algorithms. This offers distinct advantages over direct numerical integration of the Green's function, which essentially also relies on the ability to sample a single unit cell, and will allow for a standardised that can be used for any material which can described in local orbital bases.

This includes materials such as black phospherous, MoS_2 and bilayer graphene [82–85], and also super cell structures consisting of graphene such as antidot lattices [86–92].

7.1 Building a library

One of the strengths of the patching method with pristine materials are the fact that the same pristine Green's functions can be used for many distinct calculations. It can be beneficial to store already calculated pristine Green's functions in a library

for later use, as this will limit the amount of calculations one has to do, and allow you to increase the accuracy over time, by using spare computational time to do extra calculations. More technical details involving the creation of a library that we considered during this ph.d. is discussed in appendix A.

7.2 Using multi dimensional Fourier transforms

Until now the material we have considered, graphene, has been 2-dimensional. However, both 1 and 3 dimensional materials can also be treated using the same formalism. If the material has $n-$dimensional periodicity, we will in general need to do the n-dimensional Fourier transform to get the necessary coefficients. Using a sampling of the periodic Green's function $\mathbf{G}(\mathbf{k}, E)$ we will use the efficient discrete Fourier algorithms that exists for sampled signals: algorithms better knowns as FFT's or Fast Fourier Transforms.

For each periodicity number, k_i, we have $k_i \in [0, 2\pi)$. We sample the Green's function k_i with regular spacing, N_k times, and hence get a discrete set of sampled k, $k_1, k_2, ..., k_{N_K}$.

We can now calculate the Fourier components that correponds directly to real space separations of an integer number times the lattice vector, i.e. the m'th fourier component corresponds to a separation vector $\mathbf{r} = m\mathbf{a}_i$. This generalises to more dimensions so that a Fourier component with coefficients $m_1, m_2, ..., F_{m_1,m_2,...}$ corresponds to the real space separation $\mathbf{r} = m_1\mathbf{a}_1 + m_2\mathbf{a}_2 + ...$ To put it in differently

$$\mathbf{G}(E, R_j - R_i) = \mathbf{G}(E, m_1\mathbf{a}_1, m_2\mathbf{a}_2, ..) \tag{7.1}$$

$$= \int \mathrm{d}\mathbf{k}\mathbf{G}(E, \mathbf{k})\mathrm{e}^{\mathrm{i}\mathbf{k}\cdot(R_j - R_i)} \tag{7.2}$$

$$= F_{m_1,m_2,...} \tag{7.3}$$

7.2.1 Optimisation and limitations

The first immediate problem that arises when using sampling methods is a phenomenon known as aliasing. If we have a k-sampling frequency in a single dimension of $f_s = \frac{1}{N_k}$, then any frequencies higher than $0.5f_s$ (also called the Nyquist frequency) have aliases appearing. The FFT's thus usually filter out any coefficients higher than $\frac{1}{2}N_k$ as they cannot be trusted. This gives us the absolute minimum number of k-points needed for any real space separation. Furthermore when choosing the k-points it is worth noting that FFT's have certain sampling rates that are more efficient than others. Firstly any power of 2 is by far the most efficient, with powers of 3 being the second most optimum. Any combination of the type 2^i3^j, can also be used, but significant slow down will be experienced if other numbers are chosen.

A very different limitation comes in the form of memory constraints caused the size of the matrices used in the Fourier transform. A rough estimation of the minimal memory usage, M, to do an n-dimensional FFT with N_k points for every dimension, can be calculated as

$$M = (N_k)^n S_C \tag{7.4}$$

where S_C is the memory size of a single complex number. This number is the storage amount required to just store the individual G(k) values. Typically $S_C = 64\text{bit} = 8\text{byte}$ and with a memory size of 1 GB that limits the size to be $N_k = 11180$ for a 2 dimensional material, and with N_k scaling as the squareroot of the available memory

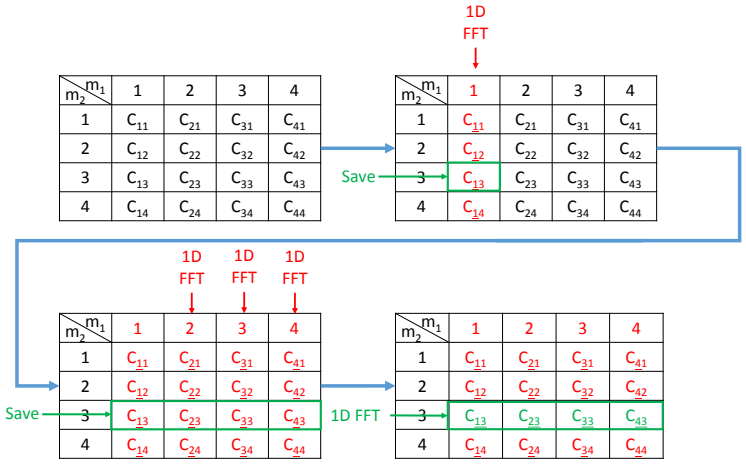

FIGURE 7.1: Schematic of sequential fourier approach. Red components are partially transformed. Green components are fully transformed. The m_i's refer to the Fourier coefficient in the i'th dimension, either before or after transformation. In k-space (before transformation) it will be the index of the sampled k_i, where as in real-space (after transformation), it will be the separation in terms of lattice vectors.

that leaves high memory machines with 64GB with only capacity to an 8 times higher sampling rate. Of course this matrix is not the only thing in the memory, and with other matrix operations having to be done, and the results also needing storage the actual memory requirement will typically be aound 5 times higher in total putting a stark limitation of the available N_k. For a 3-dimensional material this limitation is much stricter as N_k only scales as the cube root of the memory size.

Further optimisation can be made making use of standard symmetries that are can be present for multi dimensional periodic materials, meaning several Green's function elements can be identical, reducing the complete solution space. This is especially relevant when using the sequential Fourier technique described below.

7.2.2 Sequential Fourier transforms

There does exist a method of trading speed of calculation for smaller memory requirements. This is done by doing the full n-dimensional transform as a series of 1-dimensional Fourier transforms. The n-dimensional Fourier components can be written as

$$\mathbf{G}(m_1\mathbf{a}_1, ..., m_n\mathbf{a}_n) = \sum_{\mathbf{k}_1,...,\mathbf{k}_n} e^{i(m_1\mathbf{a}_1\cdot\mathbf{k}_1+...+m_n\mathbf{a}_n\cdot\mathbf{k}_n)}\mathbf{G}(\mathbf{k}_1, ..., \mathbf{k}_n). \tag{7.5}$$

We can introduce the partially transformed Green's functions,

$$\mathbf{G}(\mathbf{k}_1, ..., m_j\mathbf{a}_j, ...,k_n) = \sum_{\mathbf{k}_j} e^{i(m_j\mathbf{a}_j\cdot\mathbf{k}_j)}\mathbf{G}(\mathbf{k}_1, ..., \mathbf{k}_n) \tag{7.6}$$

which remains a function of the other k's for each value of r_j. We can use a 1-dimensional FFT to obtain the partially transformed Green's functions for each set of $(k_1, ..., k_{j-1}, k_{j+1}, ..., k_n)$. Then save only the the component $\mathbf{r}_j$ that we are interested in we reduce the problem to an $(n-1)$-dimensional Fourier transform. Thus

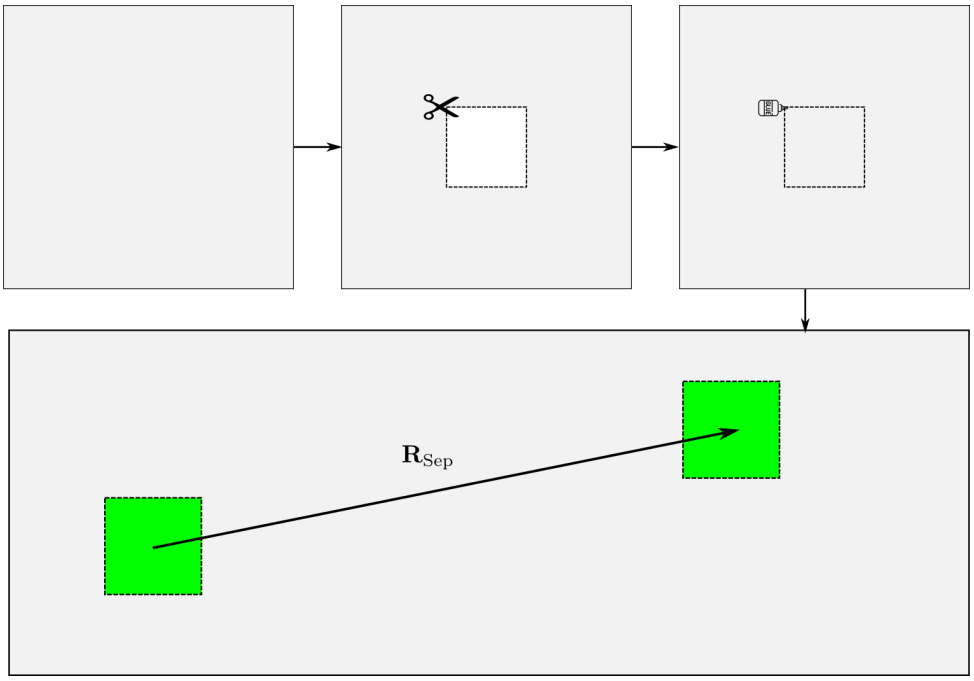

FIGURE 7.2: Schematic of benchmark method

we reduce the memory size of the problem by a factor of N_k but in order to get the same information out we need to perform $(N_k)^n$ 1-dimensional FFT and N_k, $(N-1)$-dimensional FFTs and hence it drastically increases the number of operations needed. However the dimensionallity of the problem will only be 2 or 3, and the increase of operations will be managable if one of the optimal numbers is used for N_k, and we can increase N_k beyond the limitations caused by memory constraints. A schematic for the 2-dimensional case is shown in figure 7.1.

7.2.3 Advantages of FFT

Here we have touch on some of the advantages that FFTs have over direct numerical intergration

- FFTs calculate *many* Fourier components at once.
- FFTs automatically filters out results with aliasing.

The first point is important because it, together with the efficiency of FFT algorithms, massively reduces computational time. The second point is important because very erronous results can come out of calculations with aliasing in the the Green's functions leading to artefacts in the physical properties that are calculated. Such problems can be difficult to catch if using a "black box" numerical integration method which selects k-grids based on different criteria.

7.3 Convergence

One problem with convergence using patching methods, is that the relevant accuracy of the Green's functions is very dependent on the physical quantity that is calculated. Ideally one would want to go to so high sampling rates that the Green's functions themselves are converged, but such accuracy is not necessarily required.

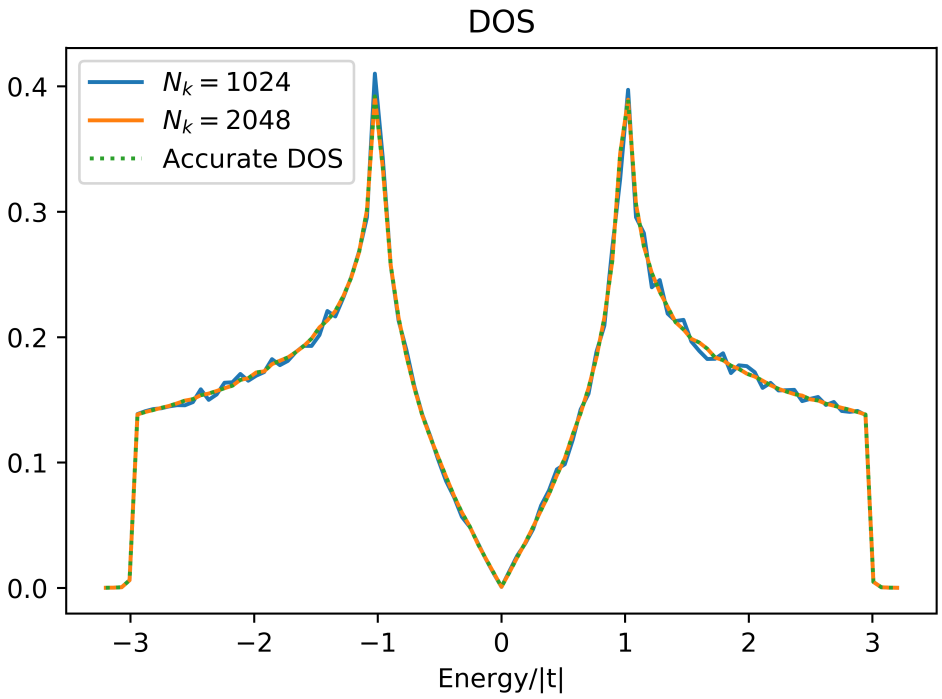

FIGURE 7.3: Graphene DOS found using FFT patching method with separation $m = n = 5$, for different accuracy in k-space. The orange line is indistinguishable from the DOS calculated directly from the periodic Green's function, and we will consider that converged.

Using the FFT method we will use the following benchmarking procedure in order to show this difference in convergence criterea. The idea is to decouple two unit cells separated by some periodicity vector $\mathbf{R}_{\text{Sep}} = (m_1\mathbf{a}_1, ..., m_n\mathbf{a}_n)$ and recouple them back to system using patching methods. A schematic of the method is shown in figure 7.2. By removing two full unit cells we get all the relevant possible combinations of start and finish sites.

We then calculate the Fourier transform and study parts of the spectral function for this separation and their convergence in k-space. The off diagonal parts will be relevant when considering transmission, bondcurrents and other scattering properties, and the diagonal parts for the density of states.

7.4 Graphene example

Here we use 1NN tight binding model graphene to show an example of the benchmarking method. In the case of graphene the extra symmetries let us get away with removing single atoms instead of full unit cells and still obtain the same information

The task is to remove two atoms on the same sublattice (sublattice B) separated some $\mathbf{R} = (m\mathbf{a}_1, n\mathbf{a}_2)$ from the graphene grid using equation (2.47), and then reintroduce them using the patching self-energy (eq. (2.43)), and study the effect on the spectral functions and how quickly they converge.

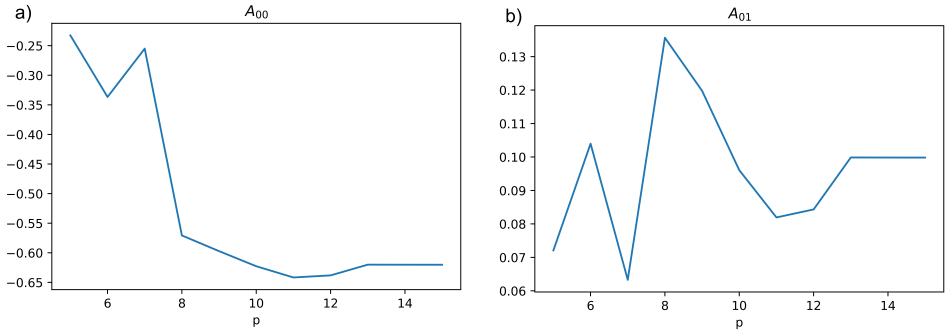

FIGURE 7.4: Convergence of graphene spectral function elements for $E = 1.5|t|$ found using FFT patching method with separation $m = n = 5$. The x-axis is indexed using p, where $N_k = 2^p$. The energy is chosen so that the DOS was not yet converged for $N_k = 1024$ in that point.

In this case we can write down the relevant Green's functions and coupling matrices explicitly, as

$$\mathbf{G}_{BB} = \begin{bmatrix} \mathbf{G}^{BB}_{0,0} & \mathbf{G}^{BB}_{1,0} & \mathbf{G}^{BB}_{0,1} & \mathbf{G}^{BB}_{m,n} & \mathbf{G}^{BB}_{m+1,n} & \mathbf{G}^{BB}_{m,n+1} \\ \mathbf{G}^{BB}_{-1,0} & \mathbf{G}^{BB}_{0,0} & \mathbf{G}^{BB}_{-1,1} & \mathbf{G}^{BB}_{m-1,n} & \mathbf{G}^{BB}_{m,n} & \mathbf{G}^{BB}_{m-1,n+1} \\ \mathbf{G}^{BB}_{0,-1} & \mathbf{G}^{BB}_{1,-1} & \mathbf{G}^{BB}_{0,0} & \mathbf{G}^{BB}_{m,n-1} & \mathbf{G}^{BB}_{m+1,n-1} & \mathbf{G}^{BB}_{m,n} \\ \mathbf{G}^{BB}_{-m,-n} & \mathbf{G}^{BB}_{-m+1,-n} & \mathbf{G}^{BB}_{-m,-n+1} & \mathbf{G}^{BB}_{0,0} & \mathbf{G}^{BB}_{1,0} & \mathbf{G}^{BB}_{0,1} \\ \mathbf{G}^{BB}_{-m-1,-n} & \mathbf{G}^{BB}_{-m,-n} & \mathbf{G}^{BB}_{-m-1,-n+1} & \mathbf{G}^{BB}_{-1,0} & \mathbf{G}^{BB}_{0,0} & \mathbf{G}^{BB}_{-1,1} \\ \mathbf{G}^{BB}_{-m,-n-1} & \mathbf{G}^{BB}_{-m+1,-n-1} & \mathbf{G}^{BB}_{-m,-n} & \mathbf{G}^{BB}_{0,-1} & \mathbf{G}^{BB}_{1,-1} & \mathbf{G}^{BB}_{0,0} \end{bmatrix} \tag{7.7}$$

$$\mathbf{G}_{PB} = \begin{bmatrix} \mathbf{G}^{BA}_{0,0} & \mathbf{G}^{BA}_{1,0} & \mathbf{G}^{BA}_{0,1} & \mathbf{G}^{BA}_{m,n} & \mathbf{G}^{BA}_{m+1,n} & \mathbf{G}^{BA}_{m,n+1} \\ \mathbf{G}^{BA}_{-m,-n} & \mathbf{G}^{BA}_{-m+1,-n} & \mathbf{G}^{BA}_{-m,-n+1} & \mathbf{G}^{BA}_{0,0} & \mathbf{G}^{BA}_{1,0} & \mathbf{G}^{BA}_{0,1} \end{bmatrix} \tag{7.8}$$

$$\mathbf{V}_{BP} = \begin{bmatrix} t & 0 \\ t & 0 \\ t & 0 \\ 0 & t \\ 0 & t \\ 0 & t \end{bmatrix}, \tag{7.9}$$

where we have used the more compact notation of $\mathbf{G}^{s_1 s_2}_{m,n}$, s_i, being the sublattice indices.

We use the analytical expression for the 1NN Green's function (equation (3.21)), to sample the Green's function in k-space. We use a regular N_k by N_k grid where $N_k = 2^p$ and p is a positive integer. We then calculate the spectral function for the device (a 2x2 matrix) a check the convergence as a function of N_k.

In order to have a familiar physical quantity to compare we study the DOS as it converges as a function of energy which is plotted in figure 7.3 run with the 2 dimensional inverse FFT. In figure 7.4 we plot examples of convergence plots for both the diagonal and off diagonal elements of the spectral density. For accuracy beyond $N_k = 2^{12} = 4096$, we use sequential Fourier transforms because of memory constraints. We go up to an accuray of $N_k = 2^{15} = 32768$ as the highest number in the plot.

It is worth noting that the DOS in figure 7.3 looks converged already for $p = 11$ and that the diagonal spectral function varies very little in figure 7.4 after this

point (around 3%), whereas the off diagonal part has not yet converged (it varies by around 15%).

7.5 Summary and Conclusions

We have shown a robust method that can be used to generate the pristine sheet Green's function components between unit cells with large spatial separations, using graphene as a calculational example. As long as a method to sample the Green's function of the pristine material in k-space exists, we can build a library and improve it over time, so it can be used and reused for calculations on the same material. We have also discussed the advantages of FFT over standard numerical integration and why care should be taken when

In order to further demonstrate the viability of this method calculations without analytical expression should be tried, in order to gauge if accurate results are possible to generate converged Green's functions within a reasonable time frame.

It is worth noting that we expect that the bottleneck will not be the Fourier transforms themselves even if sequential Fourier transform are used, but rather the actual sampling of the Green's functions. This is especially true if more computationally heavy methods such as density functional theory (DFT) are used.

We do expect this method to open up the possibility to calculate a new class of systems using patching techniques, which was previously resevered to simple graphene systems in the 1NN model.

"A story has no beginning or end: arbitrarily one chooses that moment of experience from which to look back or from which to look ahead."

Graham Greene

8 Summary and outlook

The use of graphene devices with sublattice-asymmetric potential have exciting potential for future applications both within the fields of electronics and valleytronics. As shown throughout this thesis there is still much unexplored ground for these systems that can be illuminated even using simple models.

Using Green's functions methods in a tight binding model for graphene, we have been able to calculate both very local effects, such as electronic density change in the pressence of a single impurity and very large scale effects such as transmission across hundreds of nanometers. By comparing with continuum models and effective models we have been able to bridge atomistic calculations with the macroscale behaviour. These methods together have enabled us to investigate a number of interesting systems with exotic properties.

The systems investigated in this thesis have the common factor that a major symmetry, namely the unit cell inversion symmetry, is broken. The effects of this symmetry breaking have turned out to be very stable in the pressence of disorder. The two main effects we have seen due to the introduction of average Dirac mass term, has been the opening of a bandgap and a chiral split of the valleys.

We started out by considering interfaces between sublattice domains which in the continuum model was predicted to have chiral zero energy states, but in the tight binding model shows differences when the exact boundary geometry is considered. A zigzag domain wall is predicted to still have a zero energy boundary state, where as the armchair boundary states themselves are gapped. By doing an ARPES simulation we could confirm the "local bands" near the boundary to be similar to those predicted by the Dirac model at least for the zigzag boundary, whereas the armchair boundary has the bands for both valleys projected on top of each other leading to the opening of a gap.

Next we considered ribbon type geometries with disordered sublattice dependent potentials. We studied the interaction between the between edge geomteries and the predicted gap opening abilities of sublattice-asymmetry. It was already predicted that even low concentrations of substitutional nitrogen doping would lead to gapped graphene if the distribution was sublattice-asymmetric, that retains high electron mobility. We used a tight binding decription to demonstrate that the interaction with the edge geometry has a huge effect on electronic properties of ribbons,

with these sublattice-asymmetric doping profiles and we showed that the electronic properties themselves remain similar even in cases of less than perfect asymmetry.

In case of AGNRs the electronic are very similar to those of bulk graphene with a large range of energies where the electronic density of states is depleted and a corresponding gap opens in the transmission. For ZNGRs the properties are dominated by impurity states near the edges which themselves have an inbuilt sublattice-asymmetry. These states carries a quite quenched current through the ribbon for energies that for AGNRs are gapped. These effects have relevance beyond nanoribbons since much of large scale graphene growth is based on CVD leading to grain boundaries which has edge-like defects.

We also investigated domain walls for these disordered sublattice-asymmetric doping distributions, where prefered the sublattice was changes and saw the appearence of mid gap metallic states similar to those for seen for domian walls between sublattice domains in gapped graphene sheets. This leaves possible application within valleytronics for these channels as valley polarised channels that can be made experimentally.

Wanting to further our understanding of sublattice-asymmetry in graphene led us to investigating the effect of localised Dirac masses. We solved the problem of a plane wave scattering off a circular dot in the Dirac approximation, and showed that it lead to non-trivial valley specific patterns in the electronics of the scattered states. Specifically we demonstrated the existence of large angular splits of the two reflected valley currents, tunable with the use of a back gate. This allows dots of this type to function as effective mass splitters that can be turned on and off using external electronic controls.

We used a fully atomistic tight binding calculation in a dual probe setup to verify the results in the Dirac approximation. This was done using a Green's functions patching setup where the probes and the dot are patched into a pristine graphene sheet. The atomistic model showed the same local behaviour as the Dirac approximation, even in the case of smoothened or disordered mass distributions, showing the robustness of the valley specific effects of the mass dots.

As the patching method allows for local changes in otherwise pristine materials to be probed using boundary self-energies, we wanted to extend the method beyond the use in the 1NN tight binding model for graphene. In order to do so, we described a method utilising FFT algorithms to numerically calculate the Green's function matrix elements required for implementing patching methods. This provides alternative methods for calculating the effects of local disorder in periodic systems, without computational artefacts from artifical boundary conditions, and possibly much smaller system size requirements. It also opens up possibilities for calculations in systems with multiple STM probes with large separations.

8.1 Outlook

The future prospects for both electronic and valleytronic devices based on graphene with sublattice-asymmetry appears to be bright. The use of asymmetric doping to enable gapped graphene materials which retains high mobility seems to be promising with the caveat that care should be taken to avoid problems due to edges or boundaries. The topological boundary states that appears in domain walls in gapped graphene and which seems to reappear along sublattice domain boundaries for suballtice-asymmetric doping sohuld be further investigated in disordered systems, to see wether the valley polarisation is kept from the idealised case.

The possible use of localised masses has many degrees of freedom which can still be explored. In particular the interaction betweeen the mass term, the static potential term and dot size leaves a large parameter space which might have interesting resonances of which we do not yet know.

Even more interesting is the interaction between many mass dots which can be explored in large scale calculations or experimentally. If the valley effects propagate through an array of suchs mass dot, it could lead to large scale valley splitting devices, which could be the foundation of valleytronic engineering using graphene as a base material.

Finally we hope that the patching methods can be used in more widespread selection of materials and systems. Especially with the FFT formalism discribed here intersting new systems could be investigated computationally which could help bridge gaps between experiment and theory.

A Practical implementation

A large part of this ph.d. work has been efficient implementation of the models discussed in chapter 2. Both the tight binding and Dirac model implementation has many subtleties that might be missed during implmentation, where the mathematical expression do not straight forwardly translate to computer code. The most important of these will be discussed in this appendix, as well as consesions or trade-offs that have made.

A.1 Main computational resources

We start with discussing the main computational resources that we have available and where trade offs have to made.

First we have *CPU speed* and the number of logical actions performed. In general the CPU speed will be fixed, so the goal will be to minimise the number of operations to make calculation run as fast as possible, but under the constraints of the other main resources. The second resource is *memory*, which will be the most common finite constraint that we will have to work around. In general there is a cost to moving information to memory, so we want to keep as much relevant information in memory while it is needed for the calculation. The most common trade off while be speed/memory trade offs where we need to remove important variables from memory, and even save them to the disk. This introduces third main resource which is the *I/O* capacity and speed, refering to the disk read and write capabilities.

A.2 Implementing the patched tight binding model

The implementation of the tight binding model using the patching method to do dual probe spectroscopy simulation on graphene systems has many of these subtle challenges. In this section we go through some of the technical problems we faced during the implementation phase of this ph.d. work.

A.2.1 Calculating real space graphene Green's functions

We used the analytical expression from chapter 3 to calculate the pristine graphene Green's functions. In order to do the fourier transforms needed, we use numerical integration to find individual fourier components. The exact method used is C library called cubature, (`https://github.com/bnaras/cubature`), an adaptive multivariate integration over hypercubes. This method works quite well for smaller real-space seperations, but for larger seperation the fast varying nature of the Fourier terms, makes the integral convergence harder. This puts a hard limit on the maximum seperations we can calculate using this method, which due to memory limitations has a hard cap on accuracy. As an alternative on can implement the FFT algorithms where accurracy is much more dependent on the number of kpoints sampled, which is constrainted by CPU speed instead of memory. Furthermore since the pristine system remains constant a library of accurate results can be build using these techniques.

A.2.2 Storage real space graphene Green's functions

Building and storing a full library of Green's functions turned out to be a non-trivial task. We require that for each energy the library can be accesed, the relevant Green's functions extracted and any missing components should be identified, calculated and stored for future use. One simple way to do this is to save each individual Green's function component for each energy in a seperate file, sorted in a systematic way. This way the existence of the file indicates wether the component needs to be calculated or not. This method does however put a large strain on the file indexing system, as a large number of seperate small files is created, which puts a large strain on both storage capacity, and especially the I/O capacity. In order to circumvent this issue we developed (with help from ph.d. Søren Schou Gregersen) a C library that efficiently stores, sorts and searches through n-dimensional tables. This way we could instead save a single file for each energy. Since Green's functions are only needed for a single energy at the time the is optimum we reached for conserving memory. In case of very large libraries on might need to further divide the files into sections that deals with different sections of $(m, n)-$space.

A.2.3 Intermediate Green's functions

As explained in section 2.7.3 several intermediate Green's functions has to be calculated and saved. Due to the large possible cellsize a choice have to be made, namely how many cells to keep in memory. We opted for the slightly slower but stable option to save each individual Green's function for as long as they are need before deleting them from the disk again. The puts the minimal amount of data in memory at each time moving the stress to the I/O capcity instead.

A.2.4 Book-keeping

A major part of the implementation has been keeping track of individual sistes through different numbering systems. Careful consideration should be taken when deciding how to handle the different indexing of sites. First when a system is setup each site will be naturally numbered in the list of all sites. All properties of a site is associated with this number, be that position, potentials sublattice etc. When using the adaptive tridiagonalisation algorithm each site is assigned to a cell, and will have numbering within that cell. We have to make sure that we have connection

between this new numbering and the original properties, and that we keep track of these properties in an effective manner. Further division can be reqiured if we want to calculate e.g. the local k-space projections of the spectral density as was the case for the mass dot, where we also divide the sites into a rectangular grid to calculate the local Fourier transforms and thus we also have to keep track of which grid cell each site belongs to.

B
Published papers

PHYSICAL REVIEW B **93**, 035446 (2016)

Electronic transport in graphene nanoribbons with sublattice-asymmetric doping

Thomas Aktor, Antti-Pekka Jauho, and Stephen R. Power*
Center for Nanostructured Graphene (CNG), DTU Nanotech, Department of Micro- and Nanotechnology, Technical University of Denmark, DK-2800 Kongens Lyngby, Denmark
(Received 13 April 2015; revised manuscript received 7 January 2016; published 25 January 2016)

Recent experimental findings and theoretical predictions suggest that nitrogen-doped CVD-grown graphene may give rise to electronic band gaps due to impurity distributions which favor segregation on a single sublattice. Here, we demonstrate theoretically that such distributions lead to more complex behavior in the presence of edges, where geometry determines whether electrons in the sample view the impurities as a gap-opening average potential or as scatterers. Zigzag edges give rise to the latter case, and remove the electronic band gaps predicted in extended graphene samples. We predict that such behavior will give rise to leakage near grain boundaries with a similar geometry or in zigzag-edged etched devices. Furthermore, we examine the formation of one-dimensional metallic channels at interfaces between different sublattice domains, which should be observable experimentally and offer intriguing waveguiding possibilities.

DOI: 10.1103/PhysRevB.93.035446

I. INTRODUCTION

The high Fermi velocity and linear electronic dispersion in graphene appear promising for electronic devices [1]. The absence of an intrinsic band gap is a potential stumbling block for many applications. A range of possibilities is being investigated to redress this. Many involve geometric constraints in the form of, e.g., finite-width nanoribbons [graphene nanoribbons (GNRs)] [2] or periodic perforations [3]. An alternative route is the manipulation of the atomic level structure. A hexagonal graphene lattice is composed of two intersecting triangular sublattices, A and B, shown by open and solid symbols, respectively, in the top panels of Fig. 1. The equivalence of these leads to a gapless band structure. A sublattice dependent potential opens a band gap and gives mass to the charge carriers. A possible implementation is to place graphene on a substrate, such as hexagonal boron nitride (hBN), which offers a potential varying on approximately the required length scale [4]. However, the potential here is quite weak and lattice mismatches give rise to larger scale moiré features [5–7].

Recent experiments suggest another route to breaking sublattice equivalence. Nitrogen-doped graphene grown by chemical vapor deposition (CVD) can show unusual distributions of substitutional N atoms. Large domains are found with N atoms primarily occupying a single sublattice [8–12]. This behavior depends on growth conditions, and theoretical works suggest possible mechanisms including preferential impurity positioning relative to the edges during growth [13] and interimpurity interactions in disordered ensembles [14,15]. Subsequent studies of N-doped graphene treated by high-temperature annealing [16], and of graphene decorated by hydrogen adatoms [17], suggest that asymmetric distributions may also arise in other scenarios. Such doping leads to different average potentials on each sublattice and is equivalent to introducing an effective mass term. Extended graphene sheets with sublattice-asymmetric impurity distributions are predicted to display electronic and transport band gaps, and electron-hole asymmetry in their conductivity [18–22].

In this paper we focus on nanoribbons with sublattice-asymmetric doping. This is motivated both by the possibility of etching [23] and transferring [24] devices from doped graphene sheets and by the need to understand the interplay between the effective mass term introduced by such doping and effects induced by symmetry-breaking edges. This is important since CVD-grown graphene contains extended edgelike defects in the form of grain boundaries [25–28], unlike bottom-up approaches which may allow the synthesis of more precise geometries [29]. We are further motivated by the strong dependence of GNR transport on edge geometry and impurity distribution [30–43] and by sublattice dependent features in carbon nanotubes [44,45]. We consider both armchair- (AGNR) and zigzag- (ZGNR) edged ribbons, noting the in-built sublattice asymmetry of ZGNRs due to sites along one edge belonging to one sublattice. Similar behavior to bulk graphene is found for AGNRs—namely, reliable electronic and transport band gaps consistent with an average mass term model. For ZGNRs, only a suppression of transmission is found in the expected gap region and it is not accompanied by a vanishing density of states (DOS). In particular, strong finite DOS clusters remain along one ZGNR edge. This is related to the position dependence of simple impurity bound states near zigzag edges and is captured within a coherent potential approximation (CPA) model. Finally, we investigate interfaces between different sublattice domains and predict that these should give rise to robust one-dimensional metallic wires embedded within the gapped system, and which should have features detectable by scanning tunneling microscopy (STM).

II. MODELS

The electronic structure of graphene is well described by a nearest-neighbor tight-binding Hamiltonian with a hopping integral $t = -2.7$ eV. The use of this model is validated in the Appendix, where key features from our results are reproduced using a higher-order model. We take $|t|$ as the unit of energy and include substitutional N dopants by a change of on-site energy $\Delta = -|t|$. More accurate parametrizations can be achieved [22,46,47], but the qualitative behavior

*spow@nanotech.dtu.dk

described here is reasonably independent of impurity species or parametrization. We will discuss the change in carrier density induced by such dopants at the end of Sec. III below. A general band dispersion is given by

$$\epsilon_{\pm}(\mathbf{k}) = \tfrac{1}{2}(\epsilon_A + \epsilon_B) \pm \tfrac{1}{2}\sqrt{(\epsilon_A - \epsilon_B)^2 + 4t^2|f(\mathbf{k})|^2}, \quad (1)$$

where ϵ_A (ϵ_B) is the potential on the A (B) sublattice and $f(\mathbf{k})$ is a term arising from the sum of Bloch phases over neighboring sites. For pristine graphene, $\epsilon_A = \epsilon_B = 0.0$, and so $\epsilon_{\pm}(\mathbf{k}) = \pm t|f(\mathbf{k})|$, which is gapless near $E = 0$. Uniformly breaking the sublattice symmetry, by setting $\epsilon_A \neq \epsilon_B$, has three effects on the band structure: (i) a band-center shift of $\frac{\epsilon_A+\epsilon_B}{2}$, (ii) a direct band gap of magnitude $|\epsilon_A - \epsilon_B|$ at the Dirac points, and (iii) the breaking of the band linearity due to the additive constant $(\epsilon_A - \epsilon_B)^2$ in the square root. The quantity $\frac{|\epsilon_A-\epsilon_B|}{2}$ is called a *mass* term, and the dispersion of electrons in the gapped systems is no longer linear or massless.

Transport quantities are calculated using recursive Green's function (GF) techniques [48]. Semi-infinite leads are constructed using an efficient decimation procedure [49] and the zero-temperature conductance is given by [50] $G = \frac{2e^2}{h}T$, where the transmission is calculated from $T(E) = \mathrm{Tr}[\mathbf{G}^r\Gamma_R\mathbf{G}^a\Gamma_L]$, where $\Gamma_i(E)$ $(i = L, R)$ are the level width matrices and $\mathbf{G}^{r/a}(E)$ is the retarded/advanced Green's function of the device region. A configurational average is taken for disordered systems to discern the overall trends. We also examine the local density of states (LDOS), which at site i is given by $\rho_i(E_F) = -\frac{1}{\pi}\mathrm{Im}[G^r_{ii}(E_F)]$. The GFs required here involve a double sweep through the device region [48].

Effective medium models are used to analyze the configurationally averaged densities of states. The use of the two different models below allows one to isolate effects arising from an average disorder-induced potential or mass term, and the effects of scattering from individual impurities. Both models employ a first-nearest-neighbor (1NN) tight-binding description which is perfectly periodic along the ribbon direction. On-site energies within the repeated unit cell are determined as described below. The *virtual crystal approximation* (VCA) ignores scattering effects and simply takes into account the new average potential felt by electrons. In practice, this is done by introducing a self-energy to shift on-site energies by $c\Delta$, where c is the doping concentration and Δ is the shift caused by a single dopant [51]. For sublattice dependent doping, this is generalized so that the self-energy is sublattice dependent, $\Sigma_x = c_x\Delta_x$ for $x = A, B$, due to c_x (and/or Δ_x) taking different values on each sublattice. This new unit cell is then considered part of an infinite perfectly periodic *virtual crystal* allowing us to calculate the Green's function and thus the density of states. The *coherent potential approximation* (CPA) replaces this potential with a position and energy dependent self-energy to include simple scattering effects. This self-energy is found from the solution of the self-consistent equation $\Sigma_x = c_x\Delta_x(1 - (\Delta_x - \Sigma_x)G_{\mathrm{eff}})^{-1}$, where G_{eff} is the Green's function of the new effective medium [51,52]. Periodicity of the effective medium along the ribbon direction can again be used to quickly calculate the Green's function and density of states. It can be shown that the CPA includes simple scattering effects, but neglects higher-order scattering terms. In this way features appearing in the CPA, but not the VCA, arise due to the scattering effects beyond an average potential but below higher-order cluster effects, such as localization.

III. RESULTS AND DISCUSSION

We first calculate the transmission through both GNR types for two disorder types—a completely random distribution of impurities over all sites (*symmetric*) or a distribution confined to only one sublattice (*asymmetric*). Figure 1 shows transmissions through 101-AGNR (width ∼12 nm) [Fig. 1(a)] and 100-ZGNR (width ∼21 nm) [Fig. 1(b)] systems. In the absence of disorder, these ribbons are both metallic within the nearest-neighbor tight-binding approximation. Results for the initially semiconducting 100-AGNR are shown in the Appendix.

The conductance of the pristine systems is shown by the gray shaded areas and the averaged asymmetrically (symmetrically) doped systems by solid red (dashed blue)

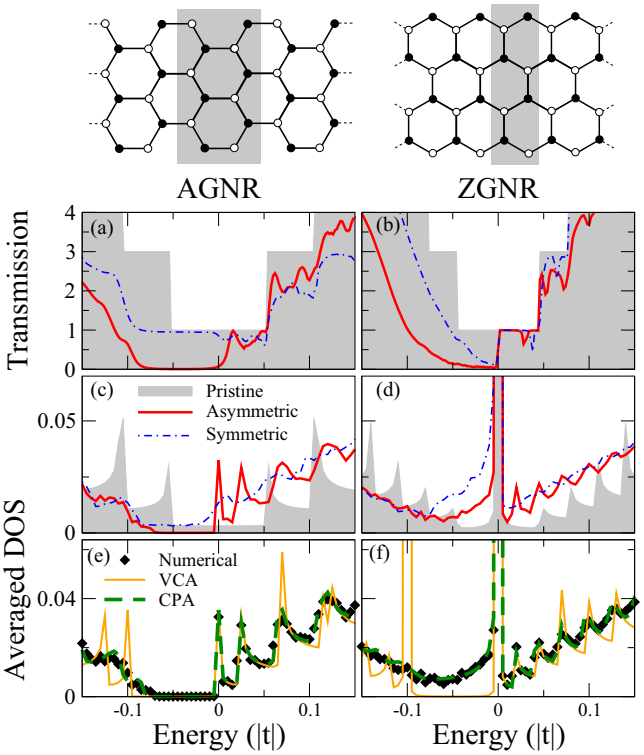

FIG. 1. Top: Schematics of a 6-AGNR and 4-ZGNR, with the unit cells shown by the shaded areas and the A (B) sublattice sites by open (solid) symbols. The index counts the dimer lines or zigzag chains across the ribbon. The remaining panels show results for a 101-AGNR (left) and a 100-ZGNR (right). (a) and (b) show the (averaged) transmission through pristine systems (gray shading) and also systems with 40 unit cells of sublattice-asymmetric (solid red lines) and sublattice-symmetric disorder (blue dashed-dotted line). (c) and (d) show the numerically averaged DOS of longer systems with corresponding disorder profiles. (e) and (f) show the numerically averaged DOS for the fully asymmetric case (black symbols) compared to VCA (orange) and CPA (green, dashed) model calculations. The concentration of N atoms for all disordered cases is 5%.

lines. Configurational averages over 100 instances of disorder through device regions 40 unit cells long (17 nm for AGNR, 10 nm for ZGNR) are shown. Impurity concentrations are $c_A = 0.05, c_B = 0.05$ ($c_A = 0.1, c_B = 0.0$) for the symmetric (asymmetric) cases, where $c_{A/B}$ is the concentration on a given sublattice. Note that the asymmetric case corresponds to a random replacement of 10% of sublattice A carbon atoms with nitrogen atoms within the disordered region, for a total nitrogen concentration of 5% as the B sublattice is unaltered. The total concentration of nitrogen is thus the same for both cases.

For AGNRs, asymmetric disorder opens a band gap with sharp edges on the hole side of the spectrum, in contrast to symmetric disorder where very little transmission suppression is seen. The persistence of the $T = 1$ plateau in the symmetric case has been observed previously [34]. In general, AGNRs are more sensitive to edge disorders than the bulk substitutional disorder considered here [31,41]. The transport gap for asymmetric doping has a corresponding electronic band gap, clearly visible in the averaged DOS plot in Fig. 1(c). This shows an average over the central 800 cells of a disordered region with a total length of 1000 unit cells. The appearance of this band gap is consistent with the results for similarly doped extended graphene sheets [22]. A comparison of the numerically averaged DOS to results from the VCA and CPA models is shown for the fully asymmetric case in Fig. 1(e). Good agreement between the VCA and numerical results is seen within the gap and on the electron side, while poor agreement is seen on the hole side. The VCA also overestimates the band gap, which is somewhat smaller than the value $c_A\Delta = 0.1|t|$ given by a uniform mass term. These discrepancies are almost entirely corrected by the CPA, where excellent agreement is seen over the entire energy range.

The accuracy of the VCA at the gap and electron-side energies suggests that the main effect of disorder here is not scattering, but rather an averaged potential landscape with a sublattice dependent mass term. The unimportance of scattering effects here is also apparent in the transmission shown in Fig. 1(a), where the asymmetric disorder only induces minor quenching of transmission at these energies. Conversely, the failure of the VCA and success of the CPA on the hole side suggest that scattering plays a more important role here. This is further evidenced by the hole-side transmission, which is significantly reduced relative to the pristine case and has its plateau features almost completely smeared out. This electron-hole asymmetry is consistent with results in graphene sheets, where reduced mobility on the hole side is associated with a pseudospin polarization giving a higher occupation of the undoped (doped) sublattice on the electron (hole) side [22]. We have confirmed that this feature is also present in the AGNR case by examining the sublattice dependent averaged DOS. The reduced gap size compared to the VCA prediction is in line with a sublinear gap dependence found in graphene sheets [18,22]. We have varied the concentration and find agreement with the $E_G \sim c_A^{0.75}$ scaling previously reported [22].

The right-hand side panels of Fig. 1 show that many of the features discussed above are radically altered for zigzag-edged systems. Transmission suppression is observed in the gap region for asymmetric doping in Fig. 1(b), but without

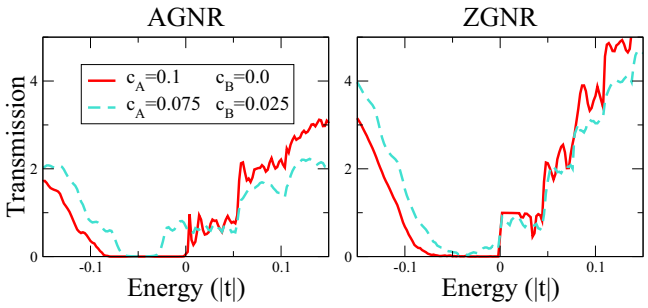

FIG. 2. Transmissions for 101-AGNR (left) and 100-ZGNR systems with 80 unit cells of asymmetric disorder. Results are shown for both fully (red, solid) and partially (turquoise, dashed) asymmetric distributions of impurities.

sharply defined band-gap edges. Furthermore, a significant DOS is noted throughout the expected band gap [Fig. 1(d)]. It is thus unsurprising that the VCA [Fig. 1(f)] fails to capture the DOS features at these energies, since this model always gives a band gap. However, it does capture the low-energy electron-side behavior quite well, including the sharp peak at $E = 0$. This peak is associated with states localized on the edge atoms of a ZGNR. It is doubly degenerate in pristine ribbons, as the states on each ribbon edge, although belonging to opposite sublattices, are equivalent. Adding a uniform mass term breaks this degeneracy and the peak splits into two, which reside at the band-gap edges, at energies corresponding to the on sites of each sublattice. This is seen for the VCA result, but the peak at $E = -0.1|t|$, associated with the N-doped sublattice, is absent in the numerical results and only the undoped sublattice peak remains. The CPA once again restores the features absent within the VCA, suggesting that the finite DOS in the expected band gap is due to scattering processes dominating over a gap-opening average potential.

To verify the robustness of the gap-opening feature, we consider the case of less than perfect sublattice asymmetry. Figure 2 shows the transmissions through systems analogous to those in Figs. 1(a) and 1(b), but with 75% of N atoms on sublattice A and 25% on sublattice B. Curves for a fully asymmetric case are shown for comparison. For partial asymmetry, we note a clear band-gap formation for the AGNR case, whereas transmission suppression without a clear band gap is still present for the ZGNR case. The AGNR band gap is shifted away from $E = 0$, unlike that of the perfectly asymmetric case, as the band-center shift and mass terms entering in Eq. (1) are no longer equal. Band-gap formation at this level of asymmetry is promising for realizing such a gap experimentally, as samples with over 90% asymmetry have been reported [11].

To further explore the differences between armchair- and zigzag-edged geometries, we show LDOS maps for a single, fully asymmetric disorder configuration of each in Fig. 3. The maps are taken at an energy in the middle of the expected band gap. The LDOS decays quickly as we move into the disordered region of an AGNR. This decay is also uniform across the ribbon width. For the ZGNR, the LDOS vanishes throughout most of the system. However, large clusters of finite density remain along the bottom edge of the ribbon,

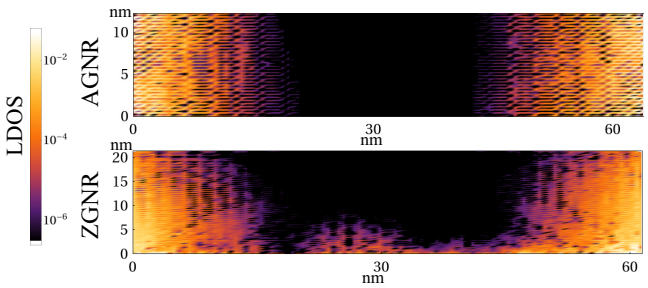

FIG. 3. LDOS maps of a disordered 101-AGNR (top) and 100-ZGNR (bottom) at $E = -0.04|t|$. The impurities are entirely on the A sublattice, corresponding to the bottom edge of the ZGNR, where a nonvanishing DOS is evident.

which is associated with the doped sublattice. This suggests an interplay between the doping of a particular sublattice and the proximity of a zigzag edge of the same sublattice. The reproduction of averaged DOS features within the CPA model suggests that this effect can be explained in terms of single scattering processes, and so we now examine individual N dopants in a ZGNR.

Figure 4(a) shows a few possible sites for a single N atom near the edge of a 50-ZGNR. The sites represented by red and green circles are on the edge sublattice, whereas the blue site is not. Figures 4(b) and 4(c) show that impurity sites on the edge sublattice give rise to conductance dips and corresponding DOS peaks in the low-energy window shown here. These features, associated with antiresonances formed by the impurity, have been studied previously in GNRs [30,41]. Symmetry-breaking edges result in a strong position dependence of the antiresonance energies. Interestingly, sites near a ZGNR edge and of the same sublattice type can give rise to features at energies within the expected band gap, whereas those on the opposite sublattice (and sites in AGNRs) result in features at energies far outside this window. In Figs. 4(d)–4(f) the change in LDOS near three of these sites is mapped. For Figs. 4(d) and 4(f), corresponding to sites on the edge sublattice, we

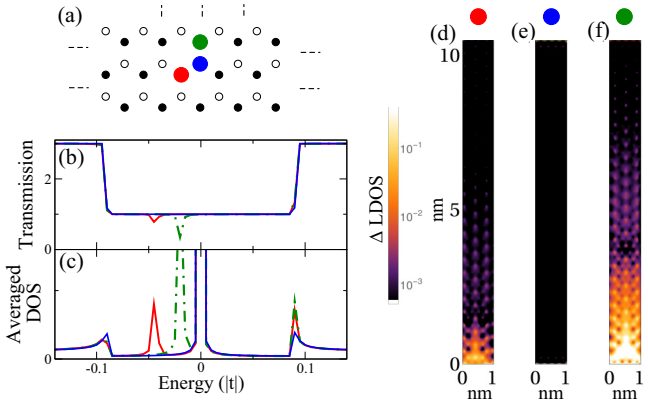

FIG. 4. The transmission (b) and averaged DOS (c) for a 50-ZGNR with a single N impurity located at each of the sites shown by the symbol of the same color in (a). (d)–(f) map the change in LDOS near the three possible impurity locations, taken at (d) $E = -0.05|t|$ and (e), (f) $E = -0.02|t|$.

choose the DOS peak energy and note a significant triangular region of increased DOS near the impurity locations at the bottom edge. For the opposite-sublattice impurity site in Fig. 4(e), we choose the same energy as Fig. 4(f), and note that no such feature is visible and the DOS barely differs from that of a pristine ribbon. Consequently, electrons in this energy range are scattered by impurities located on the same sublattice as the edge, and not by those on the opposite sublattice. Returning to asymmetrically disordered ZGNRs, we can understand the finite DOS in the expected band gap [Fig. 1(d)] as the average of many single impurity peaks at different energies and corresponding to A-sublattice impurities at different locations near the bottom edge. Away from this edge, the density of states vanishes, as shown in Fig. 3, because the net effect of the doping here is an average mass term and not scattering from impurity states. This is confirmed further by examining the position dependence of the CPA self-energy Σ_A, which in AGNRs takes a real and quite uniform value slightly smaller than $c_A\Delta$. This is also true across much of a ZGNR, except near the edge associated with the doped sublattice, where Σ_A becomes complex and its real part varies drastically from $c_A\Delta$. The VCA is unable to explain behavior near this edge, as the net effect of the doping is no longer an effective mass term. Increasing the device length will lead to a transport gap as we enter the localization regime. However, this gap is unrelated to the effective mass term or a DOS gap, and is similar to the behavior observed for ZGNRs with symmetric doping.

The breakdown of the band gap in asymmetrically doped graphene near a zigzag edge may have interesting consequences beyond GNR devices. Grain boundaries can have geometries similar to zigzag edges and break the lattice symmetry in the same manner [25]. Thus CVD-grown systems may experience leakage near these boundaries. Another relevant interface is that between neighboring regions with doping on opposite sublattices. These have been mapped experimentally [11], and in Fig. 5 we consider an AGNR with a sublattice interface running parallel to the edge so that only the A (B) sublattice is doped in the bottom (top) of the device. Near the boundary the average mass term switches sign, closing the band gap and resulting in states confined near the interface [53]. This is confirmed in the LDOS maps in Fig. 5, shown for systems with both *sudden* [Fig. 5(a)] and *gradual* [Fig. 5(b)] interfaces where the impurity concentration changes linearly from one sublattice to the other over 4 or 20 atoms, respectively. In both cases we note a large, finite DOS running along the interface and decaying away from it. Furthermore, this regions acts as a propagating channel, as is clear from Fig. 5(c), where a finite transmission is noted across the band-gap region of a single domain device.

Electron doping by nitrogen impurities shifts the Fermi energy E_F relative to any gap. Accessing the gap region experimentally will involve the application of a gate voltage. While accurate electron counting can be performed within density functional theory (DFT) calculations [22] for single impurities or small disordered regions, this is not feasible for the system sizes considered here or in experiment. Nonetheless, the charge density fluctuation can be approximated from $\delta n \sim \frac{E_D(c_A+c_B)\rho_C}{2}$, where $E_D \approx 0.4$ is the average doping efficiency of nitrogen in GNRs [47] and ρ_C is the density of lattice sites in

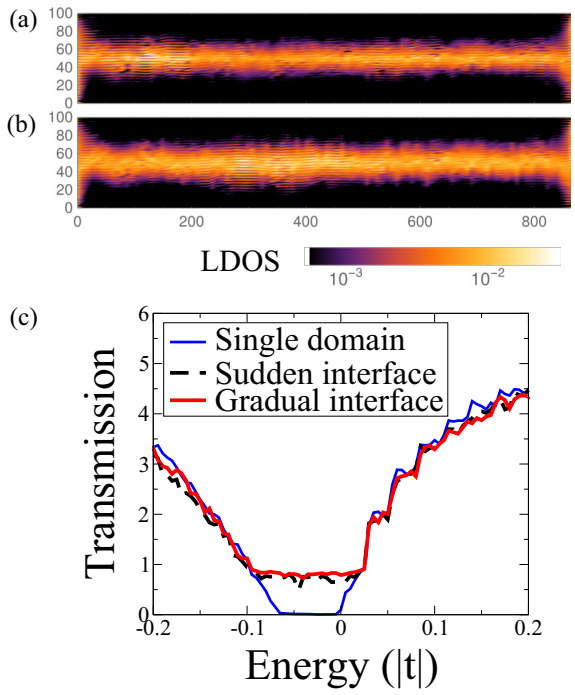

FIG. 5. LDOS maps of asymmetrically doped 200-AGNRs with (a) sudden or (b) gradual sublattice interfaces running along the center of the ribbon, taken at $E = -0.04|t|$. (c) shows the transmissions for these systems compared to one with a single domain.

graphene. For $c_A = 0.1$, we find $\delta n \sim 7.6 \times 10^{13}$ cm^{-2}, just inside the range of the most advanced gating methods [54]. $c_A = 0.02$ gives a more realistic $\delta n \sim 1.5 \times 10^{13}$ cm^{-2}, while yielding $E_G \sim$ 50–200 meV. Gaps from lower concentrations, while too small for applications, still allow experimental verification of our results. It is also possible to shift E_F nearer the gap by codoping with a symmetrically distributed p dopant, at the cost of reducing transmission outside the band gap.

IV. CONCLUSIONS

Our results highlight the importance of edge geometry in doped graphene nanoribbons. The band gap predicted for sublattice asymmetrically doped graphene is sensitive to the presence of zigzag edges, where a gap-opening average potential is no longer the dominant effect of disorder. Instead, impurity bound states within the expected band gap, associated with the edge sublattice, lead to a finite DOS and propagation, albeit scattered, along the edge. A band-gap opening, similar to that in graphene sheets, is observed for armchair edges. The sensitivity of gap opening to edge geometry is relevant beyond ribbon devices. The majority of samples with sublattice-asymmetric disorder are grown by CVD, which gives rise to edgelike defects in the form of grain boundaries. Since these can have zigzag-edge-like symmetries, we expect similar leakage near grain boundaries in asymmetrically doped polycrystalline graphene sheets. This may make it difficult to verify experimentally the band gaps predicted for such systems. Finally, we show the formation of one-dimensional metallic wire behavior at the interface between two regions with doping on opposite sublattices. Such interfaces are present in experimental systems, and the features we predict should be observable to STM measurements. These channels present waveguiding possibilities as, away from defects or edges, leakage is prevented by the gapped region surrounding them.

ACKNOWLEDGMENTS

The Center for Nanostructured Graphene (CNG) is sponsored by the Danish National Research Foundation, Project DNRF103. The authors would like to thank Søren Schou Gregersen for useful discussions during the review process.

APPENDIX: COMPARISON OF FIRST- AND THIRD-NEAREST-NEIGHBOR TIGHT-BINDING RESULTS

To check the validity of the first-nearest-neighbor tight-binding approximation (1NN) for our systems, we compare the transmissions of pristine and asymmetrically disordered nanoribbons calculated with both this model, and with a more complete third-nearest-neighbor (3NN) description of graphene. (See Fig. 6.) We also consider a 100-AGNR which is semiconducting within a 1NN description in the absence of dopants. The 1NN results are based on the system in Figs. 1(a) and 1(b), where a constant value of $t = -2.7$ eV is used throughout the system to describe the hopping parameter between nearest-neighbor sites. The 3NN results are calculated using the same relative second- and third-neighbor hoppings for pristine graphene as in Ref. [22]. For both models, we use a simple on-site shift of $\Delta = -|t|$ to represent an impurity. Larger values of Δ, suggested elsewhere in the literature [22,46] for nitrogen, would enhance the features discussed in this work due to the scaling of the effective mass term with scatterer strength.

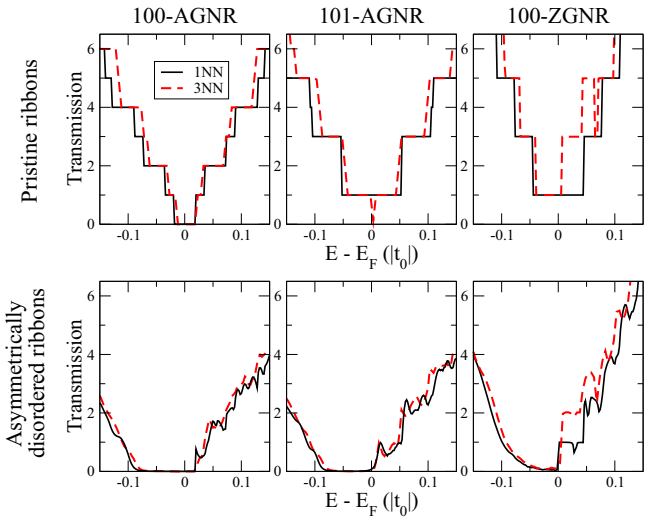

FIG. 6. Transmissions for pristine (top) and asymmetrically disordered (bottom) ribbons using both 1NN (solid, black curves) and 3NN (red, dashed curves) models. The 1NN results for the 101-AGNR and 100-ZGNR are reproduced from the main text, whereas the 100-AGNR case represents an initially semiconducting ribbon within the 1NN model.

For AGNRs we note that the 1NN model captures all the main features, with the exception of the previously reported small band gap for pristine 101-AGNRs. We also note the band-gap opening induced by asymmetric disorder occurs regardless of the metallic or semiconducting nature of the corresponding pristine ribbon. The higher transmission values for pristine ZGNRs at low electron-side energies are due to the zero-energy peak no longer remaining dispersionless within the 3NN model. This has been reported previously in the literature [38]. We note that the key result discussed in our paper, namely, the band-gap opening or transmission suppression at low hole-side energies in asymmetrically doped systems, are perfectly described by the 1NN model.

[1] A. H. Castro Neto, F. Guinea, N. M. R. Peres, K. S. Novoselov, and A. K. Geim, Rev. Mod. Phys. **81**, 109 (2009).

[2] Y.-W. Son, M. L. Cohen, and S. G. Louie, Phys. Rev. Lett. **97**, 216803 (2006).

[3] T. G. Pedersen, C. Flindt, J. Pedersen, N. A. Mortensen, A.-P. Jauho, and K. Pedersen, Phys. Rev. Lett. **100**, 136804 (2008).

[4] G. Giovannetti, P. A. Khomyakov, G. Brocks, P. J. Kelly, and J. van den Brink, Phys. Rev. B **76**, 073103 (2007).

[5] M. Bokdam, T. Amlaki, G. Brocks, and P. J. Kelly, Phys. Rev. B **89**, 201404 (2014).

[6] C. R. Woods, L. Britnell, A. Eckmann, R. S. Ma, J. C. Lu, H. M. Guo, X. Lin, G. L. Yu, Y. Cao, R. V. Gorbachev, A. V. Kretinin, J. Park, L. A. Ponomarenko, M. I. Katsnelson, Y. N. Gornostyrev, K. Watanabe, T. Taniguchi, C. Casiraghi, H.-J. Gao, A. K. Geim, and K. S. Novoselov, Nat. Phys. **10**, 451 (2014).

[7] J. Jung, A. M. DaSilva, A. H. MacDonald, and S. Adam, Nat. Commun. **6**, 6308 (2015).

[8] L. Zhao, R. He, K. T. Rim, T. Schiros, K. S. Kim, H. Zhou, C. Gutiérrez, S. Chockalingam, C. J. Arguello, L. Pálová *et al.*, Science **333**, 999 (2011).

[9] R. Lv, Q. Li, A. R. Botello-Méndez, T. Hayashi, B. Wang, A. Berkdemir, Q. Hao, A. L. Elías, R. Cruz-Silva, H. R. Gutiérrez *et al.*, Sci. Rep. **2**, 586 (2012).

[10] L. Zhao, M. Levendorf, S. Goncher, T. Schiros, L. Palova, A. Zabet-Khosousi, K. T. Rim, C. Gutierrez, D. Nordlund, C. Jaye *et al.*, Nano Lett. **13**, 4659 (2013).

[11] A. Zabet-Khosousi, L. Zhao, L. Palova, M. S. Hybertsen, D. R. Reichman, A. N. Pasupathy, and G. W. Flynn, J. Am. Chem. Soc. **136**, 1391 (2014).

[12] J. A. Lawlor and M. S. Ferreira, Beilstein J. Nanotechnol. **5**, 1210 (2014).

[13] I. Deretzis and A. La Magna, Phys. Rev. B **89**, 115408 (2014).

[14] J. A. Lawlor, S. R. Power, and M. S. Ferreira, Phys. Rev. B **88**, 205416 (2013).

[15] J. A. Lawlor, P. D. Gorman, S. R. Power, C. G. Bezerra, and M. S. Ferreira, Carbon **77**, 645 (2014).

[16] M. Telychko, P. Mutombo, M. Ondracek, P. Hapala, F. C. Bocquet, J. Kolorenc, M. Vondracek, P. Jelinek, and M. Svec, ACS Nano **8**, 7318 (2014).

[17] C. Lin, Y. Feng, Y. Xiao, M. Drr, X. Huang, X. Xu, R. Zhao, E. Wang, X.-Z. Li, and Z. Hu, Nano Lett. **15**, 903 (2015).

[18] V. M. Pereira, J. M. B. Lopes dos Santos, and A. H. Castro Neto, Phys. Rev. B **77**, 115109 (2008).

[19] D. A. Abanin, A. V. Shytov, and L. S. Levitov, Phys. Rev. Lett. **105**, 086802 (2010).

[20] P. M. Ostrovsky, M. Titov, S. Bera, I. V. Gornyi, and A. D. Mirlin, Phys. Rev. Lett. **105**, 266803 (2010).

[21] D. Abanin and L. Levitov, arXiv:1008.1424.

[22] A. Lherbier, A. R. Botello-Mendez, and J.-C. Charlier, Nano Lett. **13**, 1446 (2013).

[23] Y. Zhang, Z. Li, P. Kim, L. Zhang, and C. Zhou, ACS Nano **6**, 126 (2012).

[24] X. Li, Y. Zhu, W. Cai, M. Borysiak, B. Han, D. Chen, R. D. Piner, L. Colombo, and R. S. Ruoff, Nano Lett. **9**, 4359 (2009).

[25] J. Lahiri, Y. Lin, P. Bozkurt, I. I. Oleynik, and M. Batzill, Nat. Nanotechnol. **5**, 326 (2010).

[26] P. Y. Huang, C. S. Ruiz-Vargas, A. M. van der Zande, W. S. Whitney, M. P. Levendorf, J. W. Kevek, S. Garg, J. S. Alden, C. J. Hustedt, Y. Zhu *et al.*, Nature (London) **469**, 389 (2011).

[27] K. Kim, Z. Lee, W. Regan, C. Kisielowski, M. F. Crommie, and A. Zettl, ACS Nano **5**, 2142 (2011).

[28] O. V. Yazyev and Y. P. Chen, Nat. Nanotechnology **9**, 755 (2014).

[29] J. Cai, P. Ruffieux, R. Jaafar, M. Bieri, T. Braun, S. Blankenburg, M. Muoth, A. P. Seitsonen, M. Saleh, X. Feng *et al.*, Nature (London) **466**, 470 (2010).

[30] T. C. Li and S.-P. Lu, Phys. Rev. B **77**, 085408 (2008).

[31] E. R. Mucciolo, A. H. Castro Neto, and C. H. Lewenkopf, Phys. Rev. B **79**, 075407 (2009).

[32] V. A. Rigo, T. B. Martins, A. J. R. da Silva, A. Fazzio, and R. H. Miwa, Phys. Rev. B **79**, 075435 (2009).

[33] B. Biel, X. Blase, F. Triozon, and S. Roche, Phys. Rev. Lett. **102**, 096803 (2009).

[34] P. Dietl, G. Metalidis, D. Golubev, P. San-Jose, E. Prada, H. Schomerus, and G. Schön, Phys. Rev. B **79**, 195413 (2009).

[35] J. Kunstmann, C. Özdoğan, A. Quandt, and H. Fehske, Phys. Rev. B **83**, 045414 (2011).

[36] E. Cruz-Silva, Z. M. Barnett, B. G. Sumpter, and V. Meunier, Phys. Rev. B **83**, 155445 (2011).

[37] K. Saloriutta, Y. Hancock, A. Kärkkäinen, L. Kärkkäinen, M. J. Puska, and A.-P. Jauho, Phys. Rev. B **83**, 205125 (2011).

[38] P.-H. Chang and B. K. Nikolić, Phys. Rev. B **86**, 041406 (2012).

[39] J. R. Owens, E. Cruz-Silva, and V. Meunier, Nanotechnology **24**, 235701 (2013).

[40] A. R. Botello-Méndez, A. Lherbier, and J.-C. Charlier, Solid State Commun. **175**, 90 (2013).

[41] A. Orlof, J. Ruseckas, and I. V. Zozoulenko, Phys. Rev. B **88**, 125409 (2013).

[42] J. Wilhelm, M. Walz, and F. Evers, Phys. Rev. B **89**, 195406 (2014).

[43] J. Wilhelm, M. Walz, and F. Evers, Phys. Rev. B **92**, 014405 (2015).

[44] J. M. García-Lastra, K. S. Thygesen, M. Strange, and Á. Rubio, Phys. Rev. Lett. **101**, 236806 (2008).

[45] J. Lawlor and M. S. Ferreira, Phys. Rev. B **92**, 115405 (2015).

[46] T. G. Pedersen and J. G. Pedersen, Phys. Rev. B **87**, 155433 (2013).

[47] T. G. Pedersen, Phys. Rev. B **91**, 085428 (2015).

[48] C. H. Lewenkopf and E. R. Mucciolo, J. Comput. Electron. **12**, 203 (2013).
[49] M. P. L. Sancho, J. M. L. Sancho, and J. Rubio, J. Phys. F **14**, 1205 (1984).
[50] S. Datta, *Electronic Transport in Mesoscopic Systems* (Cambridge University Press, Cambridge, UK, 1997).
[51] R. J. Elliott, J. A. Krumhansl, and P. L. Leath, Rev. Mod. Phys. **46**, 465 (1974).
[52] P. Soven, Phys. Rev. **178**, 1136 (1969).
[53] G. W. Semenoff, V. Semenoff, and Fei Zhou, Phys. Rev. Lett. **101**, 087204 (2008).
[54] M. Craciun, S. Russo, M. Yamamoto, and S. Tarucha, Nano Today **6**, 42 (2011).

Bibliography

[1] KS Novoselov, AK Geim, and SV Morozov. Electric field effect in atomically thin carbon films. *science*, 306(October):666–669, 2004. URL http://www.sciencemag.org/content/306/5696/666.short.

[2] a. H. Castro Neto, N. M. R. Peres, K. S. Novoselov, and a. K. Geim. The electronic properties of graphene. *Reviews of Modern Physics*, 81(1):109–162, jan 2009. ISSN 0034-6861. doi: 10.1103/RevModPhys.81.109. URL http://link.aps.org/doi/10.1103/RevModPhys.81.109.

[3] A. I. Rusanov. Thermodynamics of graphene. *Surface Science Reports*, 69(4): 296–324, 2014. ISSN 01675729. doi: 10.1016/j.surfrep.2014.08.003. URL http://dx.doi.org/10.1016/j.surfrep.2014.08.003.

[4] DF Litim. Graphene: Mind the gap. *International Journal of Modern Physics A*, 6(October), 2001. URL http://www.worldscientific.com/doi/abs/10.1142/S0217751X01004748.

[5] Filip A. Rasmussen and Kristian S. Thygesen. Computational 2D Materials Database: Electronic Structure of Transition-Metal Dichalcogenides and Oxides. *Journal of Physical Chemistry C*, 119(23):13169–13183, 2015. ISSN 19327455. doi: 10.1021/acs.jpcc.5b02950.

[6] A. K. Geim and I. V. Grigorieva. Van der Waals heterostructures. *Nature*, 499 (7459):419–425, 2013. ISSN 00280836. doi: 10.1038/nature12385. URL http://dx.doi.org/10.1038/nature12385.

[7] K. S. Novoselov, A. Mishchenko, A. Carvalho, and A. H. Castro Neto. 2D materials and van der Waals heterostructures. *Science*, 353(6298), 2016. ISSN 10959203. doi: 10.1126/science.aac9439.

[8] G.E. Moore. Cramming More Components Onto Integrated Circuits. *Proceedings of the IEEE*, 86(1):82–85, jan 1998. ISSN 0018-9219. doi: 10.1109/JPROC.1998.658762. URL http://ieeexplore.ieee.org/lpdocs/epic03/wrapper.htm?arnumber=658762.

[9] M. I. Katsnelson, K. S. Novoselov, and a. K. Geim. Chiral tunneling and the Klein paradox in graphene. 2(September):15, 2006. ISSN 1745-2473. doi: 10.1038/nphys384. URL http://arxiv.org/abs/cond-mat/0604323.

[10] Ruitao Lv, Qing Li, Andrés R Botello-Méndez, Takuya Hayashi, Bei Wang, Ayse Berkdemir, Qingzhen Hao, Ana Laura Elías, Rodolfo Cruz-Silva, Humberto R Gutiérrez, Yoong Ahm Kim, Hiroyuki Muramatsu, Jun Zhu, Morinobu Endo, Humberto Terrones, Jean-Christophe Charlier, Minghu Pan, and Mauricio Terrones. Nitrogen-doped graphene: beyond single substitution and enhanced molecular sensing. *Scientific reports*, 2:586, jan 2012. ISSN 2045-2322. doi: 10.

1038/srep00586. URL http://www.pubmedcentral.nih.gov/articlerender.fcgi?artid=3421434{&}tool=pmcentrez{&}rendertype=abstract.

[11] Blanca Biel, X. Blase, François Triozon, and Stephan Roche. Anomalous doping effects on charge transport in graphene nanoribbons. *Physical Review Letters*, 102(March):1–4, 2009. ISSN 00319007. doi: 10.1103/PhysRevLett.102.096803.

[12] Chaohua Zhang, Lei Fu, Nan Liu, Minhao Liu, Yayu Wang, and Zhongfan Liu. Synthesis of nitrogen-doped graphene using embedded carbon and nitrogen sources. *Advanced materials (Deerfield Beach, Fla.)*, 23(8):1020–4, feb 2011. ISSN 1521-4095. doi: 10.1002/adma.201004110. URL http://www.ncbi.nlm.nih.gov/pubmed/21341318.

[13] Jonathan R. Owens, Eduardo Cruz-Silva, and Vincent Meunier. Electronic structure and transport properties of N2AA-doped armchair and zigzag graphene nanoribbons. *Nanotechnology*, 24(23), 2013. ISSN 09574484. doi: 10.1088/0957-4484/24/23/235701.

[14] Amir Zabet-Khosousi, Liuyan Zhao, Lucia Pálová, Mark S Hybertsen, David R Reichman, Abhay N Pasupathy, and George W Flynn. Segregation of sublattice domains in nitrogen-doped graphene. *Journal of the American Chemical Society*, 136(4):1391–7, jan 2014. ISSN 1520-5126. doi: 10.1021/ja408463g. URL http://www.ncbi.nlm.nih.gov/pubmed/24392951.

[15] Thomas Garm Pedersen and Jesper Goor Pedersen. Self-consistent tight-binding model of B and N doping in graphene. *Physical Review B*, 87(15):155433, 2013. ISSN 1098-0121. doi: 10.1103/PhysRevB.87.155433. URL https://link.aps.org/doi/10.1103/PhysRevB.87.155433.

[16] James a. Lawlor and Mauro S. Ferreira. Sublattice asymmetry of impurity doping in graphene: A review. page 20, jul 2014. doi: 10.3762/bjnano.5.133. URL http://arxiv.org/abs/1407.2560.

[17] Aurélien Lherbier, X. Blase, Yann-Michel Niquet, François Triozon, and Stephan Roche. Charge Transport in Chemically Doped 2D Graphene. *Physical Review Letters*, 101(3):036808, jul 2008. ISSN 0031-9007. doi: 10.1103/PhysRevLett.101.036808. URL http://link.aps.org/doi/10.1103/PhysRevLett.101.036808.

[18] Aurélien Lherbier, Andrés Rafael Botello-Méndez, and Jean Christophe Charlier. Electronic and transport properties of unbalanced sublattice N-doping in graphene. *Nano Letters*, 13:1446–1450, 2013. ISSN 15306984. doi: 10.1021/nl304351z.

[19] Mark B. Lundeberg and Joshua A. Folk. Harnessing chirality for valleytronics. *Science*, 346(6208):422–423, oct 2014. ISSN 0036-8075. doi: 10.1126/science.1260989. URL http://www.sciencemag.org/lookup/doi/10.1126/science.1260989.

[20] A. Rycerz, J. Tworzydło, and C. W.J. Beenakker. Valley filter and valley valve in graphene. *Nature Physics*, 3(3):172–175, 2007. ISSN 17452473. doi: 10.1038/nphys547.

[21] J. L. Garcia-Pomar, A. Cortijo, and M. Nieto-Vesperinas. Fully Valley-Polarized Electron Beams in Graphene. *Physical Review Letters*, 100(23):1–4, 2008. ISSN 00319007. doi: 10.1103/PhysRevLett.100.236801.

[22] T. Fujita, M. B A Jalil, and S. G. Tan. Valley filter in strain engineered graphene. *Applied Physics Letters*, 97(4):97–100, 2010. ISSN 00036951. doi: 10.1063/1.3473725.

[23] D. Gunlycke and C. T. White. Graphene Valley Filter Using a Line Defect. *Physical Review Letters*, 106(13):1–4, 2011. ISSN 00319007. doi: 10.1103/PhysRevLett.106.136806.

[24] J. H. Chen, G. Autès, N. Alem, F. Gargiulo, A. Gautam, M. Linck, C. Kisielowski, O. V. Yazyev, S. G. Louie, and A. Zettl. Controlled growth of a line defect in graphene and implications for gate-tunable valley filtering. *Physical Review B - Condensed Matter and Materials Physics*, 89(12):1–5, 2014. ISSN 1550235X. doi: 10.1103/PhysRevB.89.121407.

[25] Henning Schomerus. Helical scattering and valleytronics in bilayer graphene. *Physical Review B - Condensed Matter and Materials Physics*, 82(16):1–6, 2010. ISSN 10980121. doi: 10.1103/PhysRevB.82.165409.

[26] Long Ju, Zhiwen Shi, Nityan Nair, Yinchuan Lv, Chenhao Jin, Jairo Velasco, Claudia Ojeda-Aristizabal, Hans A. Bechtel, Michael C. Martin, Alex Zettl, James Analytis, and Feng Wang. Topological valley transport at bilayer graphene domain walls. *Nature*, 520(7549):650–655, 2015. ISSN 14764687. doi: 10.1038/nature14364.

[27] Fan Zhang, A. H. MacDonald, and E. J. Mele. Valley Chern Numbers and Boundary Modes in Gapped Bilayer Graphene. 2013. ISSN 0027-8424. doi: 10.1073/pnas.1308853110. URL http://arxiv.org/abs/1301.4205{%}0Ahttp://dx.doi.org/10.1073/pnas.1308853110.

[28] Wang Yao, Shengyuan A. Yang, and Qian Niu. Edge states in graphene: From gapped flat-band to gapless chiral modes. *Physical Review Letters*, 102(9):1–4, 2009. ISSN 00319007. doi: 10.1103/PhysRevLett.102.096801.

[29] G. W. Semenoff, V. Semenoff, and Fei Zhou. Domain walls in gapped graphene. 087204(August):1–4, 2008. ISSN 0031-9007. doi: 10.1103/PhysRevLett.101.087204. URL http://arxiv.org/abs/0806.0094{%}0Ahttp://dx.doi.org/10.1103/PhysRevLett.101.087204.

[30] Di Xiao, Wang Yao, and Qian Niu. Valley-contrasting physics in graphene: Magnetic moment and topological transport. *Physical Review Letters*, 99(23):1–4, 2007. ISSN 00319007. doi: 10.1103/PhysRevLett.99.236809.

[31] Tsuneya Ando. Theory of Valley Hall Conductivity in Graphene with Gap. *Journal of the Physical Society of Japan*, 84(11):1–14, 2015. ISSN 13474073. doi: 10.7566/JPSJ.84.114705.

[32] A. Cresti, B. K. Nikolíc, J. H. Garćia, and S. Roche. Charge, spin and valley Hall effects in disordered grapheme. *Rivista del Nuovo Cimento*, 39(12):587–667, 2016. ISSN 0393697X. doi: 10.1393/ncr/i2016-10130-6.

[33] R. V. Gorbachev, J. C W Song, G. L. Yu, A. V. Kretinin, F. Withers, Y. Cao, A. Mishchenko, I. V. Grigorieva, K. S. Novoselov, L. S. Levitov, and A. K. Geim. Detecting Topological Currents in Graphene Superlattices. *Science*, 346 (6208):448–451, aug 2014. ISSN 10959203. URL http://arxiv.org/abs/1409.0113http://dx.doi.org/10.1126/science.1254966.

[34] Mikkel Settnes, Stephen R. Power, Mads Brandbyge, and Antti Pekka Jauho. Graphene Nanobubbles as Valley Filters and Beam Splitters. *Physical Review Letters*, 117(27):1–5, 2016. ISSN 10797114. doi: 10.1103/PhysRevLett.117.276801.

[35] N. Levy, S. A. Burke, K. L. Meaker, M. Panlasigui, A. Zettl, F. Guinea, A. H. C. Neto, and M. F. Crommie. Strain-Induced Pseudo-Magnetic Fields Greater Than 300 Tesla in Graphene Nanobubbles. *Science*, 329(5991):544–547, jul 2010. ISSN 0036-8075. doi: 10.1126/science.1191700. URL http://www.sciencemag.org/cgi/doi/10.1126/science.1191700.

[36] M. M. Fogler, F. Guinea, and M. I. Katsnelson. Pseudomagnetic fields and ballistic transport in a suspended graphene sheet. *Physical Review Letters*, 101(22): 1–4, 2008. ISSN 00319007. doi: 10.1103/PhysRevLett.101.226804.

[37] F. Guinea, A. K. Geim, M. I. Katsnelson, and K. S. Novoselov. Generating quantizing pseudomagnetic fields by bending graphene ribbons. *Physical Review B - Condensed Matter and Materials Physics*, 81(3):1–5, 2010. ISSN 10980121. doi: 10.1103/PhysRevB.81.035408.

[38] A. Ramires and J. L. Lado. Electrically tunable gauge fields in tiny-angle twisted bilayer graphene. pages 1–9, mar 2018. URL http://arxiv.org/abs/1803.04400.

[39] S Reich, J Maultzsch, C Thomsen, and P Ordejón. Tight-binding description of graphene. *Phys. Rev. B*, 66(3):35412, 2002. ISSN 0163-1829. doi: 10.1103/PhysRevB.66.035412. URL http://link.aps.org/doi/10.1103/PhysRevB.66.035412.

[40] Giuseppe Grosso and Giuseppe Pastori Parravicini. *Solid State Physics*. 2014. ISBN 9780123850300. doi: 10.1016/B978-0-12-385030-0.00005-0. URL http://www.sciencedirect.com/science/article/pii/B9780123850300000050.

[41] Henrik Bruus and Karsten Flensberg. *Many-Body Quantum Theory in Condensed Matter Physics An Introduction*. Oxford University Press, 2012 repri edition, 2004. ISBN 978-0-19-856633-5.

[42] Magnus Paulsson and Mads Brandbyge. Transmission eigenchannels from nonequilibrium Green's functions. *Physical Review B - Condensed Matter and Materials Physics*, 76(11):1–7, 2007. ISSN 10980121. doi: 10.1103/PhysRevB.76.115117.

[43] BA Lippmann and J Schwinger. Variational principles for scattering processes. I. *Physical Review*, 337(1948), 1950. URL http://journals.aps.org/pr/abstract/10.1103/PhysRev.79.469.

[44] Mikkel Settnes, Stephen R. Power, Jun Lin, Dirch H. Petersen, and Antti-Pekka Jauho. Patched Green's function techniques for two-dimensional systems: Electronic behavior of bubbles and perforations in graphene. *Physical Review B*, 91(12):1–12, 2015. ISSN 1098-0121. doi: 10.1103/PhysRevB.91.125408. URL http://link.aps.org/doi/10.1103/PhysRevB.91.125408.

[45] G. Thorgilsson, G. Viktorsson, and S. I. Erlingsson. Recursive Green's function method for multi-terminal nanostructures. *Journal of Computational Physics*, 261: 256–266, 2014. ISSN 00219991. doi: 10.1016/j.jcp.2013.12.054. URL http://dx.doi.org/10.1016/j.jcp.2013.12.054.

[46] Caio H. Lewenkopf and Eduardo R. Mucciolo. The recursive Green's function method for graphene. *Journal of Computational Electronics*, 12(2):203–231, may 2013. ISSN 1569-8025. doi: 10.1007/s10825-013-0458-7. URL http://link.springer.com/10.1007/s10825-013-0458-7.

[47] M P Lopez Sancho, J M Lopez Sancho, and J Rubio. Quick iterative scheme for the calculation of transfer matrices: application to Mo (100). *Journal of Physics F: Metal Physics*, 14(5):1205–1215, may 1984. ISSN 0305-4608. doi: 10.1088/0305-4608/14/5/016. URL http://stacks.iop.org/0305-4608/14/i=5/a=016?key=crossref.73654bb2c5e7ede93601a4f4e5f6247b.

[48] Paul Soven. Coherent-potential model of substitutional disordered alloys. *Physical Review*, 1017, 1967. URL http://journals.aps.org/pr/abstract/10.1103/PhysRev.156.809.

[49] J Elliott. The theory and properties of random IIly disordered crystals and related physical systeIIIs. 46(3), 1974.

[50] James A. Lawlor and Mauro S. Ferreira. Green functions of graphene: An analytic approach. *Physica B: Condensed Matter*, 463:48–53, 2015. ISSN 09214526. doi: 10.1016/j.physb.2015.01.032.

[51] Alessandro Cresti, Norbert Nemec, Blanca Biel, Gabriel Niebler, Francois Triozon, Gianaurelio Cuniberti, and Stephan Roche. Charge Transport in Disordered Graphene-Based Low Dimensional Materials. page 32, 2008. ISSN 1998-0124. doi: 10.1007/s12274-008-8043-2. URL http://arxiv.org/abs/0809.4630.

[52] Gordon W. Semenoff. Condensed-Matter simulation of a three-Dimensional anomaly. *Physical Review Letters*, 53(26):2449–2452, 1984. ISSN 00319007. doi: 10.1103/PhysRevLett.53.2449.

[53] R. Jackiw and C. Rebbi. Solitons with fermion number. *Physical Review D*, 13 (12):3398–3409, 1976. ISSN 05562821. doi: 10.1103/PhysRevD.13.3398.

[54] O. Nganba Meetei and Archana Anandakrishnan. Generalized Jackiw-Rebbi Model and Topological Classification of Free Fermion Insulators. 2014. URL http://arxiv.org/abs/1406.0500.

[55] Liuyan Zhao, Rui He, Kwang Taeg Rim, Theanne Schiros, Keun Soo Kim, Hui Zhou, Christopher Gutiérrez, S P Chockalingam, Carlos J Arguello, Lucia Pálová, Dennis Nordlund, Mark S Hybertsen, David R Reichman, Tony F Heinz, Philip Kim, Aron Pinczuk, George W Flynn, and Abhay N Pasupathy. Visualizing individual nitrogen dopants in monolayer graphene. *Science (New York, N.Y.)*, 333(6045):999–1003, aug 2011. ISSN 1095-9203. doi: 10.1126/science.1208759. URL http://www.ncbi.nlm.nih.gov/pubmed/21852495.

[56] Liuyan Zhao, Mark Levendorf, Scott Goncher, Theanne Schiros, Lucia Pálová, Amir Zabet-Khosousi, Kwang Taeg Rim, Christopher Gutiérrez, Dennis Nordlund, Cherno Jaye, Mark Hybertsen, David Reichman, George W Flynn, Jiwoong Park, and Abhay N Pasupathy. Local atomic and electronic structure of boron chemical doping in monolayer graphene. *Nano letters*, 13(10):4659–65, oct 2013. ISSN 1530-6992. doi: 10.1021/nl401781d. URL http://www.ncbi.nlm.nih.gov/pubmed/24032458.

[57] I. Deretzis and A. La Magna. Origin and impact of sublattice symmetry breaking in nitrogen-doped graphene. *Physical Review B - Condensed Matter and Materials Physics*, 89(11):1–5, 2014. ISSN 1550235X. doi: 10.1103/PhysRevB.89.115408.

[58] J. a. Lawlor, S. R. Power, and M. S. Ferreira. Friedel oscillations in graphene: Sublattice asymmetry in doping. *Physical Review B*, 88(20):205416, nov 2013. ISSN 1098-0121. doi: 10.1103/PhysRevB.88.205416. URL http://link.aps.org/doi/10.1103/PhysRevB.88.205416.

[59] James A. Lawlor, Paul D. Gorman, Stephen R. Power, Claudionor G. Bezerra, and Mauro S. Ferreira. Sublattice imbalance of substitutionally doped nitrogen in graphene. *Carbon*, 77:645–650, 2014. ISSN 00086223. doi: 10.1016/j.carbon.2014.05.069. URL http://dx.doi.org/10.1016/j.carbon.2014.05.069.

[60] Vitor Pereira, J. Lopes dos Santos, and a. Castro Neto. Modeling disorder in graphene. *Physical Review B*, 77(11):115109, mar 2008. ISSN 1098-0121. doi: 10.1103/PhysRevB.77.115109. URL http://link.aps.org/doi/10.1103/PhysRevB.77.115109.

[61] D. A. Abanin, A. V. Shytov, and L. S. Levitov. Peierls-Type Instability and Tunable Band Gap in Functionalized Graphene. *Physical Review Letters*, 105(8):086802, aug 2010. ISSN 0031-9007. doi: 10.1103/PhysRevLett.105.086802. URL https://link.aps.org/doi/10.1103/PhysRevLett.105.086802.

[62] Dmitry Abanin and Leonid Levitov. Spatial Ordering of Defects and Conductivity of Functionalized Graphene. *Physical Review Letters*, 105(8):1–6, aug 2010. ISSN 00319007. URL http://arxiv.org/abs/1004.3678http://dx.doi.org/10.1103/PhysRevLett.105.086802http://arxiv.org/abs/1008.1424.

[63] P. M. Ostrovsky, M. Titov, S. Bera, I. V. Gornyi, and A. D. Mirlin. Diffusion and criticality in undoped graphene with resonant scatterers. *Physical Review Letters*, 105(26):1–4, 2010. ISSN 00319007. doi: 10.1103/PhysRevLett.105.266803.

[64] Gianluca Giovannetti, Petr A. Khomyakov, Geert Brocks, Paul J. Kelly, and Jeroen Van Den Brink. Substrate-induced band gap in graphene on hexagonal boron nitride: Ab initio density functional calculations. *Physical Review B - Condensed Matter and Materials Physics*, 76(7):2–5, 2007. ISSN 10980121. doi: 10.1103/PhysRevB.76.073103.

[65] T. C. Li and Shao Ping Lu. Quantum conductance of graphene nanoribbons with edge defects. *Physical Review B - Condensed Matter and Materials Physics*, 77:1–8, 2008. ISSN 10980121. doi: 10.1103/PhysRevB.77.085408.

[66] E. R. Mucciolo, A. H. Castro Neto, and C. H. Lewenkopf. Conductance quantization and transport gaps in disordered graphene nanoribbons. *Physical Review B - Condensed Matter and Materials Physics*, 79(7):1–5, 2009. ISSN 10980121. doi: 10.1103/PhysRevB.79.075407.

[67] V. a. Rigo, T. B. Martins, Antonio J R Da Silva, a. Fazzio, and R. H. Miwa. Electronic, structural, and transport properties of Ni-doped graphene nanoribbons. *Physical Review B - Condensed Matter and Materials Physics*, 79:1–9, 2009. ISSN 10980121. doi: 10.1103/PhysRevB.79.075435.

[68] P. Dietl, G. Metalidis, D. Golubev, P. San-Jose, E. Prada, H. Schomerus, and G. Schön. Disorder-induced pseudodiffusive transport in graphene nanoribbons. *Physical Review B - Condensed Matter and Materials Physics*, 79(19):1–5, 2009. ISSN 10980121. doi: 10.1103/PhysRevB.79.195413.

[69] Jens Kunstmann, Cem Özdoğan, Alexander Quandt, and Holger Fehske. Stability of edge states and edge magnetism in graphene nanoribbons. *Physical Review B*, 83(4):045414, jan 2011. ISSN 1098-0121. doi: 10.1103/PhysRevB.83.045414. URL http://arxiv.org/abs/1007.2602http://dx.doi.org/10.1103/PhysRevB.83.045414https://link.aps.org/doi/10.1103/PhysRevB.83.045414.

[70] E. Cruz-Silva, Z. Barnett, B. Sumpter, and V. Meunier. Structural, magnetic, and transport properties of substitutionally doped graphene nanoribbons from first principles. *Physical Review B*, 83:1–9, 2011. ISSN 1098-0121. doi: 10.1103/PhysRevB.83.155445.

[71] Karri Saloriutta, Y. Hancock, Asta Kärkkäinen, Leo Kärkkäinen, Martti J. Puska, and Antti Pekka Jauho. Electron transport in edge-disordered graphene nanoribbons. *Physical Review B - Condensed Matter and Materials Physics*, 83(20):2–7, 2011. ISSN 10980121. doi: 10.1103/PhysRevB.83.205125.

[72] Po Hao Chang and Branislav K. Nikolić. Edge currents and nanopore arrays in zigzag and chiral graphene nanoribbons as a route toward high-ZT thermoelectrics. *Physical Review B - Condensed Matter and Materials Physics*, 86(4):1–5, 2012. ISSN 10980121. doi: 10.1103/PhysRevB.86.041406.

[73] A. R. Botello-Méndez, A. Lherbier, and J. C. Charlier. Modeling electronic properties and quantum transport in doped and defective graphene. *Solid State Communications*, 175-176:90–100, 2013. ISSN 00381098. doi: 10.1016/j.ssc.2013.08.029. URL http://dx.doi.org/10.1016/j.ssc.2013.08.029.

[74] A. Orlof, J. Ruseckas, and I. V. Zozoulenko. Effect of zigzag and armchair edges on the electronic transport in single-layer and bilayer graphene nanoribbons with defects. *Physical Review B - Condensed Matter and Materials Physics*, 88(12):1–12, 2013. ISSN 10980121. doi: 10.1103/PhysRevB.88.125409.

[75] Jan Wilhelm, Michael Walz, and Ferdinand Evers. Ab initio quantum transport through armchair graphene nanoribbons: Streamlines in the current density. *Physical Review B - Condensed Matter and Materials Physics*, 89(19):1–7, 2014. ISSN 1550235X. doi: 10.1103/PhysRevB.89.195406.

[76] Jan Wilhelm, Michael Walz, and Ferdinand Evers. Ab initio spin-flip conductance of hydrogenated graphene nanoribbons: Spin-orbit interaction and scattering with local impurity spins. *Physical Review B - Condensed Matter and Materials Physics*, 92(1):1–9, 2015. ISSN 1550235X. doi: 10.1103/PhysRevB.92.014405.

[77] Thomas Garm Pedersen. Self-consistent model of edge doping in graphene. *Physical Review B - Condensed Matter and Materials Physics*, 91(8):1–6, 2015. ISSN 1550235X. doi: 10.1103/PhysRevB.91.085428.

[78] Jayeeta Lahiri, You Lin, Pinar Bozkurt, Ivan I. Oleynik, and Matthias Batzill. An extended defect in graphene as a metallic wire. *Nature Nanotechnology*, 5 (5):326–329, 2010. ISSN 17483395. doi: 10.1038/nnano.2010.53. URL http://dx.doi.org/10.1038/nnano.2010.53.

[79] M. F. Craciun, S. Russo, M. Yamamoto, and S. Tarucha. Tuneable electronic properties in graphene. *Nano Today*, 6(1):42–60, 2011. ISSN 17480132. doi: 10.1016/j.nantod.2010.12.001.

[80] R. L. Heinisch, F. X. Bronold, and H. Fehske. Mie scattering analog in graphene: Lensing, particle confinement, and depletion of Klein tunneling. *Physical Review B - Condensed Matter and Materials Physics*, 87(15):1–5, 2013. ISSN 10980121. doi: 10.1103/PhysRevB.87.155409.

[81] Mikkel Settnes, Stephen R. Power, Dirch H. Petersen, and Antti-Pekka Jauho. Theoretical Analysis of a Dual-Probe Scanning Tunneling Microscope Setup on Graphene. *Physical Review Letters*, 112(9):096801, 2014. ISSN 0031-9007. doi: 10.1103/PhysRevLett.112.096801. URL http://link.aps.org/doi/10.1103/PhysRevLett.112.096801.

[82] Gui Bin Liu, Wen Yu Shan, Yugui Yao, Wang Yao, and Di Xiao. Three-band tight-binding model for monolayers of group-VIB transition metal dichalcogenides. *Physical Review B - Condensed Matter and Materials Physics*, 88(8):1–10, 2013. ISSN 10980121. doi: 10.1103/PhysRevB.88.085433.

[83] A. N. Rudenko and M. I. Katsnelson. Quasiparticle band structure and tight-binding model for single- and bilayer black phosphorus. *Physical Review B - Condensed Matter and Materials Physics*, 89(20):1–5, 2014. ISSN 1550235X. doi: 10.1103/PhysRevB.89.201408.

[84] Ferdows Zahid, Lei Liu, Yu Zhu, Jian Wang, and Hong Guo. A generic tight-binding model for monolayer, bilayer and bulk MoS2. *AIP Advances*, 3(5), 2013. ISSN 21583226. doi: 10.1063/1.4804936.

[85] A. B. Kuzmenko, I. Crassee, D. Van Der Marel, P. Blake, and K. S. Novoselov. Determination of the gate-tunable band gap and tight-binding parameters in bilayer graphene using infrared spectroscopy. *Physical Review B - Condensed Matter and Materials Physics*, 80(16):1–12, 2009. ISSN 10980121. doi: 10.1103/PhysRevB.80.165406.

[86] Thomas G. Pedersen, Christian Flindt, Jesper Pedersen, Niels Asger Mortensen, Antti Pekka Jauho, and Kjeld Pedersen. Graphene antidot lattices: Designed defects and spin qubits. *Physical Review Letters*, 100(13):1–4, 2008. ISSN 00319007. doi: 10.1103/PhysRevLett.100.136804.

[87] Thomas G. Pedersen, Christian Flindt, Jesper Pedersen, Antti Pekka Jauho, Niels Asger Mortensen, and Kjeld Pedersen. Optical properties of graphene antidot lattices. *Physical Review B - Condensed Matter and Materials Physics*, 77 (24):1–6, 2008. ISSN 10980121. doi: 10.1103/PhysRevB.77.245431.

[88] René Petersen and Thomas Garm Pedersen. Quasiparticle properties of graphene antidot lattices. *Physical Review B - Condensed Matter and Materials Physics*, 80(11), 2009. ISSN 10980121. doi: 10.1103/PhysRevB.80.113404.

[89] Tue Gunst, Troels Markussen, Antti Pekka Jauho, and Mads Brandbyge. Thermoelectric properties of finite graphene antidot lattices. *Physical Review B - Condensed Matter and Materials Physics*, 84(15):1–11, 2011. ISSN 10980121. doi: 10.1103/PhysRevB.84.155449.

[90] René Petersen, Thomas Garm Pedersen, and Antti Pekka Jauho. Clar sextet analysis of triangular, rectangular, and honeycomb graphene antidot lattices. *ACS Nano*, 5(1):523–529, 2011. ISSN 19360851. doi: 10.1021/nn102442h.

[91] Stephen R. Power and Antti Pekka Jauho. Electronic transport in disordered graphene antidot lattice devices. *Physical Review B - Condensed Matter and Materials Physics*, 90(11):1–15, 2014. ISSN 1550235X. doi: 10.1103/PhysRevB.90.115408.

[92] Søren Schou Gregersen, Jesper Goor Pedersen, Stephen R. Power, and Antti Pekka Jauho. Graphene on graphene antidot lattices: Electronic and transport properties. *Physical Review B - Condensed Matter and Materials Physics*, 91 (11):1–12, 2015. ISSN 1550235X. doi: 10.1103/PhysRevB.91.115424.

Published by:
DTU Nanotech
Department of Micro- and Nanotechnology
Technical University of Denmark
Ørsteds Plads, building 345C
DK-2800 Kgs. Lyngby